

# Investigation of Mixing Models and Finite Volume Conditional Moment Closure Applied to Autoignition of Hydrogen Jets

by

Andrew Buckrell

A thesis  
presented to the University of Waterloo  
in fulfilment of the  
thesis requirement for the degree of  
Master of Applied Science  
in  
Mechanical Engineering

Waterloo, Ontario, Canada, 2012

© Andrew Buckrell 2012

I hereby declare that I am the sole author of this thesis. This is a true copy of the thesis, including any required final revisions, as accepted by my examiners.

I understand that my thesis may be made electronically available to the public.

## Abstract

In the present work, the processes of steady combustion and autoignition of hydrogen are investigated using the Conditional Moment Closure (CMC) model with a Reynolds Averaged Navier-Stokes (RANS) Computational Fluid Dynamics (CFD) code. A study of the effects on the flowfield of changing turbulence model constants, specifically the turbulent Schmidt number,  $Sc_t$ , and  $C_{\epsilon_1}$  of the  $k - \epsilon$  model, are investigated. The effects of two different mixing models are explored: the AMC model, which is commonly used in CMC implementations, and a model based on the assumption of inhomogeneous turbulence.

The background equations required for implementation of the CMC model are presented, and all relevant closures are discussed. The numerical implementation of the CMC model, in addition to other techniques aimed at reducing computational expense of the CMC calculations, are provided. The CMC equation is discretised using finite volume (FV) method. The CFD and CMC calculations are fully coupled, allowing for simulations of steady flames or flame development after the occurrence of autoignition.

Through testing of a steady jet flame, it is observed that the flowfield calculations follow typical  $k - \epsilon$  model trends, with an overprediction of spreading and an underprediction of penetration. The CMC calculations are observed to perform well, providing good agreement with experimental measurements.

Autoignition simulations are conducted for 3 different cases of turbulence constants and 7 different coflow temperatures to determine the final effect on the steady flowfield. In comparison to the standard constants, reduction of  $Sc_t$  results in a reduction of the centreline mixing intensity within the flowfield and a corresponding reduction of ignition length, while reducing  $C_{\epsilon_1}$  results in an increase of centreline mixing intensity and an increase in the ignition length. All scenarios tested result in an underprediction of ignition length in comparison to experimental results; however, good agreement with the experimental trends is achieved. At low coflow temperatures, the effects of mixing intensity within the flowfield are seen to have the largest influence on ignition length, while at high coflow temperatures, the chemical source term in the CMC equation increases in magnitude, resulting in very little difference between predictions for different sets of turbulence constants.

The inhomogeneous mixing model is compared using the standard turbulence constants. A reduction of ignition lengths in comparison to the AMC model is observed. In steady state simulation of the autoigniting flow, the inhomogeneous model is observed to predict both lifted flames and fully anchored flames, depending on coflow temperature.

## **Acknowledgements**

I would like to thank my supervisor, Professor Cécile Devaud, for continued help, guidance and patience throughout the duration of my MASc studies. My knowledge and understanding of CFD, CMC and combustion processes have greatly increased thanks to her help, as has my enjoyment of numerical work and problem solving.

I would also like to thank Professor Carolyn Ren and Professor Zhongchao Tan for reviewing my thesis.

# Contents

List of Tables	x
List of Figures	xiii
Nomenclature	xiv
<b>1 Introduction</b>	<b>1</b>
1.1 Overview . . . . .	1
1.2 Objectives . . . . .	2
1.3 Outline . . . . .	3
<b>2 Background</b>	<b>5</b>
2.1 Governing Equations of Fluid Flow . . . . .	5
2.1.1 Mass . . . . .	6
2.1.2 Momentum . . . . .	6
2.1.3 Enthalpy . . . . .	7
2.1.4 Species Transport . . . . .	8
2.2 Averaging Techniques . . . . .	8
2.2.1 Reynolds Averaging . . . . .	9
2.2.2 Favre-Averaging . . . . .	10

2.3	Turbulence Modelling . . . . .	11
2.3.1	Reynolds Averaged Navier-Stokes Simulations . . . . .	12
2.3.2	Large Eddy Simulation . . . . .	16
2.3.3	Direct Numerical Simulation . . . . .	17
2.4	Stochastic Description of Flows . . . . .	17
2.5	Turbulent Reacting Flows and Non-premixed Combustion . . . . .	19
2.5.1	Damköhler Number . . . . .	20
2.5.2	Mixture Fraction . . . . .	20
2.5.3	Mean Scalar Dissipation Rate . . . . .	22
2.6	Turbulent Combustion Models . . . . .	23
2.6.1	Eddy Break-up Model . . . . .	23
2.6.2	Laminar Flamelet Model . . . . .	24
2.6.3	Lagrangian PDF Transport Model . . . . .	25
2.7	Summary . . . . .	26
<b>3</b>	<b>Conditional Moment Closure</b>	<b>27</b>
3.1	Overview . . . . .	27
3.2	Conditional Species Transport Equation . . . . .	28
3.3	Conditional Enthalpy and Temperature Equation . . . . .	30
3.4	Terms Requiring Closure . . . . .	32
3.4.1	Conditional Chemical Source Term . . . . .	32
3.4.2	Turbulent Flux . . . . .	34
3.4.3	Conditional Velocity . . . . .	35
3.4.4	Probability Density Function . . . . .	35
3.5	Conditional Scalar Dissipation Rate . . . . .	38
3.5.1	Mixing Models based on Homogeneous Turbulence . . . . .	38
3.5.2	Models Based on Inhomogeneous Turbulence . . . . .	40
3.6	Summary . . . . .	42

<b>4</b>	<b>Previous Experimental and Numerical Studies</b>	<b>43</b>
4.1	Steady Flame . . . . .	43
4.1.1	Experimental Method . . . . .	44
4.1.2	Experimental Results . . . . .	44
4.1.3	Review of Previous Numerical Simulation . . . . .	46
4.2	Autoigniting Flame . . . . .	46
4.2.1	Experimental Method . . . . .	47
4.2.2	Experimental Method . . . . .	47
4.2.3	Experimental Results . . . . .	48
4.2.4	Review of Previous Numerical Simulation . . . . .	50
4.3	Summary . . . . .	58
<b>5</b>	<b>Numerical Implementation of Conditional Moment Closure</b>	<b>59</b>
5.1	Code Structure . . . . .	59
5.1.1	Coupling of CFD and CMC . . . . .	62
5.1.2	Finite Volume Method . . . . .	63
5.2	Solution of Ordinary Differential Equations . . . . .	67
5.2.1	VODE Solver . . . . .	67
5.2.2	Implementation of VODE Solver . . . . .	68
5.3	Chemical Mechanism . . . . .	69
5.4	Optimisation of CMC calculations . . . . .	72
5.4.1	Dynamic CMC Grid . . . . .	72
5.4.2	CMC Grid Multiplier . . . . .	76
5.5	Summary . . . . .	77

<b>6</b>	<b>Steady State Validation</b>	<b>78</b>
6.1	Boundary Conditions . . . . .	78
6.2	CMC Grid Density Sensitivity Analysis . . . . .	82
6.3	Numerical and Experimental Comparison . . . . .	83
6.3.1	Favre-Averaged Flowfield Results . . . . .	83
6.3.2	Conditional Results . . . . .	95
6.3.3	Discussion of Results . . . . .	102
6.4	Summary . . . . .	103
<b>7</b>	<b>Autoigniting Flame</b>	<b>105</b>
7.1	Current Numerical Setup . . . . .	105
7.2	Computational Domain and Boundary Conditions . . . . .	106
7.3	Timestep and Grid Refinement . . . . .	107
7.4	Simulation Conditions . . . . .	109
7.5	Numerical Difficulties . . . . .	111
7.6	AMC Model Results . . . . .	112
7.6.1	Effects of Turbulence and Mixing Constants on Steady Flowfield . .	112
7.6.2	Mean Mixture Fraction . . . . .	112
7.6.3	Mean Mixture Fraction Variance . . . . .	113
7.6.4	Predictions of Ignition Length . . . . .	116
7.7	Comparison of Mixing Models . . . . .	123
7.7.1	Predictions of Ignition Length . . . . .	123
7.7.2	Conditional Scalar Dissipation Rate Temporal Evolution . . . . .	124
7.7.3	Conditional Scalars . . . . .	130
7.7.4	Steady Flame Predictions . . . . .	133
7.8	Inhomogeneous Model Results . . . . .	143
7.8.1	Equation Budgets . . . . .	143
7.9	Summary . . . . .	152

<b>8</b>	<b>Conclusions</b>	<b>154</b>
8.1	Numerical Techniques . . . . .	155
8.2	Steady State Results . . . . .	155
8.3	Autoignition Results . . . . .	156
8.4	Impact of Mixing Models . . . . .	157
8.5	Recommendations and Future Work . . . . .	157
	<b>Bibliography</b>	<b>164</b>

# List of Tables

4.1	Autoignition delay with 0-D CMC equation and $T_{cflow} = 1030\text{K}$ . . . . .	53
5.1	$H_2-O_2$ reaction mechanism - forward reaction constants . . . . .	70
5.2	$H_2-O_2$ reaction mechanism - steps 1 - 13 . . . . .	73
5.3	$H_2-O_2$ reaction mechanism - steps 13 - 19 . . . . .	74
7.1	Mixing parameters used in autoignition simulations . . . . .	110
7.2	Autoignition results with AMC mixing model . . . . .	119
7.3	Autoignition results with inhomogeneous mixing model . . . . .	120
7.4	Sample locations for comparison . . . . .	133
7.5	$\tilde{\xi}$ and $\tilde{\xi}''^2$ of locations studied for inhomogeneous model equation budgets .	144

# List of Figures

3.1	AMC model $G(\eta)$ distribution . . . . .	40
4.1	Steady mixture fraction, temperature and NO measurements . . . . .	45
4.2	Experimental apparatus for autoignition . . . . .	47
4.3	Experimental autoignition results . . . . .	50
4.4	Effects on $\tau_{ign}$ of increasing $\frac{1}{2}\langle\chi \mid \eta = 0.5\rangle$ . . . . .	53
4.5	LES-PDF autoignition length predictions . . . . .	56
4.6	LES-CMC autoignition length predictions . . . . .	57
5.1	Flow chart of code structure . . . . .	61
5.2	Schematic of computational grid . . . . .	64
5.3	Dynamic CMC grid . . . . .	76
6.1	Final mesh utilised for steady state calculations . . . . .	80
6.2	Full $\eta$ grid used for steady validation . . . . .	81
6.3	Partial $\eta$ grid used for steady validation . . . . .	81
6.4	Centreline $\tilde{U}$ profile . . . . .	84
6.5	$\tilde{U}$ radial profiles at different axial locations . . . . .	85
6.6	Centreline mixture fraction profile . . . . .	86
6.7	Mixture fraction radial profiles at different axial locations . . . . .	87
6.8	Centreline $\tilde{T}$ profile . . . . .	89

6.9	$\tilde{T}$ Radial profiles at different axial locations . . . . .	91
6.10	Centreline $\widetilde{Z}''^2$ profile . . . . .	92
6.11	$\widetilde{Z}''^2$ Radial profiles at different axial locations . . . . .	93
6.12	$\langle \chi   \eta \rangle$ Profiles at different locations . . . . .	97
6.13	$\langle Y_{OH}   \eta \rangle$ Profiles at different locations . . . . .	99
6.14	$\langle T   \eta \rangle$ profiles at different axial locations . . . . .	101
7.1	Final mesh utilised for autoignition simulations . . . . .	108
7.2	Full $\eta$ grid used for autoignition . . . . .	110
7.3	Partial $\eta$ grid used for autoignition . . . . .	110
7.4	Centreline $\tilde{\xi}$ profile . . . . .	113
7.5	$\tilde{\xi}$ Radial profiles at different locations . . . . .	114
7.6	Centreline $\tilde{\xi}$ profile . . . . .	116
7.7	$\widetilde{\xi}''^2$ Radial profiles at different locations . . . . .	117
7.8	Ignition length comparison for different cases . . . . .	120
7.9	Ignition length comparison, exp. results shifted by -10K . . . . .	121
7.10	$\tilde{\xi}_{mr}$ comparison for different cases . . . . .	122
7.11	$\langle \chi   \eta = \tilde{\xi}_{mr} \rangle$ comparison for different cases . . . . .	122
7.12	$\langle \chi   \eta \rangle$ and PDF evolution, $T_{cflow} = 1080K$ . . . . .	126
7.13	$\langle \chi   \eta \rangle$ and PDF evolution, $T_{cflow} = 980K$ . . . . .	127
7.14	$\langle \chi   \eta \rangle$ and PDF evolution, $T_{cflow} = 950K$ . . . . .	129
7.15	Conditional values at $\tau/\tau_{ign} = 0.95$ and at the time of ignition . . . . .	132
7.16	Centreline steady $\tilde{\xi}$ profile . . . . .	134
7.17	Centreline steady $\tilde{T}$ profile . . . . .	134
7.18	$\tilde{T}$ distribution within the computational domain . . . . .	135
7.19	$\tilde{P}(\eta)$ , $\langle \chi   \eta \rangle$ , $\langle Y_{OH}   \eta \rangle$ and $\langle T   \eta \rangle$ at Position 1 . . . . .	136

7.20	$\tilde{P}(\eta)$ , $\langle \chi   \eta \rangle$ , $\langle Y_{OH}   \eta \rangle$ and $\langle T   \eta \rangle$ at Position 2 . . . . .	137
7.21	$\tilde{P}(\eta)$ , $\langle \chi   \eta \rangle$ , $\langle Y_{OH}   \eta \rangle$ and $\langle T   \eta \rangle$ at Position 3 . . . . .	139
7.22	$\tilde{P}(\eta)$ , $\langle \chi   \eta \rangle$ , $\langle Y_{OH}   \eta \rangle$ and $\langle T   \eta \rangle$ at Position 4 . . . . .	140
7.23	Steady flame $\tilde{T}$ predictions, $T_{coflow} = 1080K, 1020K$ and $1000K$ . . . . .	141
7.24	Steady flame $\tilde{T}$ predictions, $T_{coflow} = 960K, 950K$ and $940K$ . . . . .	142
7.25	$\langle \chi   \eta \rangle$ at $r/d = 0, 0.5$ and $1.0$ , $x = 0.5L_{ign}$ . . . . .	145
7.26	Inhomogeneous model terms and $\tilde{P}(\eta)$ at $x = 0.5L_{ign}$ . . . . .	147
7.27	$\langle \chi   \eta \rangle$ at $r/d = 0, 0.5$ and $1.0$ , $x = 1.0L_{ign}$ . . . . .	148
7.28	Inhomogeneous model terms and $\tilde{P}(\eta)$ at $x = 1.0L_{ign}$ . . . . .	149
7.29	$\langle \chi   \eta \rangle$ at $r/d = 0, 0.5$ and $1.0$ , $x = 1.25L_{ign}$ . . . . .	150
7.30	Inhomogeneous model terms and $\tilde{P}(\eta)$ at $x = 1.25L_{ign}$ . . . . .	151

# Nomenclature

## Roman Symbols

$\dot{q}_{rad}$	Heat transfer due to radiation
$A$	Frequency factor
$c_p$	Specific heat capacity at constant pressure
$D_t$	Turbulent diffusivity
$h$	Enthalpy
$k$	Turbulent kinetic energy
$k(T)$	Reaction rate constant
$L$	Turbulent length scale
$L_{ign}$	Ignition Length
$n$	Temperature exponent
$p$	Pressure
$P(\eta)$	Probability density function
$Q_\alpha$	Conditional species mass fraction of species $\alpha$
$Q_h$	Conditional enthalpy
$Q_T$	Conditional temperature
$D_t$	Turbulent diffusivity
$r$	Radial coordinate
$T$	Temperature
$T_a$	Activation temperature
$u$	Velocity
$x$	Axial coordinate
$Y_\alpha$	Mass fraction of species $\alpha$

## Greek Symbols

$\alpha$	Species within the mixture
$\beta$	Beta function, temperature exponent
$\chi$	Scalar dissipation rate
$\delta_{ij}$	Kronecker's delta
$\dot{\omega}$	Chemical source term
$\eta$	Mixture fraction sample space variable
$\Gamma$	Gamma function
$\lambda$	Thermal conductivity
$\mu$	Dynamic viscosity
$\nu$	Kinematic viscosity
$\phi$	Conserved scalar
$\rho$	Density
$\tau$	Time
$\tau_c$	Chemical time scale
$\tau_t$	Mixing time scale
$\varepsilon$	Turbulent eddy dissipation
$\xi$	Mixture fraction
$\xi'^2$	Mixture fraction variance

## Non-dimensional Numbers

$Da$	Damköhler number
$Re$	Reynolds Number
$Sc_t$	Turbulent Schmidt number

## Subscripts and Superscripts

$coflow$	Property of coflow oxidiser stream
$f$	Originating from fuel stream

<i>ign</i>	Ignition value
<i>mr</i>	Most reactive
<i>o</i>	Originating from oxidiser stream
<i>p</i>	Product(s) in chemical reaction
<i>r</i>	Reactant(s) in chemical reaction
<i>stoich</i>	Stoichiometric value

### Other Notation

$\langle \psi   \eta \rangle$	Conditional average of $\psi$
$\langle \psi \rangle$	Unconditional average of $\psi$
$\overline{\psi}$	Reynolds average of $\psi$
$\tilde{\psi}$	Favre (density-weighted) average of $\psi$
$\psi'$	Fluctuation about unconditional average
$\psi''$	Fluctuation about conditional average

### Acronyms

AMC	Amplitude Mapping Closure
CDF	Cumulative Distribution Function
CFD	Computational Fluids Dynamics
CMC	Conditional Moment Closure
DNS	Direct Numerical Simulation
EBU	Eddy Break Up
HCCI	Homogeneous Charge Compression Ignition
LES	Large Eddy Simulation
ODE	Ordinary Differential Equation
PDE	Partial Differential Equation
PDF	Probability Density Function
RANS	Reynolds Averaged Navier Stokes
TKE	Turbulent Kinetic Energy
VODE	Variable coefficient Ordinary Differential Equation solver

# Chapter 1

## Introduction

### 1.1 Overview

Increased awareness of the effects of greenhouse gas emissions and the demand for renewable fuels has led to an interest in developing cleaner and more efficient combustion methods. Due to the high energy demands of the automotive industry, a large amount of research has been focused in developing the internal combustion engine for transportation use. It is of great interest to the world's automotive manufacturers to develop new analysis techniques to provide faster and more accurate predictions of engine performance. Although research efforts have increased in recent years, the gains in efficiency in gasoline and diesel based engines are slowing. This has led researchers to focus on other areas of development, such as hybrid powertrains and energy recovery methods, as well as continuously variable transmissions, all of which have the intent of providing increased performance in the combined driving cycle. After over 100 years of development, the fundamentals of these engines are only beginning to change, with new fuels and combustion methods being the focus of development. One particular area of research investigates the use of hydrogen as a clean fuel due to its high energy density and low emissions characteristics.

Hydrogen has been investigated for use in a role as a stabiliser of the ignition and combustion processes occurring within traditional spark ignition and compression ignition internal combustion engines, such as gasoline or diesel engines. Hydrogen's resistance to extinction and ability to continually react under high strain rates provides many possibilities for its use in small quantities as an additive to traditional hydrocarbon fuels, improv-

ing the operating range and combustion characteristics of otherwise traditional engines. Development of novel engine concepts that utilise hydrogen as a primary fuel, for example the Homogeneous Charge Compression Ignition (HCCI) engine, requires an in-depth understanding of the processes that occur during mixing between fuel and air, as well as autoignition characteristics under varying operating temperatures, loads and pressures. At present, there is only a limited understanding of the interactions that occur within the new generation of engines; work is currently being done both numerically and experimentally to advance the state-of-the-art.

As a result, the primary focus of numerical research is currently oriented towards the development of mixing models that predict the complex interactions between fuel and oxidiser. Characterisation of the processes that are governed by turbulence as well as those governed by molecular mixing and diffusion processes are key to gaining an improved ability to predict the macroscopic trends occurring in these engines. Additionally, complex, multi-step chemical mechanisms must also be included with these mixing models to aid in the prediction of autoignition precursors and emission levels. The final implementation of these models within a numerical code ultimately needs to result in an application that is accurate, computationally inexpensive and easy to use.

## 1.2 Objectives

In an effort to reproduce some of the phenomena occurring within an internal combustion engine, different numerical and experimental methods have been attempted [1]. A large amount of recent work has focused on the implementation of the Conditional Moment Closure (CMC) model. This model shows great promise with more accurate prediction of ignition characteristics, but also presents numerical difficulties, such as increased computational time. The focus on further developing these models aims to provide an understanding of the strengths and weaknesses associated with this model, as well as providing a means to making the computations more attainable for a standard Computational Fluid Dynamics (CFD) end-user.

The focus of the present study is to provide an understanding of the performance of the CMC model in conjunction with hydrogen autoignition. Two molecular mixing models are tested and compared in order to provide insight into the effects of these models in

terms of accuracy and computational efficiency. These models are the Amplitude Mapping Closure (AMC) model [2] and a model based on the assumption of inhomogeneous turbulence [3]. To the author's best knowledge, the latter has not yet been applied in a finite volume formulation for autoignition problems. Additionally, the CFD code used in this study provides an option for "turning off" computationally expensive CMC calculations where they are unneeded, offering a significant increase in performance and accessibility of this model to more generic and unpredictable situations when it is not known a priori where the active CMC calculations are required.

### 1.3 Outline

In Chapter 2 the general background of fluid dynamics are covered. The relations presented serve as the basis for virtually all CFD simulations. The governing equations of fluid flow and various methods typically used for modelling turbulence are discussed. Various averaging techniques are discussed.

Following the outline of the CFD equations, Ch. 3 details the governing equations and implementation of the CMC model used in this work in detail. Included is a derivation of the finite volume inhomogeneous mixing model used in this study. The requirement for mixing models and closure of other terms within the CMC formulation are presented.

A review of previous numerical work is presented in Ch. 4. The experimental method and general results of the steady state flame used for initial validation of the CMC calculations is discussed. Following this, a review of the experimental work on the autoigniting flame used in the study is detailed. A summary of previous numerical studies and the respective findings is also provided.

Chapter 5 provides a further examination into the way the CFD model used in the current research has been implemented. Numerical solution methods and their implementation are discussed in further detail. A schematic outline of the CMC code used in this study is presented, explaining the coupling methods to link CMC and CFD calculations together. The detailed chemical mechanism and implementation of the mechanism into the solution is discussed. Solver methods used in the CFD and CMC calculations are also presented.

The focus of Chapter 6 is demonstrating the performance of the CFD/CMC code in

comparison with existing experimental data for steady flames. This includes the investigation of mixture fraction, temperature and rate of mixing documented in previous studies. A brief analysis of options within the CMC code will be discussed, which includes an investigation of combining multiple CFD cells into a single larger CMC cell and the use of a dynamic grid, activating/de-activating based on mean mixture fraction limits. A general analysis of the CFD results is presented and compared to the experimental trends seen. The overall performance of the CMC calculations in relation to experimental measurements is compared in detail with available conditional measurements.

Chapter 7 provides an investigation into the autoignition of hydrogen jets. In-depth details of the simulations performed in the current study are investigated, including boundary conditions, mesh and timestep refinement, and variation of model constants. The effect of the different mixing models is discussed in relation to various aspects of the CMC calculations as well as experimental results.

Conclusions based on this study are presented in Chapter 8. This includes a summary of all work performed and the findings of this study, as well as recommendations for future areas of study using the present computational code.

# Chapter 2

## Background

In this chapter, the fundamental equations governing thermodynamics and fluid flows are presented. Complete understanding of these equations and the subsequent models that arise for full closure in different simulation techniques is essential to the further understanding of the work presented in this study. The governing equations of fluid flow and thermodynamics provide an exact representation of processes governing the fluid properties. Each of the fundamental equations is presented in full detail, without the use of simplifications and assumptions. Following this, methods used to facilitate the use of these exact equations in a numerical application are discussed. This includes an overview of simulation types, averaging techniques, turbulence models and common combustion models, including many of the submodels required for closure.

### 2.1 Governing Equations of Fluid Flow

The governing equations of fluid dynamics can be separated into three general categories that control fluid motion and thermodynamics: conservation of mass (continuity), momentum and energy. For multicomponent flows, the species transport equation must also be solved, which can be seen as analogous to the continuity equation, but for a single species. Through the solution of these equations, the intensive and extensive properties can be determined. For simplicity, the following equations are written in Cartesian coordinates

using tensor notation.

### 2.1.1 Mass

The conservation of mass, or continuity equation as it is more commonly known, is given by:

$$\frac{\partial \rho}{\partial t} + \frac{\partial (\rho u_i)}{\partial x_i} = 0. \quad (2.1)$$

The first term given on the left hand side (LHS) of Eq. 2.1 is the rate of change of mass within the control volume, while the second term represents the convective mass transport. The right hand side (RHS) of the equation indicates that there are no sources or sinks for mass. When this value is positive, it indicates that mass is flowing into the system, and when negative, mass is leaving the system.

### 2.1.2 Momentum

The conservation of linear momentum equation relates any external body forces or pressures to density and velocity. The general conservation of linear momentum is given by:

$$\frac{\partial (\rho u_i)}{\partial t} + \frac{\partial (\rho u_i u_j)}{\partial x_i} = -\frac{\partial p}{\partial x_i} + \frac{\partial \tau_{ij}}{\partial x_j} + B_i, \quad (2.2)$$

where the first term on the LHS represents the local rate of change in momentum and the second term represents the convective change in momentum. The first term on the RHS is the pressure gradient acting on the fluid, the second term is the force due to the symmetric shear stress tensor and the last term on the RHS represents body forces, such as those due to gravity or magnetism.

The shear stress tensor,  $\tau_{ij}$ , is given by the equation

$$\tau_{ij} = \mu \left( \frac{\partial u_i}{\partial x_j} + \frac{\partial u_j}{\partial x_i} \right) - \mu \frac{2}{3} \frac{\partial u_k}{\partial x_k} \delta_{ij}. \quad (2.3)$$

The Kronecker delta,  $\delta_{ij}$ , is equal to 1 when  $i = j$ , and is equal to 0 when  $i \neq j$ . The turbulent viscosity is represented by  $\mu$ .

### 2.1.3 Enthalpy

The enthalpy of any fluid can be split into two separate components: the sensible enthalpy and the enthalpy of formation. Sensible enthalpy is a measure of the energy required to change the temperature from a base or reference state to another defined state. This is often represented by integrating the specific heat capacity for species  $\alpha$ ,  $c_{p,\alpha}$ , over the given change in temperature. The second component of enthalpy is typically referred to as the enthalpy of formation,  $h_{\alpha,ref}$ , and is a quantification of the energy contained within the chemical bonds of species. It is the changing of these bonds that results in energy liberation during a chemical reaction. Thus, the enthalpy of the fluid can be represented by the expression

$$h_{\alpha} = h_{\alpha,ref} + \int_{T_{ref}}^T c_{p,\alpha}(T) dT. \quad (2.4)$$

In a flow containing more than one species, the enthalpy of the flow is equal to the mass-weighted sum of the component enthalpies of species  $\alpha$ :

$$h = \sum_{\alpha=1}^{N_{\alpha}} Y_{\alpha} h_{\alpha}. \quad (2.5)$$

Similarly, the specific heat capacity of the mixture,  $c_p$ , is given by a mass weighted sum of the specific heat capacities of species  $\alpha$ :

$$c_p = \sum_{\alpha=1}^{N_{\alpha}} Y_{\alpha} c_{p,\alpha}. \quad (2.6)$$

Using this definition for enthalpy of the mixture, the transport equation for enthalpy within the system can now be defined. This is given by

$$\frac{\partial(\rho h)}{\partial t} + \frac{\partial(\rho u_i h)}{\partial x_i} = \frac{\partial p}{\partial t} + \frac{\partial(u_i p)}{\partial x_i} + \frac{\partial(u_i \tau_{ij})}{\partial x_i} - \frac{\partial}{\partial x_i} j_q + u_i B_i + \dot{q}_{rad}. \quad (2.7)$$

The terms on the LHS of Eq. 2.7 represent the rate of change in enthalpy and the convective enthalpy transport, respectively. The first two terms on the RHS of Eq. 2.7 represent the rate of change of pressure and the boundary work done by pressure. The third term on the RHS represents the work done by shear stresses. The term  $\dot{q}_{rad}$  represents radiative

heat transfer, and  $u_i B_i$  is a representation of work done by body forces. The diffusive heat flux,  $j_q$  is given by the expression

$$j_q = -\lambda \frac{\partial T}{\partial x_i} + \sum_{\alpha=1}^{N_\alpha} h_\alpha j_\alpha. \quad (2.8)$$

In Eq. 2.8  $\lambda$  is the thermal conductivity and  $j_\alpha$  is the diffusive heat flux represented by Fick's first law of diffusion as

$$j_\alpha = -\rho D_\alpha \frac{\partial Y_\alpha}{\partial x_i}, \quad (2.9)$$

with the diffusivity of species  $\alpha$  given by  $D_\alpha$  and the mass fraction of species  $\alpha$  given by  $Y_\alpha$ .

### 2.1.4 Species Transport

Similar to the concepts of having transport equations for intensive properties, it is also appropriate to use similar transport equations adapted for use with scalars. In reacting flows, it is of paramount importance to calculate the transport, production and destruction of the different chemical species present. Therefore, the governing equation of species  $\alpha$  is given by

$$\frac{\partial (\rho Y_\alpha)}{\partial t} + \frac{\partial (\rho u_i Y_\alpha)}{\partial x_i} = -\frac{\partial j_{i,\alpha}}{\partial x_i} + \dot{\omega}_{\alpha} \quad \alpha = 1, 2, \dots, N_s, \quad (2.10)$$

where  $N_s$  is the total number of species in the mixture. The chemical source term,  $\dot{\omega}_\alpha$ , is dictated by the chemical mechanism calculations. This will be discussed further in 5.3.

## 2.2 Averaging Techniques

The statistical description of laminar flows is trivial; since there are no random fluctuations, the flow can be completely characterised by the use of a mean scalar value which is dependant only on time and position. As a flow transitions from laminar to turbulent, small instabilities within the flow begin to have an effect on the larger flow structures. As a flow becomes fully turbulent, the effects of these small instabilities begins to have a

larger and larger effect on the flow. As a result, the analysis and characterisation for either scalars or vector quantities within turbulent flows become much more complicated; even steady turbulent flows cannot be defined by a mean value alone. The fluctuations about the mean value must also be defined in a process known as decomposition, where the mean value and an instantaneous fluctuation about the mean yield the instantaneous value [4]. It can be shown that both the mean values and fluctuations may be substituted into the governing equations while providing proper closure.

Two different types of averaging techniques are commonly used to address the need for scalar decomposition. The first type, Reynolds averaging, is commonly used in non-reacting flows where the density does not have large fluctuations. The second type, Favre-averaging, or density weighted averaging, is typically employed in flows where a large density change is expected, either due to various species present or large changes in temperature.

### 2.2.1 Reynolds Averaging

Quantities in turbulent flows may be decomposed into mean and fluctuating components. This can be represented for the quantity  $\psi$  as [4]

$$\psi(x_i, t) = \overline{\psi}(x_i, t) + \psi'(x_i, t), \quad (2.11)$$

where  $\psi(x_i, t)$  is the instantaneous value,  $\overline{\psi}(x_i, t)$  is the average value, and  $\psi'(x_i, t)$  is the magnitude of the fluctuation about the average. The use of decomposition within the governing equations allows separation of the mean and instantaneous values into different sets of governing equations. It can be shown that the continuity and momentum equations can be reduced to

$$\frac{\partial \overline{\rho}}{\partial t} + \frac{\partial (\overline{\rho u_i})}{\partial x_i} = 0 \quad (2.12)$$

$$\frac{\partial (\overline{\rho u_i})}{\partial t} + \frac{\partial (\overline{\rho u_i u_j})}{\partial x_i} = -\frac{\partial \overline{p}}{\partial x_i} + \frac{\partial \tau_{ij}}{\partial x_j} + \frac{\partial (\overline{\rho u'_i u'_j})}{\partial x_j} + B_i. \quad (2.13)$$

These equations are known as the Reynolds Averaged Navier-Stokes (RANS) equations. The new term present in Eq. 2.13,  $\frac{\partial (\overline{\rho u'_i u'_j})}{\partial x_j}$ , represents the Reynolds stresses. Reynolds

stresses are a measure of the internal shear due to velocity fluctuations within the flow. Closure of this term can be obtained using various turbulence models, some of which will be described in further detail in Section 2.3.

Similar to the treatment of the RANS equations, the scalar transport equation may be derived as follows

$$\frac{\partial (\bar{\rho}\bar{\psi})}{\partial t} + \frac{\partial (\bar{\rho}u_i\bar{\psi})}{\partial x_i} = \frac{\partial}{\partial x_i} \left( \bar{\rho}D_\psi \frac{\partial \bar{\psi}}{\partial x_i} \right) - \frac{(\bar{\rho}u'_i\psi')}{\partial x_j} + \dot{\omega}. \quad (2.14)$$

Equation 2.14 is analogous to both the RANS continuity and momentum equations; the source term is represented by  $\dot{\omega}$  and scalar fluctuations are represented by  $(\overline{u'_i\psi'})$ . These fluctuations are referred to as turbulent scalar fluxes.

## 2.2.2 Favre-Averaging

The majority of flows involving buoyancy, temperature changes or multiple chemical species produce large variations in density that cannot be neglected. For these flows, the density weighted averaging, or Favre-averaging method is preferred [5]. The process of Favre-averaging takes into account density variations within the flow when calculating mean values, such that the Favre-averaged value is

$$\tilde{\psi}(x_i, t) = \frac{\overline{\rho\psi}(x_i, t)}{\bar{\rho}}. \quad (2.15)$$

Decomposition can occur in a similar fashion to Reynolds averaging, as shown in Eq. 2.12 through Eq. 2.14. Once again, the instantaneous value of the quantity  $\psi$  is equal to

$$\psi(x_i, t) = \tilde{\psi}(x_i, t) + \psi''(x_i, t). \quad (2.16)$$

Using the decomposition method shown in Eq. 2.16, a set of Favre-averaged governing equations may be obtained:

$$\frac{\partial \bar{\rho}}{\partial t} + \frac{\partial (\bar{\rho}\tilde{u}_i)}{\partial x_i} = 0, \quad (2.17)$$

$$\frac{\partial (\bar{\rho}\tilde{u}_i)}{\partial t} + \frac{\partial (\bar{\rho}\tilde{u}_i\tilde{u}_j)}{\partial x_i} = -\frac{\partial \bar{p}}{\partial x_i} + \frac{\partial \tau_{ij}}{\partial x_j} + \frac{\partial (\bar{\rho}\widetilde{u''_i u''_j})}{\partial x_j} + B_i, \quad (2.18)$$

$$\frac{\partial (\overline{\rho\tilde{\psi}})}{\partial t} + \frac{\partial (\overline{\rho\tilde{u}_i\tilde{\psi}})}{\partial x_i} = \frac{\partial}{\partial x_i} \left( \overline{\rho} D_\psi \frac{\partial \tilde{\psi}}{\partial x_i} \right) - \frac{\partial (\overline{\rho u_i'' \psi''})}{\partial x_j} + \dot{\omega}. \quad (2.19)$$

## 2.3 Turbulence Modelling

In reaching the RANS equations, Eqs. 2.12 - 2.14, it was observed that one term involving turbulent fluctuations remained without adequate closure. This term, the Reynolds stress tensor, poses many of the difficulties encountered in the modelling of turbulent flows. In order to provide closure for this term, many different models and methods have been suggested. Within the RANS equations, these models are usually defined by the number of additional transport equations required for closure, such as 0-equation, 1-equation and 2-equation. These models are linked to the Reynolds stress tensor via an approximation known as the turbulent viscosity hypothesis [4]. In addition to these turbulent viscosity based models, another frequently encountered model is the Reynolds stress model, which attempts to resolve each of the individual stresses in the Reynolds stress tensor.

Instead of using the RANS equations, several additional techniques have grown in popularity recently. These techniques are known as Large Eddy Simulation (LES) or Direct Numerical Simulation (DNS). As the name suggests, LES involves modelling the larger turbulent eddies present in the flow. Instead of using averaged values, as with RANS, LES uses filtered governing equations while providing models for lower energy length scales within the flow. DNS takes this one step further by resolving the entire energy cascade, including even the smallest flow structures. The drawback to this increased resolution is the dramatic increase in computational cost. LES typically requires much finer grid spacing than RANS simulations, often requiring a significant amount of parallel computing power. The increase in computational cost for DNS is so dramatic that contemporary supercomputers are only able to simulate low Reynolds number (Re) flows in extremely small domains, on the order of centimeters. Although computing power has maintained an exponential growth, the widespread use of LES and DNS for practical engineering problems is still several years from reality.

The following section will investigate turbulence modelling in RANS simulations, LES and DNS.

### 2.3.1 Reynolds Averaged Navier-Stokes Simulations

RANS modelling involves solving the averaged Navier-Stokes equations presented in Section 2.2.1. Since the Reynolds stress term remains unclosed, turbulence models must be used to provide closure for this term using a turbulent viscosity model or a direct model. The turbulent viscosity based models may be subdivided into 0-equation, 1-equation or 2-equation models. The order of the model refers to the number of additional transport equations required for closure. An additional, more direct model exists that does not rely on turbulent viscosity, providing an additional transport equation for each of the unclosed Reynolds stresses.

#### Turbulent Viscosity Hypothesis

Before discussing the models further, it is important to outline the turbulent viscosity hypothesis upon which the 0, 1 and 2 equation models rely. The turbulent viscosity hypothesis, presented by Boussinesq in 1877, assumes that the Reynolds stresses are determined by the mean velocity gradients, much in the same way as viscous stresses are related to the bespoke velocity gradients [4]. This is shown as

$$\overline{\rho u'_i u'_j} = -\mu_t \left( \frac{\partial \overline{u}_i}{\partial x_j} + \frac{\partial \overline{u}_j}{\partial x_i} \right) - \frac{2}{3} \overline{\rho} \delta_{ij} \overline{k}. \quad (2.20)$$

The second assumption is that the Reynolds stress anisotropy,  $a_{ij}$  is governed by the relationship

$$a_{ij} = -2\nu_T \overline{S}_{ij}, \quad (2.21)$$

where  $\overline{S}_{ij}$  is the mean rate of strain tensor. These relations have been shown to be inaccurate in many flows; however, for simple shear flows, the turbulent viscosity hypothesis is somewhat reasonable.

#### 0-Equation Models

Perhaps the simplest of all turbulence models is the zero equation model. As the name suggests, there are no additional transport equations required for closure, rather, a simple

relation combined with assumptions about length scales present in the flow is used to determine the turbulent viscosity. This model, commonly referred to as the mixing length model was initially introduced by Prandtl [6]. It is assumed that the kinematic turbulent viscosity,  $\nu_T$ , is the product of a turbulent velocity scale and an assumed mixing length scale,  $l_m$ . Upon simplification of the model, it can be shown that

$$\nu_T = l_m^2 \left| \frac{\partial u_i}{\partial x_j} \right|. \quad (2.22)$$

Further manipulation of Eq. 2.22 will yield a form suitable for implementation as the Reynolds stress term in the closure of the Navier-Stokes equations. Therefore, the Reynolds stresses can be described by

$$\tau_{ij} = \tau_{ji} = -\overline{\rho u'_i u'_j} = \rho l_m^2 \left| \frac{\partial u_i}{\partial x_j} \right| \frac{\partial u_i}{\partial x_j}. \quad (2.23)$$

Although this model is computationally inexpensive and easy to implement, the accuracy of the simulations are completely dependent on selection of an appropriate length scale [4, 6]. An implication of this model is that the velocity scale is locally calculated by the gradient. There are, however, some circumstances where this is not true, such as in the centre of a round jet or decaying grid turbulence [4]. As a result of these uncertainties and potential inaccuracies, this model is not frequently used for industrial flows.

## 1-Equation Models

The implementation of a 1-equation model represents an evolution of the zero equation models. The further development of this model yields a dynamic specification of the velocity length scale that is not dependent on shear only. This model introduces the concept of turbulent kinetic energy. Kolmogorov and Prandtl suggested that the velocity scale should be dependent on the turbulent kinetic energy, such that

$$u^* = ck^{\frac{1}{2}}, \quad (2.24)$$

where the turbulent kinetic energy (TKE),  $k$ , is given by [7, 1]

$$k = \frac{1}{2} \widetilde{u_i'^2}. \quad (2.25)$$

Similar to the zero equation model, the length scale is once again assumed to be constant. Therefore, the turbulent kinematic viscosity is given by

$$\nu_T = ck^{\frac{1}{2}}l_m, \quad (2.26)$$

with  $c$  usually taken as 0.55.

Since the turbulent kinetic energy is a spatial (and temporal, if unsteady flow) dependent term, an additional transport equation must be introduced for calculation of this term. This transport equation is given as

$$\bar{\rho} \frac{\partial \tilde{k}}{\partial t} + \bar{\rho} u_k \frac{\partial \tilde{k}}{\partial x_k} = \frac{\partial}{\partial x_k} \left[ \left( \frac{\mu_t}{\sigma_k} + \mu \right) \frac{\partial \tilde{k}}{\partial x_k} \right] + \bar{\rho} P - \bar{\rho} \tilde{\epsilon}, \quad (2.27)$$

where  $\tilde{\epsilon} = C_d k^{\frac{3}{2}}/l_m$ ,  $\sigma_k$  is the the turbulent Prandtl number,  $C_d$  is an empirical constant, usually set equal to 0.09 and  $P$  is the turbulent production rate. The production rate is modelled using

$$P = -\widetilde{u_i'' u_j''} \frac{\partial \tilde{u}_j}{\partial x_i} \quad (2.28)$$

where

$$\widetilde{u_i'' u_j''} = \frac{2}{3} \delta_{ij} \left( \tilde{k} - \frac{\mu_T}{\bar{\rho}} \frac{\partial \tilde{u}_k}{\partial x_k} \right) - \frac{\mu_T}{\bar{\rho}} \left( \frac{\partial \tilde{u}_i}{\partial x_i} + \frac{\partial \tilde{u}_J}{\partial x_K} \right). \quad (2.29)$$

Although this model does present a slightly more physical representation of the turbulent processes than the zero equation model, it is still plagued by some of the same limitations, namely the specification of a fixed turbulent length scale.

## 2-Equation Models

A group of two equation models are in widespread use throughout most commercial CFD codes. These models, while requiring slightly more computational expense, provide a large improvement in accuracy in addition to an excellent understanding of the limitations associated with the model. These models typically do not require anything more than specification of a few constants which remain similar for many flows. Building on the TKE transport equation introduced for the 1-equation model, a second transport equation

is introduced, providing a means of calculating the length scale required by the turbulent viscosity hypothesis for closure of the Reynolds stresses. The most widely used two equation models are the  $k - \omega$  proposed by Wilcox et al. [8] and the  $k - \epsilon$  model proposed by Jones et al. [7]. This section will focus on the implementation of the latter, as it is used in the current study.

The  $k - \epsilon$  model is perhaps the most widely documented and best understood of the RANS turbulence models [4, 6]. The implementation of this model is achieved by using the aforementioned turbulent kinetic energy equation, shown in Eq. 2.25 and introducing a second transport equation for dissipation,  $\epsilon$ , which is subsequently used to calculate the turbulent length scale.

The dissipation equation is given as

$$\bar{\rho} \frac{\partial \tilde{\epsilon}}{\partial t} + \bar{\rho} u_k \frac{\partial \tilde{\epsilon}}{\partial x_k} = \frac{\partial}{\partial x_k} \left[ \left( \frac{\mu_T}{\sigma_\epsilon} + \mu \right) \frac{\partial \tilde{\epsilon}}{\partial x_k} \right] + C_{\epsilon 1} \bar{\rho} P \frac{\partial \tilde{\epsilon}}{\partial k} - C_{\epsilon 2} \bar{\rho} \frac{\tilde{\epsilon}^2}{k}, \quad (2.30)$$

with

$$\mu_T = C_\mu \bar{\rho} \frac{\tilde{k}^2}{\tilde{\epsilon}}. \quad (2.31)$$

The standard model constants, first proposed by Launder and Sharma [9], are given as

$$C_\mu = 0.09, \quad C_{\epsilon 2} = 1.44, \quad C_{\epsilon 1} = 1.92, \quad \sigma_k = 1.0, \quad \text{and} \quad \sigma_\epsilon = 1.3. \quad (2.32)$$

Equations 2.30 and 2.31 can be used to derive the turbulent length and time scales for the flow:

$$l_m = \frac{\tilde{k}^{\frac{3}{2}}}{\tilde{\epsilon}}, \quad (2.33)$$

and

$$\tau = \frac{\tilde{k}}{\tilde{\epsilon}}. \quad (2.34)$$

The  $k - \epsilon$  equation has many well known deficiencies [4, 6]; however, knowledge of its shortcomings only further encourages its use. For example, it is well documented that this model will overpredict the spreading of round jets, which leads to a subsequent reduction in penetration length. Modification of the  $C_{\epsilon 1}$  and  $C_{\epsilon 2}$  constants is a common way of compensating for these deficiencies, and has been used in previous studies [10, 11].

## Reynolds-Stress Model

The Reynolds-stress model differs from the 0-, 1- and 2-equation models in that it does not use an eddy viscosity approximation to determine the Reynolds-stresses [4]. Instead, a group of 6 additional transport equations are introduced into the calculation in order to resolve the Reynolds-stress tensor. The equations take the form

$$\frac{\partial}{\partial t}(\overline{\rho u'_i u'_j}) + \frac{\partial}{\partial x_i}(\overline{\rho u'_i u'_j u'_k}) = \frac{\partial}{\partial x_k} \left[ \left( \nu + \frac{2}{3} C_s \frac{\tilde{k}^2}{\tilde{\epsilon}} \right) \frac{\partial \overline{u'_i u'_j}}{\partial x_k} \right] + P_{ij} + \phi_{ij} - \frac{2}{3} \delta_{ij} \tilde{\epsilon}. \quad (2.35)$$

In the above equation,  $P_{ij}$  is the exact production term,  $\phi_{ij}$  is the pressure strain correlation, and  $C_s$  is a model constant.

Due to the increase in computational cost, the Reynolds-stress model is infrequently used compared to simpler two-equation models, such as the  $k - \epsilon$  model [6]. In addition to the increased complexity, some of the same limitations seen with the  $k - \epsilon$  model present themselves. Further explanation of this model is not relevant to the current study; however, details of the model and its implementation may be found in [4, 6].

### 2.3.2 Large Eddy Simulation

Large Eddy Simulation (LES) is one of the methods that has been increasing in popularity over the past several years, mainly due to the increase in parallel computing power. This model, although extremely computationally expensive in comparison to simpler RANS models, does present some advantages as well as disadvantages.

Instead of decomposing the flow into mean and fluctuating values, a filter is applied to yield an instantaneous and residual value. The instantaneous values, which by the nature of LES must be obtained by unsteady simulation even for steady flows, represent the larger flow structures that would be entirely modelled within RANS. These larger eddies which are fully resolved do potentially provide useful information when modelling combustion processes: the unsteady nature of combustion processes often depends on temporal fluctuations which are lost in RANS simulations [12]. The flow structures which are too small to be resolved in LES are modelled by various models, further discussed in [4].

Although the benefits of LES are attractive, they do come at a significant computational cost. The filter width in LES is proportional to the grid spacing, which must be

chosen such that the filter width is located within the inertial subrange of the flow [4]. This reduced grid spacing, with all else being equal, leads to a smaller timestep in order to maintain the Courant number of the simulation [6]. Another compounding factor relevant to this study is that LES are necessarily 3-dimensional flows, even for axisymmetric domains, whereas RANS can be reduced to a two dimensional axisymmetric slice one cell thick. When combined, these factors lead to the significant increase in computational cost, which at present makes LES somewhat impractical for many industrial applications. However, one must consider that due to the steady increases in computational power, this may not always be the case.

### **2.3.3 Direct Numerical Simulation**

A further refinement of LES is direct numerical simulation (DNS). In contrast to LES and RANS, DNS does not use any filtering or modelling of flow patterns; instead, even the smallest length scales at which energy dissipation occurs are resolved. The implications of this are similar in nature to those experienced with LES; the grid spacing must be further refined and timesteps further decreased in order to maintain numerical accuracy and stability [4]. As a result, massive amounts of computing power are required for low-Re simulations, and it is currently impractical to model high Re flows. DNS studies are restricted to determining flow statistics and providing data for validation of simpler models. Further information can be found in [4, 6].

## **2.4 Stochastic Description of Flows**

In Section 2.3.1, it was shown that a flow can be broken down into a mean value and a fluctuation. Since these fluctuations are only modelled, and not resolved, it is key to provide a statistical description of the flow. This description allow it to be said with some probability whether an instantaneous value, the sum of the mean and the fluctuation, will fall within a certain range. Therefore, one must rely on stochastic methods with which the flow can be described.

As an example, a variable,  $\Phi$ , may take on values within the valid range of the sample space variable,  $\phi$ . Although  $\Phi$  is able to take on any value within the sample space, the likelihood of  $\Phi$  falling within a certain range can be characterised by use of a probability density function (PDF) or cumulative distribution function (CDF) [4, 13]. Use of statistical methods, although not able to predict exact values of variables, allows the value, or range of values, to be stated with a level of confidence. The level of confidence is related to the width of the range, and the randomness of the field.

In the simplest sense, the cumulative probability of  $C(\Phi < \phi)$  is defined as the probability of occurrence of  $\Phi$  such that  $\Phi < \phi$ . Even though this statement seems relatively simple and intuitive, its implications are extremely important. The value of  $\phi$  can be selected to be sufficiently small such that  $\Phi < \phi$  is never true, or sufficiently large that  $\Phi < \phi$  is always true. The resultant probabilities will then be 0 and 1, respectively. As a result, the function  $C$  is continually increasing, bounded by 0 and 1. Subsequently, for a given range defined by the sample variables  $\phi_1$  and  $\phi_2$ ,  $C(\phi_1 < \Phi < \phi_2) = C(\Phi < \phi_2) - C(\Phi < \phi_1)$ .

An alternative way to represent the probability is via a probability density function. The PDF,  $P$ , is defined as the derivative of the CDF

$$P(\phi) = \lim_{\delta\phi \rightarrow 0} \frac{C(\Phi < \phi + \delta\phi) - C(\Phi < \phi)}{\delta\phi} = \frac{dC(\Phi < \phi)}{d\phi} \quad (2.36)$$

such that

$$\int_{-\infty}^{+\infty} P(\phi) = 1. \quad (2.37)$$

When used to describe random variables, the PDF can be easily employed to calculate the mean or the variance of the variable. These values become extremely useful when only the statistical behaviour of a variable is available but further details are required. The mean, or expected value of the variable  $\Phi$  is then defined by

$$\langle \Phi \rangle \equiv \int_{-\infty}^{+\infty} \phi P(\phi) d\phi. \quad (2.38)$$

Similarly, this expression can be used to define the mean of any function of  $\phi$ ,  $f(\Phi)$  as

$$\langle f(\Phi) \rangle \equiv \int_{-\infty}^{+\infty} f(\phi) P(\phi) d\phi. \quad (2.39)$$

Based on the preceding analysis, the dependence of a variable on a single random variable may be extended to two or more random variables using Bayes' theorem [14]. The resultant PDF is typically known as a joint PDF, and is defined as [4, 14, 13]

$$P(\phi_1, \phi_2) = P(\phi|\Phi_2 = \phi_2) P(\phi_2), \quad (2.40)$$

in which  $P(\phi|\Phi_2 = \phi_2)$  is the probability of  $\Phi_1$  having a value of  $\phi_1$  for all scenarios where the condition of  $\Phi_2 = \phi_2$  is satisfied. The conditional expectation can subsequently be defined as

$$\langle \Phi_1 | \Phi_2 = \phi_2 \rangle = \frac{\int_{-\infty}^{+\infty} \phi_1 P(\phi_1 | \Phi_2 = \phi_2) P(\phi_2) d\phi_2}{P(\phi_2)}. \quad (2.41)$$

Likewise, for any function,  $f(\Phi_1)$ , the conditional expectation may be defined as

$$\langle f(\Phi_1) | \Phi_2 = \phi_2 \rangle = \frac{\int_{-\infty}^{+\infty} f(\phi_1) P(\phi_1 | \Phi_2 = \phi_2) P(\phi_2) d\phi_2}{P(\phi_2)}. \quad (2.42)$$

## 2.5 Turbulent Reacting Flows and Non-premixed Combustion

Flows in which a reaction occurs become greatly complicated by the additional processes taking place. The Navier-Stokes equations, although still valid, must be supplemented to fully account for the effects of reactions occurring within the fluid. This matter is greatly complicated by the fact that there is, even still, a limited understanding of the full kinetics and governing rates of chemical mechanisms and all of the interactions that take place within. Further compounding the level of complexity is the fact that instead of a single fluid species, reactions now require potentially hundreds of intermediate species in addition to the reactants and products to be accounted for to fully and accurately define a process.

The difficulties associated with predicting combustion processes, a subset of the field of reacting flows, stem from the uncertainties associated with mixing, temperature dependent rates and providing simplified models to more efficiently evaluate the required information. This section will provide a further discussion of some basic modelling assumptions and techniques, as well as providing some common models used to predict combustion.

### 2.5.1 Damköhler Number

It is widely understood, even to the layman without any technical background, that combustion processes have the potential occur extremely quickly. Without this speed of reaction, many of the devices upon which we rely daily would be completely different, if not impossible. An excellent example of this is the automotive internal combustion engine, which requires a fast, yet controlled, burning of the fuel in order to operate properly. At the same time, turbulent mixing is also occurring within these processes. The ratio between the chemical and turbulent timescales has a very large impact on the way analysis must be conducted for reacting flows. The ratio between these timescales is known as the Damköhler number, or  $Da$  [15]. This non-dimensional number is a measure of the relative rate of chemical reaction and turbulent mixing processes.

$$Da = \frac{\tau_t}{\tau_c}. \quad (2.43)$$

For flows in which the Damköhler number is greater than 1, reactions occur faster than the turbulent mixing. For flows in which the Damköhler number is less than 1, turbulent mixing occurs faster than the chemical reaction. Use of this number is extremely relevant to modelling of non-premixed reacting flows: if the value of  $Da$  is sufficiently large (i.e.  $Da \gg 1$ ), a 1-step, infinite rate reaction can be assumed with little impact on the overall results [16]. This situation corresponds to what is commonly known as a well-stirred reactor. Conversely, when the value of  $Da$  is small, (i.e.  $Da \ll 1$ ), the effects of the chemical mechanism have a large impact on the flow [16].

### 2.5.2 Mixture Fraction

The concept of mixture fraction is one of the key ideas required for successful evaluation of turbulent reacting flows. The mixture fraction,  $\xi$ , is a normalised scalar that is used to represent the relative amounts of fuel and oxidiser present in a given parcel of fluid. It is defined as the local ratio of mass originating from the fuel to the total mass of the mixture

$$\xi = \frac{\text{mass originating from fuel}}{\text{total mass of mixture}} \quad (2.44)$$

In order to properly use the variable  $\xi$  given in Eq. 2.44, all non reacting elements that are present in the fuel *must* be accounted for in addition to those participating in the reaction,

otherwise the results will be inaccurate.

For a two-feed system, where fuel and oxidiser are supplied by separate means, mixture fraction is defined as [1]

$$\xi = \frac{\dot{m}_f}{\dot{m}_f + \dot{m}_o}, \quad (2.45)$$

where  $\dot{m}_f$  represents the mass flow of the fuel stream and  $\dot{m}_o$  represents the mass flow of the oxidiser stream. If it is assumed that the diffusivities for all species are equal, or that the mixing in the flow is governed by turbulence, the mixture fraction can be considered as a conserved scalar (due to the conservation of mass), and is governed by the transport equation

$$\frac{\partial (\rho\xi)}{\partial t} + \frac{\partial}{\partial x_i} (\rho u_i \xi) = \frac{\partial}{\partial x_i} \left( \rho D \frac{\partial \xi}{\partial x_i} \right). \quad (2.46)$$

In Eq. 2.46, there are no sources or sinks included. Transport of the mixture fraction scalar is entirely dependent on convective and diffusive means.

As shown previously in Section 2.2.2, for reacting flows it becomes necessary to use a density weighted approach for solution of the transport equations. Eq. 2.46 may be Favre-Averaged to yield

$$\frac{\partial (\bar{\rho}\tilde{\xi})}{\partial t} + \frac{\partial}{\partial x_i} (\bar{\rho}u_i\tilde{\xi}) = \frac{\partial}{\partial x_i} \left( \bar{\rho}D_t \frac{\partial \tilde{\xi}}{\partial x_i} - \bar{\rho}\widetilde{u_i''\xi''} \right). \quad (2.47)$$

In this equation, molecular diffusion processes are neglected by assuming a high Re flow. The turbulent flux term,  $\widetilde{u_i''\xi''}$ , is modelled using the gradient diffusion hypothesis

$$\widetilde{u_i''\xi''} = -D_t \frac{\partial \tilde{\xi}}{\partial x_i}. \quad (2.48)$$

In addition to mean mixture fraction transport, the proper treatment of the mean mixture fraction variance,  $\widetilde{\xi''^2}$ , also requires the use of a similar transport equation. The mean mixture fraction variance transport equation is given by

$$\frac{\partial (\bar{\rho}\widetilde{\xi''^2})}{\partial t} + \frac{\partial}{\partial x_i} (\bar{\rho}\widetilde{u_i\xi''^2}) = -\frac{\partial}{\partial x_i} (\bar{\rho}\widetilde{u_i''\xi''^2}) + 2\bar{\rho}D_t \left( \frac{\partial \tilde{\xi}}{\partial x_i} \right)^2 - \bar{\rho}\tilde{\chi}. \quad (2.49)$$

Again, the turbulent flux term,  $\widetilde{u_i''\xi''^2}$ , in Eq. 2.49 is modelled using the gradient diffusion hypothesis. The effects of the mean scalar dissipation rate,  $\tilde{\chi}$ , will be discussed in 2.5.3

and in further detail in Chapter 3.

Following the solution of the mean mixture fraction and its variance, a presumed form PDF can now be defined. Use of a presumed form PDF will be covered in further detail in Chapter 3.

### 2.5.3 Mean Scalar Dissipation Rate

The mean scalar dissipation rate,  $\tilde{\chi}$ , is a measure of the level of mixing present in a turbulent flowfield. It can influence many characteristics of reacting flows, such as temperature, ignition and extinction processes. A very small value of  $\tilde{\chi}$  means that combustion processes are occurring at conditions close to equilibrium, while a very high  $\tilde{\chi}$  is indicative of a highly strained flame that is close to extinction [6]. As the scalar dissipation rate increases, more heat is removed from the reaction zone, subsequently lowering the rate of reaction and fluid temperature. If the value of  $\tilde{\chi}$  exceeds a certain threshold,  $\tilde{\chi}_{extinction}$ , the chain reactions controlling combustion can no longer continue and the flame is extinguished. Since the value of  $\tilde{\chi}_{extinction}$  is directly related to diffusion of the fuel within the oxidiser, fuels with high diffusivities such as hydrogen are able to withstand much higher scalar dissipation rates without extinction.

An expression for the closure of the mean scalar dissipation rate,  $\tilde{\chi}$ , was developed by Peters [1]. An integral timescale for the mixing field can be defined as

$$\tau_i = \frac{\tilde{\xi}''^2}{\tilde{\chi}}, \quad (2.50)$$

while for the flow, the time scale is

$$\tau = \frac{\tilde{k}}{\tilde{\epsilon}}. \quad (2.51)$$

Invoking the assumption of proportionality of timescales, a constant of proportionality of the order of unity may be obtained [1]. This can be shown as

$$\tau = C_\chi \tau_i \quad (2.52)$$

Upon substitution of Equations 2.50 and 2.51 into Equation 2.52, the following relation for mean scalar dissipation rate is obtained

$$\tilde{\chi} = C_\chi \frac{\tilde{\epsilon}}{\tilde{k}} \tilde{\xi}''^2 \quad (2.53)$$

The value of the constant of proportionality is entirely dependent on the flow. Janicka and Peters [17] found that a value of  $C_\chi = 2.0$  provides good performance when considering an inert methane jet. Various other models have been suggested for closure of the mean scalar dissipation rate [4]; however, they are not used in the current implementation of the CMC equations and are beyond the scope of the present work.

## 2.6 Turbulent Combustion Models

Similar to the turbulence models discussed in Section 2.3, it is necessary to provide modelling for proper closure of the enthalpy and chemical species transport equations. Once again, similar to turbulence modelling, a wide array of modelling techniques exist, ranging from the simple to very complex. Proper application requires a great amount of knowledge of both the applicable flow and the features of the model being used. This section provides an overview of the Eddy Break-up Model (EBU) [18], the Laminar Flamelet model (LF) [6] and the PDF Transport Model [19]. The CMC combustion model is presented in greater detail in Ch. 3.

### 2.6.1 Eddy Break-up Model

The Eddy Break-Up model (EBU) was first proposed by Spalding [18] as a method of obtaining closure for the chemical source term. In this model, the rate of consumption of reactants is governed by the level of turbulent mixing in the flow. The mixing-controlled rate of reaction can be expressed in terms of the turbulent time scale, which is defined by the ratio of the turbulent kinetic energy to the dissipation rate,  $k/\epsilon$ . It is assumed that the chemistry is infinitely fast, and that the reaction rate is only governed by turbulent mixing. The initial intent of the model was to address premixed combustion processes; however, by calculating the mixture fraction PDF, the EBU model can be adapted for use with non-premixed combustion. The reaction rates for the fuel, oxidiser and products, which are proportional to the turbulent dissipation rate, may be expressed as

$$\tilde{\omega}_{fuel} = -C_R \bar{\rho} \tilde{Y}_{fuel} \frac{\epsilon}{k}, \quad (2.54)$$

$$\tilde{\omega}_{ox} = -C_R \bar{\rho} \frac{\tilde{Y}_{ox}}{s} \frac{\epsilon}{k}, \quad (2.55)$$

and

$$\tilde{\omega}_{pr} = -C'_R \bar{\rho} \frac{\tilde{Y}_{pr}}{1+s} \frac{\epsilon}{k}. \quad (2.56)$$

In these equations,  $s$  represents the stoichiometric oxygen to fuel mass ratio,  $Y$  is the mass fraction and  $C_R$  and  $C'_R$  are model constants. Typical values for the model constants are  $C_R = 1.0$  and  $C'_R = 0.5$  [6], although some fine tuning may be required to yield the proper results [4]. Since the rate equations are directly tied together via the conservation of mass, the rate determining equation is taken as the minimum of the three, such that

$$\tilde{\omega}_{fuel} = -\bar{\rho} \frac{\epsilon}{k} \min \left[ C_R \tilde{Y}_{fuel}, C_R \frac{\tilde{Y}_{ox}}{s}, C_R \frac{\tilde{Y}_{pr}}{1+s} \right]. \quad (2.57)$$

Since the reaction rate is entirely dependent on the quantities  $\epsilon$  and  $k$ , the overall performance of the combustion model hinges on successful and accurate modelling of the turbulence. It is worth noting that only the bulk reaction rates are considered, the evolution of intermediate species are not considered.

## 2.6.2 Laminar Flamelet Model

The laminar flamelet model is a relatively simple model that combines computational efficiency with some aspects of detailed chemistry. In this model, a high Damköhler number and fast chemistry are assumed. Reaction is limited to a thin sheet positioned approximately parallel to the surface contour defined by stoichiometry. The impact of turbulence results in a wrinkled sheet of reaction that is embedded within the turbulent structures [6]. These reaction structures are known as flamelets.

The effects of varied chemical mechanisms are included in the calculation by providing a series of flamelet libraries. Each of these flamelet libraries is pre-calculated for discrete mixture fraction points and turbulent mixing levels, defined by the scalar dissipation rate,  $\chi$ , or the strain rate. The tables are generated by solving the one-dimensional governing equations for non-premixed combustion for various levels of mixing.[6]. Interpolation is

then used between the available libraries during the simulation, providing quick, computationally inexpensive and reasonably accurate chemical interactions. The pre-calculation of the tables allows for prediction of intermediate species concentrations and pollutant formation, as well as using complex chemical mechanisms that would be otherwise impractical or inefficient for full simulations.

The additional computational cost is minimal. Aside from the pre-generated flamelet libraries, there is no need for full transport equations for the various chemical species included in the mechanism; the only additional parameters required during simulation are the transport equations for mean mixture fraction and mean mixture fraction variance to complete the lookup. The enthalpy equation is necessarily coupled with the flamelet library to provide the temperature increases associated with species evolution and reaction [6].

Due to the reliance on pre-generated tables, the accuracy of these simulations is heavily dependent on the resolution in mixture fraction space and the amount of different mixing levels that are specified. Additionally, the applicability of this model is limited when the assumption of  $Da \gg 1$  is not true or if the reaction zone is thicker than the Kolmogorov length scale of the flow, i.e. the timescales of combustion must be very small in comparison to the mixing timescales associated with the flow. This makes the laminar flamelet model unsuitable for the prediction of autoignition or flames with large chemical timescales.

### 2.6.3 Lagrangian PDF Transport Model

The Lagrangian PDF transport model was initially developed by Pope in 1994 [19], and can be used for both premixed and non-premixed combustion. This method results in computational cost well in excess of the EBU and laminar flamelet models; however, it does not rely on some of the assumptions made for convective transport in other models. It is assumed that in a high Reynolds number flow, the transport equations are dominated by convection, and the diffusive processes have little overall impact. As a result, imaginary particles are introduced into the flow, each of which has its own set of properties for position, velocity, species concentrations etc. Monte Carlo methods are used in the simulation of the particle distributions. Use of particles instead of fluid parcels allows the fluid flow to be modelled without invoking the gradient diffusion hypothesis used traditionally

for closures of the RANS equations.

The overall performance of the PDF model is dependent on the models chosen for the unclosed terms in the PDF transport equation. As this equation does not account for scalar gradients, suitable closures are still required for viscous and molecular mixing terms. Proper modelling of the mixing term is important in PDF methods. Modelling of the mixing term also presents one of the largest difficulties in application of this method. One of the largest benefits of the PDF model is that the chemical reaction rate is presented in closed form, and no further modelling is required. Additional information about the derivation and formulation of the PDF transport equation can be found in reference [4].

## 2.7 Summary

In this chapter, much of the background information required for understanding of the general modelling techniques used in this study has been presented. The governing equations for fluid flow, including conservation of mass, momentum and energy have been given in their general form as well as in the Reynolds-averaged form. The technique of Favre-averaging, important for the proper treatment of reacting flows, was also introduced in conjunction with the Favre-averaged Navier-Stokes equations. Typical turbulence modelling techniques for the RANS set of equations were covered with general model details. Additionally, basic combustion models and the concept of mixture fraction was also introduced. The following chapter, Ch. 3, covers the general concepts used for the Conditional Moment Closure model, including required closures and relevant models.

# Chapter 3

## Conditional Moment Closure

In this chapter, Conditional Moment Closure (CMC) along with the required submodels and closures are introduced. A general derivation of the equations required for the model, including the details on terms requiring closure is presented as background information.

The CMC model lies between the flamelet model and PDF methods in terms of modelling assumptions and computational cost. The reduced complexity compared with PDF methods combined with increased accuracy over flamelet models makes CMC an attractive option for combustion modelling.

### 3.1 Overview

As it was examined in Section 2.5, there are many available methods of addressing the complex phenomenon of turbulent combustion. The complexity of these models, as well as their accuracy and ease of use is varied, and is often related to the assumptions made during the formulation of the model. One combustion modelling approach that has been gaining popularity in recent years is CMC. This method was developed independently by Klimenko [20] and Bilger [21], and published in a joint paper [13].

One of the largest difficulties arising when predicting combustion or other reacting flows, is accurately representing the non-linearities in the species concentration and temperature equations. The goal of CMC is to provide closure of turbulence-chemistry interactions

without  $Da$  restrictions posed by other combustion models, such as the laminar flamelet model. CMC also allows easy provision of detailed chemistry mechanisms. In implementing the CMC model, transport equations for chemical species and enthalpy are conditionally averaged. Consequently, an additional conditioning variable is introduced into the solution in the form of mixture fraction. Fluctuations about the conditional averages are much smaller than the fluctuations about the unconditional averages. In first-order CMC, used in the present study, these fluctuations are neglected, reducing the complexity of the transport equations required to be solved.

Although Klimenko and Bilger derived the CMC equations independently and from different starting points, the end result is the same. Klimenko's approach began with the PDF transport equation under high Reynolds number (Re) flows, and is therefore often referred to as the joint-PDF method. Bilger used a decomposition approach very similar to that used with turbulent fluctuations, with the instantaneous values separated into a mean and fluctuation [21]. The following analysis will follow the decomposition approach of Bilger.

## 3.2 Conditional Species Transport Equation

Although the mixture fraction transport equation is one of the key requirements of CMC, since mixture fraction space is a dimension added to the analysis, it is still required that each species have a transport equation in order to provide the species concentrations required for the subsequent chemistry calculations. Therefore, for species  $\alpha$ , the conditional average of the mass fraction,  $y_\alpha$ , can be defined as

$$Q_\alpha(\eta, x_i, t) = \frac{\langle \rho Y_\alpha(x_i, t) \mid \xi(x_i, t) = \eta \rangle}{\rho_\eta}, \quad (3.1)$$

where  $\xi$  is the mixture fraction,  $\eta$  is the sample space variable upon which the mixture fraction is conditioned, such that  $0 \leq \eta \leq 1$ , and  $\rho_\eta = \langle \rho \mid \eta \rangle$  is the conditional density. The notation  $\langle \rangle$ , denotes the ensemble average, where the quantity on the left of the vertical bar is conditioned on the quantity to the right. Using decomposition, the mass fraction of  $\alpha$ ,  $Y_\alpha$  can be shown as

$$Y_\alpha(x_i, t) = Q_\alpha(\xi(x_i, t), x_i, t) + y''_\alpha(x_i, t), \quad (3.2)$$

where  $y''$  is a fluctuation with respect to the conditional mean. By definition of first order CMC,  $y''_\alpha(x_i, t) = 0$ .

As a starting point, the species transport equation is combined with the definition of the conditional average mass fraction, such that

$$\frac{\partial(\rho Y_\alpha)}{\partial t} + \frac{\partial(\rho u_i Y_\alpha)}{\partial x_i} = \frac{\partial}{\partial x_i} \left( \rho D_\alpha \frac{\partial Y_\alpha}{\partial x_i} \right) + \dot{\omega}. \quad (3.3)$$

It has been assumed that with high Re flows, the species diffusivities are dominated by turbulent mixing and remain constant across all species, such that  $D_\alpha = D$ . Subsequent substitution of Eq. 3.2 into 3.3 followed by conditional averaging over  $\eta$  yields

$$\langle \rho | \eta \rangle \frac{\partial(Q_\alpha)}{\partial t} + \langle \rho | \eta \rangle \langle u_i | \eta \rangle \frac{\partial(Q_\alpha)}{\partial x_i} = \langle \rho | \eta \rangle \frac{\langle \chi | \eta \rangle}{2} \frac{\partial^2 Q_\alpha}{\partial \eta^2} + e_Q + e_Y + \langle \dot{\omega} | \eta \rangle, \quad (3.4)$$

where

$$\langle \chi | \eta \rangle = 2D \frac{\partial^2 Q_\alpha}{\partial \eta^2}, \quad (3.5)$$

is the conditional scalar dissipation rate. Two additional terms requiring closure are  $e_Q$  and  $e_Y$ . Following [13],  $e_Q$  and  $e_Y$  are defined as

$$e_Q = \left\langle \left[ \frac{\partial}{\partial x_i} \left( \rho D \frac{\partial Q_\alpha}{\partial x_i} \right) + \rho D \frac{\partial \xi}{\partial x_i} \cdot \frac{\partial}{\partial x_i} \left( \frac{\partial Q_\alpha}{\partial \eta} \right) \right] | \eta \right\rangle, \quad (3.6)$$

and

$$e_Y = - \left\langle \left[ \rho \frac{\partial y''_\alpha}{\partial t} + \rho u_i \frac{\partial y''_\alpha}{\partial x_i} - \frac{\partial}{\partial x_i} \left( \rho D \frac{\partial y''_\alpha}{\partial x_i} \right) \right] | \eta \right\rangle. \quad (3.7)$$

Analysis by Klimenko and Bilger [13] indicates that the term  $e_Q$  in Eq. 3.6 is small when Re is large. As a result, this term can be neglected,

$$e_Q \approx 0. \quad (3.8)$$

In order to simplify Eq. 3.7, the unconditional form is considered. By analysis of the derivatives of the unconditional average, Bilger [13, 21] shows that the first and third term are negligible, and that  $e_Y$  can be written as

$$e_Y = - \frac{1}{P(\eta)} \frac{\partial}{\partial x_i} (\langle \rho | \eta \rangle \langle u_i'' y'' | \eta \rangle P(\eta)). \quad (3.9)$$

By substituting the definition of the Favre-averaged PDF,  $\tilde{P}(\eta)$  written as

$$\tilde{P}(\eta) = \frac{\langle \rho | \eta \rangle P(\eta)}{\langle \rho \rangle}, \quad (3.10)$$

where  $\langle \rho \rangle$  is the unconditional density, Eq. 3.4 becomes

$$\begin{aligned} \frac{\partial(Q_\alpha)}{\partial t} + \langle u_i | \eta \rangle \frac{\partial(Q_\alpha)}{\partial x_i} &= \frac{1}{\langle \rho \rangle \tilde{P}(\eta)} \frac{\partial}{\partial x_i} \left( \langle \rho \rangle \langle u_i'' y_\alpha'' | \eta \rangle \tilde{P}(\eta) \right) \\ &+ \frac{1}{2} \langle \chi | \eta \rangle \frac{\partial^2 Q_\alpha}{\partial \eta^2} + \frac{\langle \dot{\omega} | \eta \rangle}{\langle \rho | \eta \rangle}. \end{aligned} \quad (3.11)$$

The first term on the LHS of Eq. 3.11 represents the temporal rate of change of the conditional species mass fraction, while the second term represents the conditional transport by convection. The first term on the RHS of Eq. 3.11 accounts for the transport due to turbulent flux, the second term represents the molecular mixing and the third term is the chemical source term. Use of Eq. 3.11 forms the basis of the Conditional Moment Closure model.

### 3.3 Conditional Enthalpy and Temperature Equation

The enthalpy,  $h$ , of a mixture of species is the summation of the enthalpy of each of its constituents. The enthalpy of each constituent can be seen as a function of the mass fraction  $Y_\alpha$ , temperature,  $T$ , such that

$$h = h(Y_1, \dots, Y_n, T) = \sum_{\alpha=1}^n Y_\alpha \left( (h_0)_\alpha + \int_{T_0}^T (C_p)_\alpha dT \right). \quad (3.12)$$

This definition can be extended to conditional form, such that

$$Q_h = \sum_{\alpha=1}^n Y_\alpha \langle h(x_i, t) \eta \rangle Q_\alpha. \quad (3.13)$$

Subsequently, the conditional temperature,  $Q_T$ , may be derived from the mixture enthalpy equation where

$$h = a_0 + a_1 T + a_2 T^2. \quad (3.14)$$

The enthalpy coefficients  $a_0$ ,  $a_1$ , and  $a_2$  are calculated by summing the coefficient values for the Favre-averaged species mass fractions.

The transport equation for the conditional average enthalpy,  $Q_h = \langle h | \eta \rangle$ , may be derived from the enthalpy transport,

$$\frac{\partial(\rho h)}{\partial t} + \frac{\partial(\rho u_i h)}{\partial x_i} = \frac{\partial}{\partial x_i} \left( \rho D_\alpha \frac{\partial h}{\partial x_i} \right) + \frac{\partial p}{\partial x_i} + \dot{q}_{rad}, \quad (3.15)$$

in a similar fashion as shown in the preceding section. The conditional enthalpy is defined as

$$Q_h(\eta, x_i, t) = \langle h(x_i, t) | \xi(x_i, t) = \eta \rangle. \quad (3.16)$$

The conditional enthalpy may be subsequently decomposed into

$$h(x_i, t) = Q_h(\xi(x_i, t), x_i, t) + h''(x_i, t), \quad (3.17)$$

where, by definition,  $\langle h''(x_i, ) | \eta \rangle = 0$ . Substitution of the conditional enthalpy into Eq. 3.15 followed by conditional averaging on  $\eta$  yields

$$\begin{aligned} \frac{\partial Q_h}{\partial t} + \langle u_i | \eta \rangle \frac{\partial Q_h}{\partial x_i} = & -\frac{1}{\langle \rho \rangle \tilde{P}(\eta)} \frac{\partial}{\partial x_i} \left( \langle \rho \rangle \langle u_i'' h'' | \eta \rangle \tilde{P}(\eta) \right) + \frac{1}{2} \langle \chi | \eta \rangle \frac{\partial^2 Q_h}{\partial \eta^2} \\ & + \frac{1}{\langle \rho | \eta \rangle} \left\langle \frac{\partial p}{\partial t} | \eta \right\rangle - \frac{\langle \dot{q}_{rad} | \eta \rangle}{\langle \rho | \eta \rangle}. \end{aligned} \quad (3.18)$$

The two terms on the LHS of Eq. 3.18 represent the temporal rate of change of conditional enthalpy, and the conditional convective enthalpy transport, respectively. On the RHS of this equation, the first term represents the enthalpy transport by turbulent flux, the second term represents enthalpy dissipation, which is largely influenced by the local molecular mixing rate, the third term is the pressure work term and the final term is the heat loss due to radiation. The radiation losses are highly dependent on the products of the fuel, where fuels producing large amounts of soot such as diesel may have extremely high heat losses. Fuels such as hydrogen, which do not produce soot, have significantly less radiative heat loss. The gaseous combustion byproducts, such as  $H_2O$ , are the primary emitters for  $H_2$ .

## 3.4 Terms Requiring Closure

In the Section 3.3, several terms are introduced that require closure in order to evaluate the transport equations. This section outlines the models used to close the remaining terms. These terms include the conditional chemical source term,  $\langle \dot{\omega}_\alpha | \eta \rangle$ , the turbulent fluxes,  $\langle u_i'' y_\alpha'' | \eta \rangle$  and  $\langle u_i'' T_\alpha'' | \eta \rangle$ , the conditional velocity,  $\langle u_i | \eta \rangle$ , and the PDF,  $\tilde{P}(\eta)$ . The final unclosed term is that of the conditional scalar dissipation rate,  $\langle \chi | \eta \rangle$ , and is presented in full detail in Section 3.5.

### 3.4.1 Conditional Chemical Source Term

Production and evolution of chemical species is very dependent on the mechanism used. Also, due to the nature of chemical kinetics, the highly non-linear reaction rates are very sensitive to temperature. In general, a reversible reaction step may be represented as two irreversible reactions, which are in equilibrium when the forward and reverse rates are equivalent. Each of these irreversible reactions can be described by the reaction



Despite the simplicity of this equation, it can be applied to any fundamental step in a reaction mechanism. The rate of formation of products has previously been referenced as the chemical source term,  $\dot{\omega}$ . Progress rate of the reaction is typically controlled by a reaction rate calculation, where

$$\dot{\omega} = \rho k(T) Y_A Y_B. \quad (3.20)$$

In this equation,  $Y_A$  and  $Y_B$  represent the mass fractions of the reactants,  $\rho$  is the average density, and  $k(T)$  is the temperature dependent reaction rate constant. The rate constant is a simple, yet highly accurate description of the resultant rate of reaction, where

$$k = AT^n \exp\left(\frac{-T_a}{T}\right). \quad (3.21)$$

$A$  is the collision frequency factor,  $n$  is the temperature exponent, and  $T_a$  is the activation temperature. The activation temperature is a description of the average kinetic energy

required to initiate a reaction. When the temperature is below the activation temperature, the reaction may be assumed to proceed sufficiently slowly that it may be neglected. The temperature is calculated as a function of mixture enthalpy, based on the equations presented in Section 3.3.

As a result of the non-linearity of the chemical source term,  $\langle \dot{\omega} \rangle$  cannot be expressed as a linear function of the unconditional averages  $\langle \rho \rangle$ ,  $\langle T \rangle$ , and  $\langle Y \rangle$ , i.e.

$$\langle \dot{\omega}_\alpha(Y, T) \rangle \neq \dot{\omega}_\alpha(\langle Y \rangle, \langle T \rangle), \quad (3.22)$$

which is due to the fluctuations in  $Y$  and  $h$  [13]. Therefore, when considering the effects of fluctuations, the equation becomes

$$\langle \dot{\omega}_\alpha(Y, T) \rangle \neq \dot{\omega}_\alpha(\langle Y \rangle, \langle T \rangle). \quad (3.23)$$

The magnitude of the conditional fluctuations are known to be considerably smaller than the unconditional fluctuations [13], such that

$$\begin{aligned} y'' &\ll y', \\ T'' &\ll T'. \end{aligned} \quad (3.24)$$

As a result, the average of the chemical source term may be conditioned on the mixture fraction, yielding the conditional chemical source term equation

$$\langle \dot{\omega}_\alpha(Y, T) | \eta \rangle = \langle \dot{\omega}_\alpha(\langle Y | \eta \rangle + y'', \langle T | \eta \rangle + T'') | \eta \rangle. \quad (3.25)$$

By neglecting the conditional fluctuations due to the first order closure of the chemical source term,

$$\langle \dot{\omega}_\alpha(Y, T) | \eta \rangle \simeq \langle \dot{\omega}_\alpha(\langle Y | \eta \rangle, \langle T | \eta \rangle) | \eta \rangle = \dot{\omega}_\alpha(\langle Y | \eta \rangle, \langle T | \eta \rangle), \quad (3.26)$$

Klimenko and Bilger note that the intensities of the conditional fluctuations are dependent on both the flow and the chemical reactions [13]. It follows that the accuracy of this closure is therefore dependent on the magnitude of conditional fluctuations [13]. By performing a second order Taylor series expansion of Eq. 3.20, it is seen that the equation

$$\begin{aligned} \langle \dot{\omega} | \eta \rangle \simeq \langle \rho | \eta \rangle k(Q_T) Q_A Q_B &\left[ 1 + \frac{\langle y_A'' y_B'' | \eta \rangle}{Q_A Q_B} + \left( \beta + \frac{T_a}{Q_T} \right) \left( \frac{\langle y_A'' T'' | \eta \rangle}{Q_A Q_T} + \frac{\langle y_B'' T'' | \eta \rangle}{Q_B Q_T} \right) \right. \\ &\left. + \frac{1}{2} \left( \beta(\beta - 1) + \frac{2(\beta - 1)T_A}{Q_T} + \frac{T_a^2}{Q_T^2} \right) \frac{\langle (T'')^2 | \eta \rangle}{Q_T^2} \right] \end{aligned} \quad (3.27)$$

can be derived. By assuming that the conditional fluctuations are small, with the exception of the first term, all terms on the RHS of Eq. 3.27 are negligible. By neglecting these terms, this equation is significantly simplified and reduces to

$$\langle \dot{\omega} | \eta \rangle \simeq \langle \rho | \eta \rangle k(Q_T) Q_A Q_B. \quad (3.28)$$

Thus, Eq. 3.28 represents the final form of the first order closure of the conditional chemical source term required for the CMC model.

### 3.4.2 Turbulent Flux

The second group of terms requiring closure in the CMC equations are related to the conditional turbulent transport flux, which can be shown as  $\langle u_i'' \phi'' \rangle$  for the scalar  $\phi$ . Analogous to the approach used for obtaining closure in Eq. 2.47, the Favre-averaged mixture fraction transport equation, closure for the current conditionally averaged terms are obtained by invoking the gradient diffusion hypothesis. The gradient diffusion hypothesis states that the turbulent transport of a conserved scalar,  $\phi$ , is governed by the mean scalar gradient, which occurs in the direction of  $-\nabla \langle \phi \rangle$  [4], such that

$$\langle u_i'' \phi'' \rangle = -D_T \frac{\partial \phi}{\partial x_i} \quad (3.29)$$

where

$$D_T = \frac{\nu_T}{Sc_T} = \frac{C_\mu \tilde{k}^2}{Sc_t \tilde{\epsilon}} \quad (3.30)$$

In these equations,  $D_T$  is the turbulent diffusivity,  $\nu_T$  is the turbulent kinematic viscosity,  $C_\mu = 0.09$  is an empirically derived constant, and  $Sc_T$  is the turbulent Schmidt number. Closure for the conditional turbulent flux terms,  $\langle u_i'' y_\alpha'' | \eta \rangle$  and  $\langle u_i'' T'' | \eta \rangle$ , is obtained by applying this hypothesis as shown in Eq. 3.29. These terms then become

$$\langle u_i'' y_\alpha'' | \eta \rangle = -D_T \frac{\partial \langle y_\alpha | \eta \rangle}{\partial x_i}, \quad (3.31)$$

and

$$\langle u_i'' T'' | \eta \rangle = -D_T \frac{\partial \langle T | \eta \rangle}{\partial x_i}. \quad (3.32)$$

### 3.4.3 Conditional Velocity

Closure of the conditional velocity term is based on the linear model, initially proposed by Kuznetsov et al. [22] and applied to CMC [10, 11]. This model assumes a linear progression of the conditional velocity in the sample space, such that

$$\langle \tilde{u}_i | \eta \rangle = \tilde{u}_i + \frac{\widetilde{u_i'' \xi''}}{\xi''^2} (\eta - \tilde{\xi}). \quad (3.33)$$

As seen in Sec. 3.4.2, the gradient diffusion hypothesis is again used to obtain closure for the turbulent flux term,  $\widetilde{u_i'' \xi''}$ , such that the conditional velocity becomes

$$\langle \tilde{u}_i | \eta \rangle = \tilde{u}_i - D_T \frac{(\eta - \tilde{\xi})}{\xi''^2} \frac{\partial \tilde{\xi}}{\partial x_i}. \quad (3.34)$$

In Eq. 3.34,  $\tilde{u}_i$  is the Favre-averaged velocity,  $\tilde{\xi}$  is the Favre-averaged mixture fraction,  $\xi''^2$  is the Favre-averaged mean mixture fraction variance and  $D_T$  is the turbulent diffusivity.

The linear conditional velocity model is supported by various experimental data [22, 23] and is considered to be a good approximation for flows where  $\eta$  is within two standard deviations of  $\tilde{\xi}$ . Despite this, measurements performed by Li et al. raise some question as to the accuracy and validity of this model [24].

Notwithstanding the potential flaws in the model, the linear conditional velocity model remains popular due to its ease of implementation, low computational expense and numerical robustness. The linear conditional velocity model is used for the remainder of this study.

### 3.4.4 Probability Density Function

One of the most important unclosed terms in the CMC equation is the probability density function. Although briefly discussed in Sec. 2.4, presumed probability density functions require a large amount of computational cost and forethought for proper implementation. The unclosed term appears in several locations within the CMC model: in the conditional species mass fraction equations, the conditional temperature equation and the conditional scalar dissipation rate equation. Due to its widespread implementation, the presumed form PDF *must* provide a physically valid and accurate description of the flow. Without proper modelling of the PDF, the CMC model is unlikely to provide accurate results.

Defining the PDF is accomplished by using one of a number of presumed form PDFs. Although there are many potential distributions that could be applied to a given problem, the two most commonly found are the clipped Gaussian PDF and the  $\beta$ -PDF. Each of these requires a mean and variance for the flow to be provided for calculation of the appropriate probability distribution.

### Clipped Gaussian PDF

The clipped Gaussian PDF is a modification of the Gaussian, or normal distribution. The normal distribution is a perfectly symmetrical PDF, centered on the mean, with the strength of the tails governed by the variance. The tails of the normal distribution extend to infinity, but assume very low values at the furthest extents. By definition, the integration of

$$\int_{-\infty}^{+\infty} P(\eta)d\eta = 1 \quad (3.35)$$

must be true. Contrary to the implications of Eq. 3.35, the variable  $\eta$  is limited only to  $0 \leq \eta \leq 1$  in the current application. Therefore, the integration of this PDF across  $\eta$ -space is no longer true, i.e.

$$\int_0^1 P(\eta)d\eta \neq 1. \quad (3.36)$$

Due to this limitation, further modification is required to the PDF such that the LHS of Eq. 3.36 evaluates to be equal to 1. The clipped Gaussian form of the PDF is a modification that provides proper closure.

In order to account for the discrepancy, the strength of the tails is accounted for by providing a modification to the magnitude of the PDF. In order to achieve the proper moments upon integration, for the range of  $0 < \eta < 1$  the PDF now takes the form

$$P_T = \frac{G(\eta)}{\int_0^1 G(\eta)d\eta}, \quad (3.37)$$

in which  $G(\eta)$  follows the normal distribution, i.e.

$$G(\eta) = \frac{1}{\sigma_g\sqrt{2\pi}}\exp\left(-\frac{(\eta - \xi_g)^2}{2\sigma_g^2}\right). \quad (3.38)$$

The distribution of  $P_T$  is valid for mixed fluid, i.e.  $\eta \neq 0$  and  $\eta \neq 1$ , in which  $\xi_g$  and  $\sigma_g$  represent the mean and variance, respectively. Although Eq. 3.38 provides proper closure upon integration between 0 and 1, it does not provide a representation of unmixed fluid. This is accomplished via the use of Dirac delta functions,  $\delta(\eta)$ , placed at the two limits, representing pure fuel and pure oxidiser. The delta functions evaluate to 1 when the argument is equal to 0, and 1 everywhere else. The strength of these two delta functions,  $\alpha_1$  and  $\alpha_2$ , is governed by the intermittency of the flow, or the likelihood that unmixed fluid parcels will be present in a given location. These functions become strongest near the fuel inlet and far downstream, but are otherwise relatively small. When combined with  $P_T$ , the equation for the PDF now becomes

$$P(\eta) = \alpha_1\delta(\eta) + (1 - \alpha_1 - \alpha_2)P_T(\eta) + \alpha_2\delta(1 - \eta). \quad (3.39)$$

In this formulation, the strength of the delta functions is related to the area under the tail that is clipped from the PDF. Further information on the formulation of this PDF can be found in [25].

The clipped Gaussian PDF has the distinct advantage of being easy and computationally inexpensive to implement; however, discontinuities at the limits of  $\eta$ -space can potentially lead to some unphysical behaviour.

### **$\beta$ -PDF**

The  $\beta$ -PDF is one of the most commonly used presumed form PDFs in CMC modelling. Girimaji [26] showed that the  $\beta$  form PDF characterises the evolution of  $\tilde{P}(\eta)$  accurately, a finding which is supported by the DNS results of Givi et al. [27], Eswaran et al. [28] and Swaminathan et al. [29]. It has been included in a wide range of studies and flow types [10, 11, 30, 31, 32, 33, 34, 35, 36].

The Favre-averaged  $\beta$ -PDF is given by the expression

$$\tilde{P}(\eta) = \frac{\eta^{\alpha-1}(1-\eta)^{\beta-1}}{I_b} \quad \text{with} \quad I_b = \int_0^1 \eta^{\alpha-1}(1-\eta)^{\beta-1} d\eta. \quad (3.40)$$

The distribution, shown as a function of  $\eta$ , is characterised by the two parameters  $\alpha$  and  $\beta$ . These parameters are calculated directly from the flowfield using the mean mixture

fraction,  $\tilde{\xi}$  and the mean mixture fraction variance,  $\widetilde{\xi''^2}$ , using the definitions

$$\alpha = \tilde{\xi} \left( \frac{\tilde{\xi}(1 - \tilde{\xi})}{\widetilde{\xi''^2}} - 1 \right), \quad (3.41)$$

and

$$\beta = (1 - \tilde{\xi}) \left( \frac{\tilde{\xi}(1 - \tilde{\xi})}{\widetilde{\xi''^2}} - 1 \right). \quad (3.42)$$

The result of Eq. 3.40, Eq. 3.41 and Eq. 3.42 is a smooth PDF, which provides asymptotic behaviour near the limits of  $\eta = 0$  and  $\eta = 1$  instead of using discontinuous delta functions as in the clipped Gaussian PDF. The  $\beta$ -PDF provides an improvement in the representation of the PDF scalar over the range of valid  $\eta$  values, but at an increased computational cost when compared to the clipped Gaussian PDF.

## 3.5 Conditional Scalar Dissipation Rate

Proper modelling of the conditional scalar dissipation rate,  $\langle \chi \mid \eta \rangle$ , is the primary focus of this study. Many different models with differing assumptions have been suggested for providing closure for this term, ranging from constant values for all  $\eta$ , the assumption of homogeneous turbulence [37, 2] and the assumption of inhomogeneous turbulence [3]. All models have individual strengths and weaknesses, most of which will be summarised in the following section.

### 3.5.1 Mixing Models based on Homogeneous Turbulence

#### Girimaji's Model

Girimaji's mixing model is formulated on the observation that the presumed  $\beta$ -PDF may be used to accurately characterise the scalar PDF during all stages of two-scalar, constant density mixing under statistically stationary, homogeneous turbulence [37]. The model is derived using the homogeneous PDF transport equation as a starting point. This equation

is integrated twice in  $\eta$ -space, such that an expression may be obtained for the conditional scalar dissipation rate, yielding

$$\langle \chi | \eta \rangle = -2\chi \frac{\tilde{\xi}(1 - \tilde{\xi})}{\tilde{\xi}''^2} \frac{J(\eta)}{\tilde{P}(\eta)}. \quad (3.43)$$

In Eq. 3.43,  $\tilde{\chi}$  is the Favre-averaged, unconditional mean scalar dissipation rate, given previously by Eq. 2.53. The function  $J(\eta)$  represents the integral

$$J(\eta) = \int_0^\eta \left\{ \tilde{\xi}(\ln \eta' - J_1) + (1 - \tilde{\xi}) [\ln(1 - \eta') - J_2] \right\} \tilde{P}(\eta') (\eta - \eta') d\eta', \quad (3.44)$$

where

$$J_1 = \int_0^1 \ln \eta d\eta, \quad \text{and} \quad J_2 = \int_0^1 \ln(1 - \eta) d\eta. \quad (3.45)$$

The derivation of this model is based entirely upon the assumption of statistically stationary, homogeneous turbulence, similar to grid generated turbulence. Therefore, Girimaji's model should not be applied in shear layers and similar flows as well as flows with highly inhomogeneous turbulence.

## Amplitude Mapping Closure

The Amplitude Mapping Closure model (AMC) is a mixing model that was initially developed by O'Brien [2]. This model assumes that the conditional scalar dissipation rate,  $\langle \chi | \eta \rangle$ , is always proportional to a function,  $G(\eta)$ , that is independent of the mean mixture fraction  $\tilde{\xi}$ , and the mean mixture fraction variance,  $\tilde{\xi}''^2$ , such that

$$\langle \chi | \eta \rangle = \langle \chi | \xi = 0.5 \rangle G(\eta). \quad (3.46)$$

The function  $G(\eta)$  is given by

$$G(\eta) = \exp \left\{ -2 \left[ \text{erf}^{-1}(2\eta - 1)^2 \right] \right\}, \quad (3.47)$$

where  $\text{erf}^{-1}$  is the inverse error function. The error function  $\text{erf}^{-1}(2\eta - 1)^2$  is singular at  $\eta = 0$  and  $\eta = 1$ , where  $\lim_{x \rightarrow -1} \text{erf}^{-1}(x) = -\infty$  and  $\lim_{x \rightarrow 1} \text{erf}^{-1}(x) = \infty$ . These singularities are avoided in Eq. 3.47 by use of the exponential function, resulting in

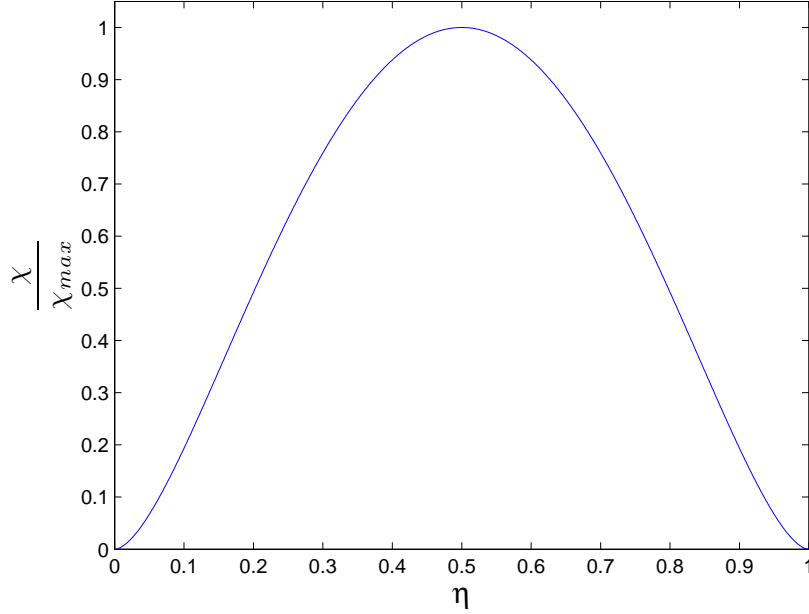


Figure 3.1: AMC model  $G(\eta)$  distribution

$G(0) = G(1) = 0$ . This curve is symmetrical about its maximum at  $\eta = 0.5$ , as shown in Fig. 3.1.

In order to obtain proper closure with the value of  $\langle \chi \mid \xi = 0.5 \rangle$ , further modelling assumptions are required. This quantity is obtained by the integration of Eq. 3.46 multiplied by the Favre-averaged PDF,  $\tilde{P}(\eta)$ , from  $0 \leq \eta \leq 1$  such that

$$\langle \chi \mid \eta \rangle = \frac{\int_0^1 \langle \chi \mid \eta \rangle \tilde{P}(\eta) d\eta}{\int_0^1 G(\eta) \tilde{P}(\eta) d\eta} = \frac{\tilde{\chi}}{\int_0^1 G(\eta) \tilde{P}(\eta) d\eta}, \quad (3.48)$$

where  $\tilde{\chi}$  is the Favre-averaged mean scalar dissipation rate, given previously in Eq. 2.53.

### 3.5.2 Models Based on Inhomogeneous Turbulence

Quite often, the assumption of homogeneous turbulence is not valid, thus negating the basic assumptions made in Girimaji's model and the AMC model. In order to provide a more generally applicable scalar dissipation rate model, Devaud et al. [3] developed a model on the basic assumption of inhomogeneous turbulence. Due to the assumptions

made during formulation, this model is appropriate to flows such as autoignition occurring at low temperatures, where more complete mixing of the fuel is required before ignition occurs. This model was formulated directly from the probability density function of the conserved scalar mixture fraction,  $\tilde{\xi}$ .

The first step in derivation of this model is the double integration of the PDF transport equation, shown in its original form as

$$\frac{\partial \langle \rho \rangle \tilde{P}(\eta)}{\partial t} + \frac{\partial}{\partial x_i} \left( \langle \rho \rangle \langle u_i | \eta \rangle \tilde{P}(\eta) \right) = \frac{\partial^2}{\partial \eta^2} \left( \frac{1}{2} \langle \rho \rangle \tilde{P}(\eta) \langle \chi | \eta \rangle \right), \quad (3.49)$$

where once again, the term  $\langle u_i | \eta \rangle$  is the conditional velocity. In order to provide closure for the conditional velocity term, the linear conditional velocity model, shown previously in Eq. 3.34, is introduced. Following the double integration of Eq. 3.49, the general form of the inhomogeneous model is obtained, yielding

$$\frac{1}{2} \tilde{P}(\eta) \langle \chi | \eta \rangle = -\frac{1}{\langle \rho \rangle} \left( \frac{\partial \langle \rho \rangle \tilde{I}_1(\eta)}{\partial t} \right) + \frac{-1}{\langle \rho \rangle} \frac{\partial}{\partial x_i} \left( \langle \rho \rangle \tilde{u}_i \tilde{I}_1(\eta) \right) + \frac{-1}{\langle \rho \rangle} \left( \langle \rho \rangle \frac{\widetilde{u_i'' \xi''}}{\widetilde{\xi''^2}} \tilde{I}_2(\eta) \right). \quad (3.50)$$

In this equation,  $I_1$  and  $I_2$  are integral quantities defined as

$$\tilde{I}_n(\eta) = \int_{\eta}^1 (\eta^0 - \eta) (\eta^0 - \tilde{\xi})^{n-1} \tilde{P}(\eta^0) d\eta^0, \quad (3.51)$$

where  $n = 1$  or  $n = 2$ . The boundary conditions for these integrals in  $\eta$ -space are [3]

$$\begin{aligned} \tilde{I}_1(0) &= \tilde{\xi}, & \tilde{I}_1(1) &= 0, \\ \tilde{I}_2(0) &= \widetilde{\xi''^2}, & \tilde{I}_2(1) &= 0. \end{aligned} \quad (3.52)$$

In the range of  $0 \leq \eta \leq 1$ , these functions are monotonic with respect to  $\eta$  [3].

Further simplification of Eq. 3.49 is achieved through the use of the gradient diffusion hypothesis to replace  $\widetilde{u_i'' \xi''}$  with the substitution

$$\widetilde{u_i'' \xi''} = -D_T \nabla \tilde{\xi}. \quad (3.53)$$

Following simplification, Eq. 3.50 becomes

$$\frac{1}{2} \tilde{P}(\eta) \langle \chi | \eta \rangle = -\frac{1}{\langle \rho \rangle} \left( \frac{\partial \langle \rho \rangle \tilde{I}_1(\eta)}{\partial t} \right) + \frac{-1}{\langle \rho \rangle} \frac{\partial}{\partial x_i} \left[ -\langle \rho \rangle \tilde{u}_i \tilde{I}_1(\eta) + \frac{\langle \rho \rangle D_T \tilde{I}_2(\eta)}{\widetilde{\xi''^2}} \frac{\partial \tilde{\xi}}{\partial x_i} \right]. \quad (3.54)$$

Rearranging Eq. 3.54 and applying the continuity and transport equations of  $\tilde{\xi}$  yields

$$\frac{1}{2}\tilde{P}(\eta)\langle\chi|\eta\rangle = \underbrace{-\frac{\partial}{\partial t}\tilde{I}_1(\eta)}_{\text{Term 1}} + \underbrace{\left[-\tilde{u}_i\frac{\partial\tilde{I}_1(\eta)}{\partial x_i}\right]}_{\text{Term 2}} + \underbrace{\left[-D_t\frac{\partial\tilde{\xi}}{\partial x_i}\frac{\partial}{\partial x_i}\left(\frac{\tilde{I}_2(\eta)}{\tilde{\xi}''^2}\right)\right]}_{\text{Term 3}} + \underbrace{\left(\frac{\tilde{I}_2(\eta)}{\tilde{\xi}''^2}\right)\left[\frac{\partial\tilde{\xi}}{\partial t} + \tilde{u}_i\frac{\partial\tilde{\xi}}{\partial x_i}\right]}_{\text{Term 4}}, \quad (3.55)$$

which is in a form that is suitable for discretisation in the CMC code.

Devaud et al. compared the performance of this model based to Girimaji's model and DNS results [38] at various positions and found an improvement in predictions. Previous studies have also used this model with success [11, 39].

## 3.6 Summary

This chapter presented an overview of the first-order Conditional Moment Closure Model. Use of the CMC model allows for simulation of combustion with a wide range of chemical timescales that cannot be accurately modelled using the EBU or laminar flamelet model.

The general form of the species transport equation including all unclosed terms was presented. Common models for closure of the chemical source term, turbulent flux and conditional velocity were presented. Two different models for closing the conditional probability density function were discussed, including the clipped Gaussian PDF and the  $\beta$ -PDF. Several different models for the conditional scalar dissipation rate, including the inhomogeneous model which is the focus of the current study, were introduced.

The following chapter introduces and discusses the steady flame and autoigniting flames used in this work. Also included are results and observations from previous numerical studies of these two flames.

# Chapter 4

## Previous Experimental and Numerical Studies

This chapter provides a summary of the two experimental and related numerical studies used in the current work. The first experimental flame, which consists of a steady  $H_2$  jet in a quiescent unconfined environment, provides a validation case for the current code. In studying the performance of the CMC calculations in relation to the experimental results, a baseline of calculation performance is obtained. The findings are applied to the second case, which is the simulation of a transient autoigniting flame. In this case, a mixture of  $H_2$  and  $N_2$  is injected into a turbulent coflow of air. As the fuel and oxidiser mix, chemical interaction occurs resulting in autoignition of the mixture. The available numerical work relating to this flame, including studies of chemical mechanisms and full simulations of the autoigniting flow using various modelling techniques are also covered.

### 4.1 Steady Flame

The flame chosen to validate the CMC calculations for the first part of the current work is that studied by Barlow and Carter [40]. This flame consists of a high velocity hydrogen jet in an essentially quiescent environment. Although the focus of the Barlow and Carter study is to evaluate nitric oxide formation, detailed temperature and mixture frac-

tion results are presented, in conjunction with conditional species mass fractions for the OH radical. RANS simulations by Barlow et al. provide details about the nitric oxide predictions yielded by the CMC and PDF combustion models when combined with various radiation submodels [41].

### 4.1.1 Experimental Method

In the experimental study [40], a variety of different mixtures of  $H_2$  and  $He$  for fuel at various Reynolds numbers were tested. The most complete data are presented for the case of 100%  $H_2$  at a Reynolds number of 10000, so this case is chosen as the baseline for comparison.

The experimental apparatus consists of a single straight tube used as the burner, with an inner diameter,  $d$ , of 3.75mm and an outer diameter of 4.8mm [40]. The burner velocity was maintained such that the outlet  $Re$  is 10000, which corresponds to approximately 296m/s for pure  $H_2$ . The stoichiometric mixture fraction,  $\eta_{st}$ , for this flame is equal to 0.0285. The coflow consisted of pure air maintained at a velocity of approximately 1m/s. The coflow and burner outlet direction are parallel. In all cases, the experimental apparatus maintained an unconfined flame, that is, the coflow existed in a free environment without any external tube or walls to direct, enclose or otherwise influence the flow.  $Re$  above 10000 were not tested, as the flame tended towards liftoff conditions as the fuel velocity increased.

### 4.1.2 Experimental Results

A variety of results for the pure  $H_2$  flame are published, including radial temperature and mixture fraction profiles, measured at  $L/8$ ,  $L/4$ ,  $3L/8$ ,  $L/2$ ,  $5L/8$ ,  $3L/4$  and  $L$ , where  $L$  represents the visible flame length, equivalent to  $180d$ , or 675mm. Conditional OH values were also presented at the  $L/8$ ,  $3L/8$  and  $3L/4$  locations

The results for Favre-averaged temperature, mixture fraction and NO mole fraction are included in Fig. 4.1. In this figure, the jet follows trends typical for a round jet, with gradual mixing and widening of the jet with increasing axial distance from the inlet.

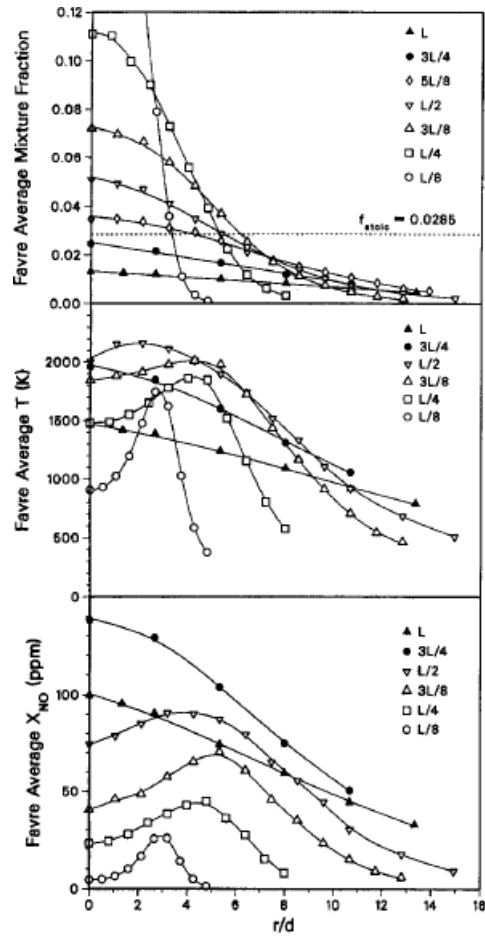


Figure 4.1: Steady mixture fraction, temperature and NO measurements, reproduced from [40]

### 4.1.3 Review of Previous Numerical Simulation

The primary focus of the numerical work by Barlow et al. [41] is the prediction of nitric oxides and the performance of radiation submodels for simulation of the Barlow and Carter flame [40]. The Barlow et al. study, which is conducted using a RANS CFD code, includes detailed results from both the CMC and PDF combustion models. Favre-averaged flowfield results, as well as detailed results for the conditional concentrations of  $O$ ,  $OH$ ,  $H_2O$ ,  $NO$ , and conditional temperature are presented.

Through variation of the  $k - \epsilon$  model constants, excellent agreement with the flowfield is achieved. Centreline predictions of  $\tilde{\xi}$  and  $\tilde{u}$  closely match the measured results. The centreline Favre-averaged temperature results also exhibit excellent agreement with experimental agreement for both the CMC and PDF models, indicating that the chemistry and radiation calculations are performing well. The predictions of  $NO$  are seen to be within 20-30% of experimental measurements.

It is concluded by the authors that there is no clear advantage of using either the CMC or the PDF combustion model in terms of predicting  $NO$  concentrations and radiation. Both models provide good agreement with experimental results for conditional and Favre-averaged values.

## 4.2 Autoigniting Flame

The second part of the present work, relating to the autoignition process, focuses on simulating a single set of experiments, which are performed at ambient pressures with a heated fuel stream and a coflow heated to varying temperatures. The effect of coflow temperature is examined and analysed in relation to how the ignition length is affected. The experimental work performed by Markides and Mastorakos is chosen as the basis for the autoignition portion of this study [42].

### 4.2.1 Experimental Method

In the experiments by Markides and Mastorakos [42], heated air flows are set up with temperatures up to 1015K and velocities up to 35m/s. A fuel, which in the experiment consisted of  $H_2$  gas, either pure or diluted with varying amounts of  $N_2$  gas, is injected along the centreline at various temperatures and velocities. The autoignition of this injected fuel is observed by using high speed photography to capture the chemiluminescence of the hydroxyl,  $OH$ , radical which is a precursor to ignition [42].

During the experimentation, a sufficient number of trials are performed such that a statistical description of the autoignition process could be determined for all temperature and velocity combinations. This includes an estimate of the autoignition length,  $L_{ign}$ , mean and variance. The values of  $L_{ign}$  are presented along with the minimum observed ignition lengths for selected combinations of coflow temperature and velocity.

### 4.2.2 Experimental Method

A schematic of the experimental apparatus, reproduced from [42], is shown in Fig. 4.2. The incoming air is electrically heated by inline heaters. A feedback loop takes the air

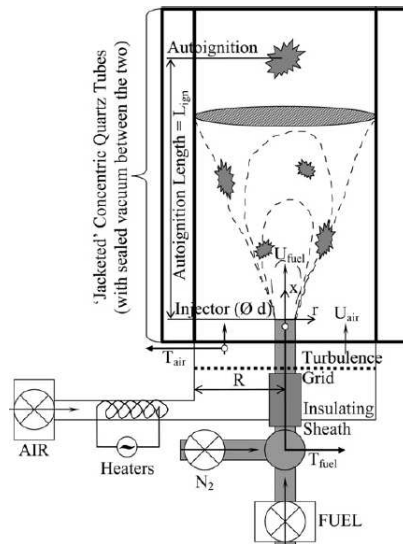


Figure 4.2: Experimental apparatus for autoignition, reproduced from [42]

temperature at the exit of the heater section in order to provide a steady air temperature at the entrance of the test section. Following the heater, the coflow air passed through a perforated plate to provide a uniform level of turbulence throughout the flow. The test section is composed of a vacuum-insulated, jacketed quartz tube. This jacketing allowed optical access to the test section, but also insulated the airflow enough that any heat losses to surroundings are negligible. The quartz test section has an inner diameter of 25.0mm and a total length of 500mm. Air velocities of up to 35m/s are achieved in the test section, with temperatures as high as 1015K [42].

The fuel nozzle consists of a stainless steel tube, with a 2.25mm internal diameter and a 0.32mm wall thickness. The exit of the nozzle is situated 63mm downstream of the perforated plate in order to allow the turbulence to stabilise. The injection of fuel is situated coaxially with the test section such that an axisymmetric flow is obtained. The flow rates for fuel are varied such that the inlet velocity ranged from 20 to 120m/s. Fuel temperatures between 650K and 930K are used.

The fuel and air flows are carefully controlled by digital mass flow controllers in order to maintain the maximum level of consistency between experimental conditions. The air temperatures are measured at several locations along the test section for a non-reacting flow, and it is determined that the temperature does not typically drop more than 3K per 100mm of the test section due to heat loss.

Markides and Mastorakos report that the flow across the test section is essentially uniform in terms of velocity, temperature and turbulence. The turbulence intensity under cold (ambient) conditions is approximately 12-13%, although an estimation for the turbulence intensity during operating conditions is not provided.

Temperature errors are estimated to be approximately 10K, or 1% of the coflow temperature, due to a combination of systematic and random error sources [42].

### 4.2.3 Experimental Results

Although Markides and Mastorakos provide a range of results for different experimental conditions, the main focus of this study will be on a small subsection that involve equal fuel and oxidiser flow velocities, i.e.  $U_{fuel} = U_{air} = 26\text{m/s}$ . The fuel composition is held at a hydrogen mass fraction,  $Y_{H_2}$  of 0.13, with the remainder of the fuel flow being  $N_2$ .

The fuel composition yields a stoichiometric mixture fraction,  $\eta_{st}$  of 0.184. The fuel inlet temperature is maintained at 750K. As a result, only the air coflow temperature remains unspecified, and it is therefore varied over a range of temperatures to capture the autoignition properties. The resulting set of conditions yields what is referred to as being similar to a diffusion problem, since the spreading is largely due to turbulence and diffusion as opposed to advective means [42].

Due to the nature of autoignition, it is difficult to associate an exact time of occurrence to the event. As the igniting fluid parcel begins to react, chemical reactions begin to take place, relatively slowly in comparison to a fully burning condition. This reacting parcel will evolve various species as well as some enthalpy. The difficulty arises when setting a minimum threshold for either species concentrations or temperature increase, both being difficult to measure. The method adopted in this study is to observe the chemiluminescence of the  $OH$  radical, which is recorded using high speed photography. Although chemiluminescence provides a convenient method of observing autoignition experimentally, the threshold of chemiluminescence is difficult to represent numerically. Alternative methods used to signal the autoignition event in numerical studies are discussed further in Section 4.2.4.

The experimentally observed autoignition lengths are provided in Fig. 4.3 [42], which provides the relevant fuel mass fraction of  $Y_{OH} = 0.13$  and velocity of  $U_{fuel} = 26m/s$ . Although only a narrow range of coflow temperatures are provided, it can be seen that there is a sharp increase in autoignition length with decreasing fuel temperatures.

The results of this study indicate that there are 4 specific regimes of autoignition in the flow tested: no ignition, random spots, lifted flame and flashback [42]. The no ignition regime is characterised by a lack of reaction due to insufficient mixture enthalpy or high scalar dissipation rates which preclude reaction. The random spots regime consists of small ignition kernels forming downstream from the injector, but are subsequently convected downstream before the flame is able to propagate to a stable structure. The lifted flame, which is typically seen with higher fuel velocity, consists of a quasi-steady flame forming at some distance from the fuel outlet. The flame structure is maintained at approximately a constant distance due to the balancing of downstream convective and upstream diffusive heat transfer within the flame structure. The final regime is flashback, in which the diffusive heat transfer is sufficient that convection is overcome, and a stable flame becomes attached to the fuel outlet. The boundary between random spots and flash-

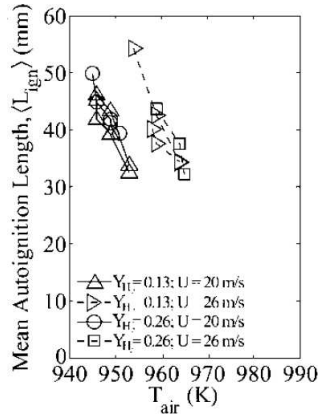


Figure 4.3: Experimental autoignition results, reproduced from Markides and Mastorakos [42]

back is observed to be sharp, typically occurring within 1-2K [42].

#### 4.2.4 Review of Previous Numerical Simulation

Following the experiments by Markides and Mastorakos [42], there have been several numerical works published to simulate the experiment and provide insight into the chemistry and mixing interactions that cannot be directly measured. The studies that have been performed to present cover a variety of numerical investigations, including RANS-CMC [43], LES-PDF [44, 45], LES-CMC [46, 47], DNS [48] and a detailed investigation of autoignition performance of different chemical mechanisms under relevant temperature and scalar dissipation rate conditions with the CMC model [46, 47].

Although the aforementioned studies cover a wide array of methods and details relevant to the experimental results, each is useful as a basis for comparison with the current numerical results. Section 4.2.4 through Sec. 4.2.4 provide a review of the general findings of each study.

## Autoignition Criteria

Before beginning an in-depth review of the results from previous studies, it is important to discuss the criteria for defining autoignition. Although autoignition is referred to as a single event, it is the product of a complex interaction between various species within the chemical mechanism, leading to a chain reaction in which the combustion products are formed and the Favre-averaged temperatures of the flow increase. This process occurs over a finite amount of time, and is not instantaneous.

Experimentally, there are limitations to what can be used for detecting autoignition. Accurate detection of temperature increase can be extremely difficult, due to the short autoignition timescales and thermal inertia of measuring devices. Although it is mentioned that sound can indicate the presence of chemical reaction occurring [42], the chosen method in this study is to measure the presence of the  $OH$  radical through chemiluminescence. The advantage of using chemiluminescence is that it provides a good representation of location, and with the aid of high speed cameras and post processing abilities can provide an accurate measurement of autoignition location and time.

The difficulty arising when analysing numerical results is not with the availability of flow parameters, which for a given flow can be made available to the user at any location and time within the simulation, but rather what is classified as autoignition. If the presence of the  $OH$  radical is used as an indicator, proper criteria must be established to determine a critical concentration or rate of evolution at which autoignition is deemed to have occurred. Similarly, if temperature is used as an indicator, it must be established whether conditional temperature curves or Favre-averaged temperatures are used, and how large the increase must be.

Two different autoignition criteria have been suggested in previous studies involving the  $H_2 - O_2$  reaction mechanism [45, 49]. In [45], the criterion of a temperature increase of 1% is suggested, while in [49], the criterion of the  $OH$  mass fraction reaching a Favre-averaged value of  $2 \times 10^{-4}$  is proposed. Through investigation by Stanković [46], it is determined that for the  $H_2 - O_2$  mechanism under the relevant experimental conditions, the autoignition predictions are insensitive to the criteria used. In the current study, the 1% Favre-averaged temperature increase criterion of Jones et al. [45] is used.

## Chemical Mechanisms

Due to the complexity of the chemical interactions occurring during combustion, for a given fuel composition, there are often multiple detailed mechanisms available for use. Each possible mechanism provides a unique set of sensitivities and characteristics. Although the mechanisms are validated by the authors to some extent [50, 51, 52, 53, 54], the performance of each under various conditions will vary.

Stanković [46] and Stanković et al. [47] have conducted a comprehensive study of the autoignition characteristics of many of the possible hydrogen-oxygen combustion mechanisms. The mechanisms tested include those by Li et al. [50], Yetter et al. [53], Mueller et al. [52], O’Conaire et al. [51] and Konnov [54].

The initial characteristic studied is the effect of the the scalar dissipation rate on autoignition delay. In effect, these simulations replicate a well stirred reactor for each mixture fraction value in  $\eta$ -space. From this calculation, it can be determined how long the minimum expected autoignition delay is for a given coflow temperature, scalar dissipation rate and chemical mechanism.

The method used in the solution of this problem is to reduce Eq. 3.11 to

$$\frac{\partial(Q_\alpha)}{\partial t} = \frac{1}{2}\langle\chi|\eta\rangle\frac{\partial^2 Q_\alpha}{\partial\eta^2} + \frac{\langle\dot{\omega}|\eta\rangle}{\langle\rho|\eta\rangle}, \quad (4.1)$$

which is referred to as the 0-dimensional CMC equation [46]. In Eq. 4.1, the spatial terms are neglected, corresponding to the conditions of a well stirred reactor. This isolates the effects of the scalar dissipation rate and chemical mechanism, allowing for simple and direct comparison between cases. Solution of this equation provides an estimation of the autoignition delay time,  $\tau_{ign}$ , and the most reactive mixture fraction,  $\eta_{mr}$ , where chemical activity peaks in  $\eta$ -space.

It is found that for a coflow temperature of 1030K and a constant  $\chi$  of  $2\text{ s}^{-1}$ , there is a significant difference in the autoignition delay times predicted by the various mechanisms although the predictions of  $\eta_{mr}$  remain fairly consistent for all mechanisms. The value of  $\eta_{mr}$  is seen to vary by approximately 12%, while  $\tau_{ign}$  varies by approximately 27%. The longest delay predicted is for the mechanism by Yetter et al. [53], and the shortest for that by Konnov [54]. The results are summarised in Table 4.2.4.

The effects of scalar dissipation rate on  $\tau_{ign}$  are also studied for a fixed coflow temperature. In this portion of the study, the AMC model is applied for the closure of the

Table 4.1: Autoignition delay with 0-D CMC equation and  $T_{coflow} = 1030\text{K}$ , from [46]

Mechanism	$\tau_{ign}[\text{ms}]$	$\eta_{mr}$
Yetter et al. [53]	0.302	0.0365
Mueller et al. [52]	0.293	0.0365
Li et al. [50]	0.274	0.0409
O’Conaire et al. [51]	0.276	0.0409
Konnov [54]	0.221	0.0409

scalar dissipation rate term in Eq. 4.1. The maximum value of the scalar dissipation rate is given as  $\frac{1}{2}\langle\chi | \eta = 0.5\rangle$ . The results are shown in Fig. 4.4 a) and b) [46]. In Fig. 4.4 a), the coflow temperature is set to 960K. It can be seen that there is a sharp spike in  $\tau_{ign}$  as the value of  $\langle\chi | \eta = 0.5\rangle$  increases, while in Fig. 4.4 b), there is a more gradual increase in  $\tau_{ign}$ . Please note that in Fig. 4.4, the convention  $N$  is used as the conditional scalar dissipation rate, which follows the conversion of  $\langle N | \eta \rangle = \frac{1}{2}\langle\chi | \eta \rangle$ . In general, it is demonstrated that the effect of increasing scalar dissipation rate corresponds to a net increase in the ignition delay time. At lower temperatures, this effect is more pronounced due to the reduced impact of the chemical source term in Eq. 4.1 [46].

An additional finding by Stanković is that the value of  $\eta_{mr}$  increases with increasing

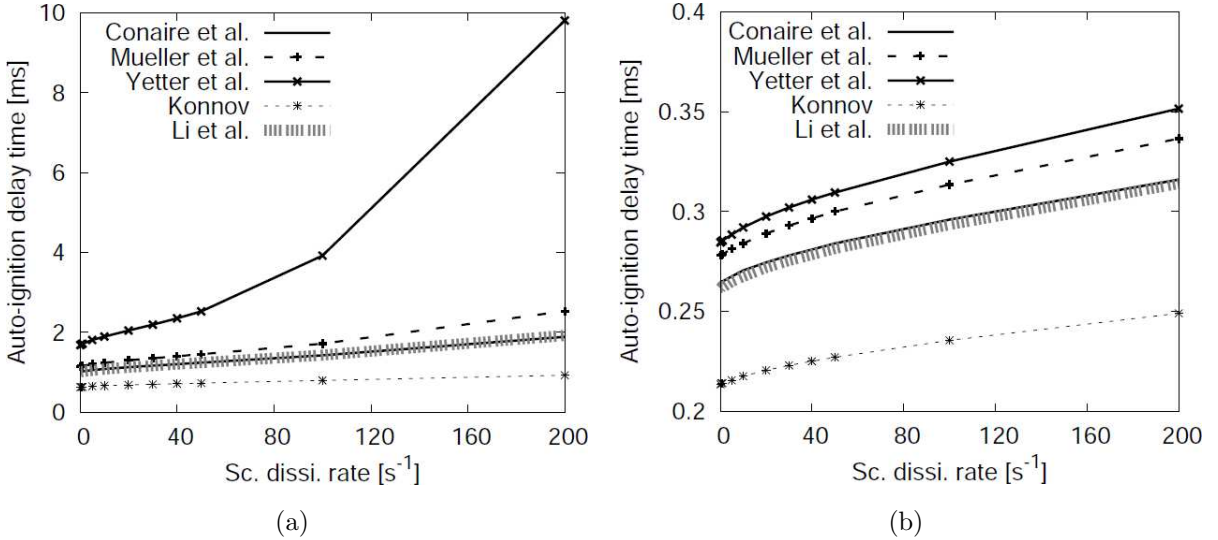


Figure 4.4: Effects on  $\tau_{ign}$  of increasing  $\frac{1}{2}\langle\chi | \eta = 0.5\rangle$ , reproduced from [46]

coflow temperatures. This result is consistently demonstrated through all of the tested

mechanisms [46]. The values of  $\eta_{mr}$  are also seen to become richer as scalar dissipation rate increases. Due to the dilution of the fuel from the low values of  $\eta_{mr}$ , the effects of fuel temperature on autoignition are minimal.

## RANS Simulations

The study performed by Patwardhan and Lakshmisha [43] is, at the time of writing, the only other RANS based CMC study of the Markides and Mastorakos experiment [42]. This study focused on evaluating the autoignition properties for the equal velocity case, where  $U_{fuel} = U_{coflow} = 26m/s$ . The fuel temperature is held constant at 750K, while the coflow is varied between 960K and 1020K. The tuning of the flowfield is also investigated by using a second set of mixing constants, with  $C_{\epsilon_1} = 1.6$ ,  $S_{c_t} = 0.5$ , and  $C_{\chi} = 14$ , from Eq. 2.53. The AMC mixing model is utilised in this study.

Investigation into the mixing field shows a significant change in the predictions for  $\tilde{\xi}$  and  $\tilde{\xi}''^2$  when simulating a steady diffusion flame. The modified constants yield a significant reduction in  $\tilde{\xi}''^2$  near the inlet, and a corresponding increase in the centreline  $\tilde{\xi}$  values. With the code used in [43], this is seen to raise the Favre-averaged centreline temperatures from a significantly underpredicted 1100K to a peak of 2000K for the steady flame [43].

Autoignition length in this study is slightly overpredicted compared to the experimental results. At lower coflow temperatures, the autoignition lengths are seen to follow the trends predicted by the analysis of Stanković [46], with the decreasing coflow temperature yielding a sharp increase in autoignition length.

As this study is performed on a fully coupled CFD-CMC code, some analysis is provided regarding post ignition behaviour. In all cases tested, the numerical results are seen to form an attached diffusion flame. At lower temperatures, i.e. 960K coflow, the flame is observed to travel a significant distance upstream to form a fully detached flame. This is contrary to the experimental findings, which show a very distinct "random spots" regime at  $T_{coflow} = 960K$ , where autoignition kernels are convected downstream before a continued chain reaction is able to form [42]. The cause of this is surmised by the authors to be a result of the averaging nature of RANS simulations, which tend to suppress small flow details such as the random ignition kernels.

## LES Simulations

Several different LES studies of the Markides and Mastorakos experiment have been conducted [42]. The first study published is conducted by Jones et al. [44, 45], and investigates the use of the Lagrangian PDF method, described in Sec. 2.6.3, for autoignition predictions. The second study is that of Stanković [46], in which a fully coupled CMC calculation is incorporated with LES flowfield calculations. Various aspects of autoignition and mixing performance are studied, including autoignition length predictions for different flow conditions.

### LES PDF Method

Jones et al. [45] numerically replicate the burner used in [42]. In total, 6 different cases are studied, with 4 cases having  $U_{fuel} = U_{coflow} = 26m/s$ , which are the primary focus of the current study. The fuel temperature is held at a constant temperature of 750K, while the coflow temperature is varied at 950K, 955K, 960K and 980K [44]. A additional publication of the study includes results from 1000K and 1020K coflows as well [45]. The chemistry mechanism used is that of Yetter et al. [53].

It is found that the LES PDF method provides excellent agreement with experimental results. The autoignition length predictions correspond well with those observed experimentally, as shown in Fig. 4.5. Both the random spots and flashback regimes documented by Markides and Mastorakos [42] are observed, including the sharp boundary between regimes [44]. It is also found that the autoignition length and delay before an anchored flame develops are inversely proportional to coflow temperature, agreeing with the chemistry trends shown by Stanković [46]. The random spots regime is also well represented, with small ignition kernels forming and subsequently being convected downstream before the flame can propagate and anchor. This is repeated continually, with new kernels forming roughly every 2.5ms and then being convected downstream [44]. The no ignition and lifted flame regimes are not observed due to the choice of simulation boundary conditions.

### LES CMC Method

The study performed by Stanković [46] examines the performance of a fully coupled LES-CMC code in relation to the experiments of Markides and Mastorakos [42]. In this study,

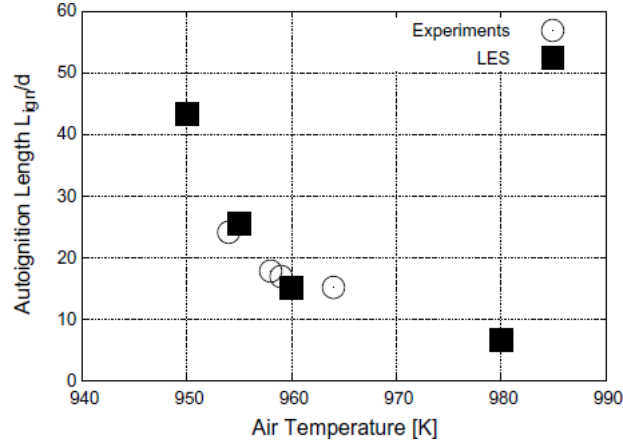


Figure 4.5: LES-PDF autoignition length predictions, reproduced from Jones and Navarro-Martinez [44]

detailed predictions of autoignition lengths and autoignition flow conditions are presented. Again, the geometry of the experimental apparatus is modelled numerically, and several cases with varying velocity and coflow temperature are presented. Fuel inlet velocity ranges from 110-130m/s, with the coflow velocity ranging from 20-35m/s. Fuel temperatures are held constant at 691K, and coflow temperatures of 935K, 945K, 960K, 980K and 1009K are used.

The results published for autoignition length show good agreement with the experimental trends predicted, with a sharp increase in autoignition length seen at lower coflow temperatures. However, in order to obtain good agreement with the length predictions, it is found that the ignition lengths required a 60K shift in the positive direction relative to coflow temperature [46]. This is illustrated in Fig. 4.6, which is shown after the 60K shift is applied. The most consistent performance is achieved using the mechanism of Li et al. [50], which successfully demonstrates the 4 experimental regimes seen by Markides and Mastorakos [42], i.e. no ignition, random spots, lifted flame and flashback. This is achieved through variation of the fuel and coflow temperatures and velocities. In addition to this, detailed results of the conditional values of the different terms in Eq. 3.11 are presented for several locations in the flow.

In this study it is found that CMC model is able to accurately predict the chemical activity seen experimentally, albeit with an underprediction of ignition length. The 4 experimental regimes observed by Markides and Mastorakos [42] are reproduced numerically

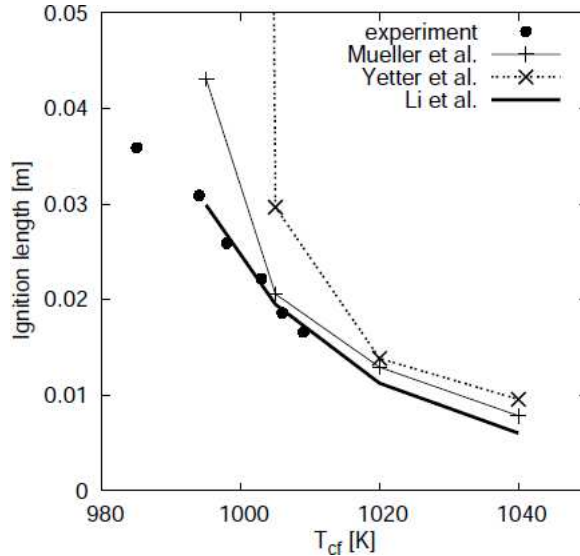


Figure 4.6: LES-CMC autoignition length predictions, reproduced from Stanković [46]

by varying coflow velocity and temperature; however, this performance is dependent on the chemical mechanism used. The transient nature of the random spots regime is observed with small ignition kernels forming and subsequently being convected downstream before flame propagation is able to occur.

## DNS Study

To date, a single DNS study has been reported for the autoignition experiment used in this study [42]. This study, performed by Kerkmeier at ETH in Zurich [48], investigates the performance of a DNS code in both 2-Dimensional and 3-Dimensional autoignition simulations.

In the 2-Dimensional axisymmetric simulations, the entire experimental domain is included in the simulation. In these simulations, all of the experimental regimes observed, no ignition, random spots, flashback and lifted flame, were produced by varying the coflow temperature [48].

In order to minimise computational expense, the 3-Dimensional DNS study is performed on a reduced domain, in which the height and radius of the domain are decreased to the area of interest near the fuel inlet. In the 3-Dimensional simulation, the random

spots regime is simulated, with autoignition kernels forming, then being convected downstream before the flame is able to propagate and form a stable flame structure. Due to the computational requirements, the scope of the 3-Dimensional study is mainly limited to simulation of the flowfield and turbulence characteristics. It is found that the mixture fraction predictions are in good agreement with the distribution predicted by the  $\beta$ -PDF, while the scalar dissipation rate follows a log-normal distribution.

### 4.3 Summary

This chapter presented the previous experimental and numerical work used as a basis for the current work. The first experimental work presented is of a steady state flame, used for initial validation of the numerical code. This study provides detailed results about the flowfield as well as some conditional values used for validation of the CMC calculations. A numerical simulation performed by Barlow et al. on the same flame provides evidence that the CMC model, when properly tuned to the flowfield, can provide excellent correlation with experimental measurements. The second experimental work presented is for an autoigniting flame. This flame, although the flowfield is not well documented, provides an excellent basis for comparison of autoignition predictions. Several detailed numerical studies, including RANS, LES and DNS simulations, are available for comparison. It is seen that there is some difference in ability of the various modelling techniques to predict the various experimental regimes, i.e. no ignition, random spots, lifted flame and flashback. The LES and DNS studies show the ability to successfully predict the random spots regime, while the RANS study is unable to simulate this experimental regime.

The following chapter discusses the numerical implementation of the equations presented in this chapter. The CMC transport equations are discussed with the finite volume (FV) discretisation scheme. Additionally, solver methods and procedures for the non-linear ODE's in the chemical mechanism are presented.

# Chapter 5

## Numerical Implementation of Conditional Moment Closure

Although many of the problems in fluid mechanics can be posed in terms of general ordinary differential equations (ODE) or partial differential equations (PDE), in many cases, solving these equations requires an efficient and accurate numerical implementation. The numerical solution of these ODE's and PDE's forms the basic framework of CFD as well as the basis for additional submodels, such as CMC. Implementation of these submodels has been completed in many academic and commercial CFD codes. A number of different numerical implementation topics will be explored in this chapter, including the general structure of the computational code used in the current work, the present implementation of CMC calculations, the coupling of the CFD and CMC calculations, as well as solver methods and algorithms. Additionally, several strategies to improve the computational efficiency of the calculations are introduced. The effectiveness, ease of use and reliability of each of these efficiency strategies will be discussed.

### 5.1 Code Structure

The first step taken in examining the computational code used in this study is to provide a general outline of the calculation structure. The structure of the code is pivotal in main-

taining accurate and efficient calculations. A flow chart is used to provide an overview of this structure, and each of the following subsections discusses the implementation and effects of various features. The flow chart of this general structure is shown below in Fig. 5.1.

The code begins by reading the input file and initialising variables. All of the boundary conditions, flow parameters and different settings used in the code, including the chemical mechanism, are specified in this input file. Following this, all of the variables required for calculation are either initialised, calculated (if dependent on other variables), or read in from a previously saved file.

The save file feature of the code is extremely useful for initialising or backing up the run. The saved files are output at a user specified interval, typically every 5 or 10 timesteps or as required by the user for processing results, and allow the code to be entirely restarted from that exact point. Using these saved points is also extremely useful in initialising a flowfield prior to turning on the fuel inlet, i.e. allowing the velocity and temperature of a coflow to fully stabilise under given flow conditions prior to adding a fuel mass flow.

The iteration loop, which forms the bulk of the code, begins by storing all variable values in a separate group of arrays for use in time derivative calculations. Only one previous timestep is stored, meaning only first order backwards-differencing methods are used for time derivative calculations. When required, individual variables needed for each species, such as heat capacity,  $c_{p,i}$ , or species enthalpy,  $h_i$ , are combined using a mass weighted sum in order to provide mean values for the flowfield calculations.

The flowfield calculations are carried out in a very typical fashion for unsteady RANS simulations. In this case, the chemical interactions are assumed to be frozen throughout the bulk of the timestep when the CFD calculations are performed, later calculated and updated at the end of each timestep calculation using CMC methods. This allows for a full isolation and control of each of the CFD and CMC portions of the calculation, but retains the interactions required for the calculations to be fully coupled.

The differencing scheme used in the CFD calculations follows the hybrid method developed by Patankar [55]. The hybrid method uses the Peclet number stability criterion to modify the discretisation scheme used, alternating between the Upwind Differencing Scheme (UDS) and the Central Differencing Scheme (CDS). The hybrid method provides the inherent stability of first order UDS, while providing a slight increase in accuracy with the provision of second order CDS where appropriate. Further details on this method and

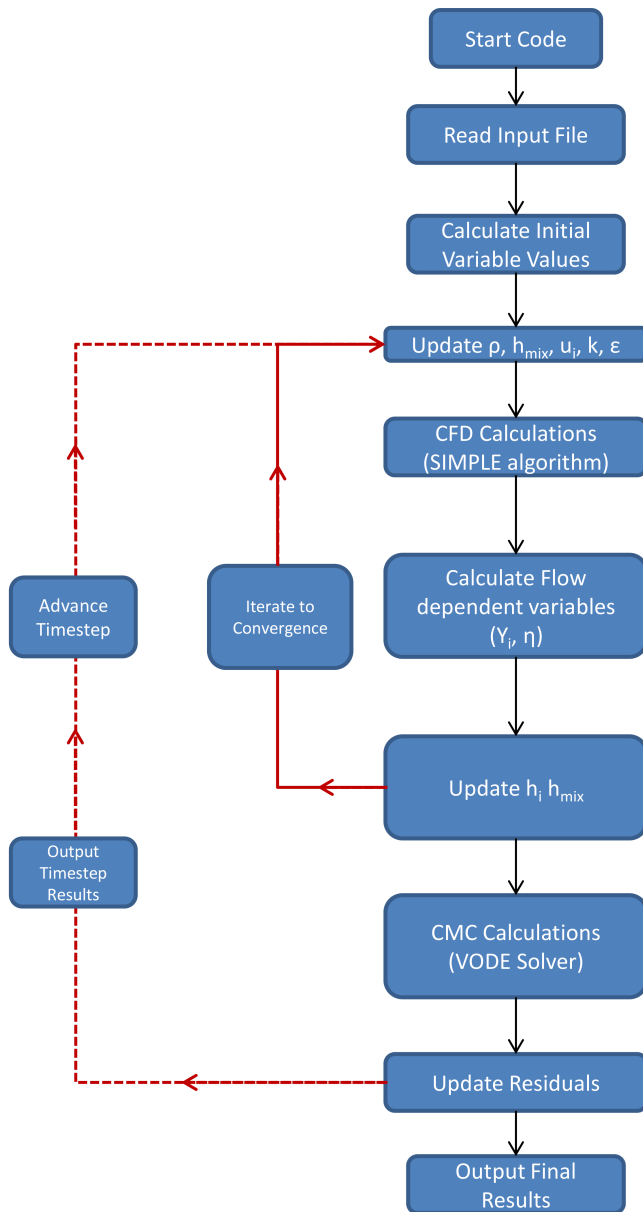


Figure 5.1: Flow chart of code structure

its formulation can be found in [55]. Solution of the linked pressure-velocity equations is accomplished through the use of the SIMPLER algorithm. The SIMPLER algorithm, which stands for Semi-Implicit Method for Pressure Linked Equations - Revised, is a guess and correct iterative method used for solving the coupled pressure and velocity equations, which, for stability reasons are calculated on staggered grids. This method was initially developed by Spalding [56] and further details of its implementation can be found in many CFD texts [6, 55]. This solution methodology is very typical of RANS simulations [6].

The turbulence model used in flowfield calculations follows the standard  $k - \epsilon$  model. This model, which is one of the most common turbulence models used in RANS type simulations, is employed with a standard implementation, as outlined in Sec. 2.3.1. The user may specify the model coefficients used in Eq. 2.30, such as  $C_{\epsilon_1}$  or  $C_{\epsilon_2}$ , in the input file to match the flow to given results.

Following the calculation of the flowfield, which is iterated such that the mass and velocity residuals fall below  $10^{-4}$ , the CMC calculations proceed at the end of the timestep. Due to the nature of the stiff ODE's involved in the chemical mechanism, the computational time required at this stage dominates the total calculation time. The stiff ODE's are solved using a numerical algorithm developed specifically for the problem of solving this type of chemical interaction. This solver, known as the Variable coefficient Ordinary Differential Equation (VODE) [57] solver is used exclusively for the CMC calculations. Further details of this solver, as well as the relevant discretisation methods, will be further discussed in the Sec. 5.2.

### 5.1.1 Coupling of CFD and CMC

Some studies of autoignition using uncoupled CMC calculations have been completed [30, 39, 58]. The advantage to performing uncoupled calculations is that the flowfield and CMC calculations may be performed independently from one another, i.e. the density and chemical changes are small relative to the fluctuations in the flowfield. This allows an extensively validated commercial CFD package to calculate the flowfield, while a standalone code performs the CMC calculations based on the CFD output. The assumption used in the uncoupled method, known as the frozen mixing assumption, becomes invalid at the point of ignition when the temperature, density and changes in chemistry become large and subsequently influence the flowfield. The drawback to this method is that it is only

applicable prior to the onset of ignition and is not suitable for the simulation of flame location and structure.

In order to overcome the frozen mixing assumption, feedback must be provided to the CFD calculations. This is done in the form of mixture enthalpy, which reflects the chemical changes occurring and resultant mixture temperature. Following the completion of every CMC calculation, the conditional temperatures for the constituent species in the mixture are calculated by use of the following relation

$$h = a_0 + a_1T + a_2T^2. \quad (5.1)$$

The resulting conditional temperatures and the conditional enthalpies are Favre-averaged in order to return suitable feedback for the CFD calculations. This change in enthalpy results in a corresponding density and temperature change which effect changes in the flowfield. This iteration method of solving for the flowfield, performing CMC calculations, then advancing the timestep with the new density and enthalpy values is repeated until the desired simulation time is reached.

### 5.1.2 Finite Volume Method

In many previous implementations of CMC, the conditional species transport equation, Eq. 3.4, is shown in non-conservative form using a Finite Difference (FD) discretisation [10, 11, 39, 58]. Although these studies show the finite difference discretisation to be adequate for use, a potential improvement in continuity and conservativeness can be realised by the use of a Finite Volume (FV) discretisation. The use of the FV discretisation allows the conditional species transport equation to be valid through variations of grid spacing, which is an area that the FD assumptions lose validity.

In the present CMC implementation, the conditional species transport equation is discretised on a structured, hexahedral mesh. The directions are designated as  $e$ , east in the positive axial direction,  $w$ , west in the negative axial direction,  $n$ , north in the positive radial direction and  $s$ , south in the negative radial direction. The up and down conventions are not used as this discretisation is used strictly in the 2-D axisymmetric case. The  $p$  subscript denotes values at the centre of the computational cell of interest. Upper case subscripts refer to values at adjacent nodes, while lower case subscripts refer to values

at boundaries, typically velocities, which are required due to the staggered grid. When considering values in mixture fraction, or  $\eta$ -space, the + subscript refers to values at the positive boundary, ++ refers to values at the positive cell centre, - subscripts refer to values at the negative boundary and -- subscripts refer to values at the negative cell centre. This is shown schematically for spatial coordinates in Fig. 5.2.

As an initial step, the conditional species transport equation, Eq. 3.4, must be given

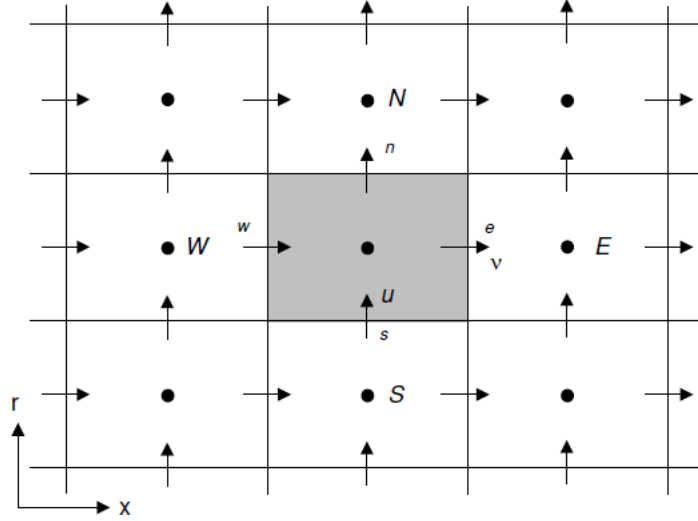


Figure 5.2: Schematic of computational grid, reproduced from [59]

in a form suitable for FV discretisation. That is, the conservative form of the equation must be used as a starting point. Through manipulation of Eq. 3.4, it can be shown that the conservative form of the conditional species transport equation is given by

$$\begin{aligned} \frac{\partial}{\partial x} \left[ \gamma u_{\eta} Q_i - \gamma D_t \frac{\partial Q_i}{\partial x} \right] + \frac{1}{r} \frac{\partial}{\partial r} r \left[ \gamma v_{\eta} Q_i - \gamma D_t \frac{\partial Q_i}{\partial r} \right] = \\ \gamma \langle \omega_i | \eta \rangle + \gamma \frac{1}{2} \langle \chi | \eta \rangle \frac{\partial^2 Q_i}{\partial \eta^2} + Q_i \left[ \frac{\partial}{\partial x} (\gamma u_n) + \frac{1}{r} \frac{\partial}{\partial r} r (\gamma v_{\eta} r) \right]. \end{aligned} \quad (5.2)$$

The substitution  $\gamma = \rho_{\eta} P(\eta) = \langle \rho \rangle \tilde{P}(\eta)$  is used in this equation. This equation is valid for the quasi 2-D axisymmetric case. Planar 2-D or 3-D cases require a different formulation of this transport equation accounting for use of an alternate coordinate system.

The conditional species transport equation is discretised by integrating the advective and diffusive terms across the cell boundaries. By integration of Eq. 5.2 and using Gauss'

Divergence Theorem, Eq. 5.2 becomes

$$\begin{aligned}
& \frac{\gamma_e}{\gamma_P} A_e \left( u_\eta Q_i - Dt \frac{\partial Q_i}{\partial x} \right)_e - \frac{\gamma_w}{\gamma_P} A_w \left( u_\eta Q_i - Dt \frac{\partial Q_i}{\partial x} \right)_w + \\
& \frac{\gamma_n}{\gamma_P} A_n \left( v_\eta Q_i - Dt \frac{\partial Q_i}{\partial r} \right)_n - \frac{\gamma_s}{\gamma_P} A_s \left( v_\eta Q_i - Dt \frac{\partial Q_i}{\partial r} \right)_s - \\
& Q_i \left[ \frac{\gamma_e}{\gamma_P} (u_\eta A)_e - \frac{\gamma_w}{\gamma_P} (u_\eta A)_w + \frac{\gamma_n}{\gamma_P} (u_\eta A)_n - \frac{\gamma_s}{\gamma_P} (u_\eta A)_s \right] = \\
& V \left\{ \langle \omega_i | \eta \rangle + \frac{1}{2} \frac{\langle \chi | \eta \rangle}{\Delta \eta} \left[ \left( \frac{\partial Q_i}{\partial \eta} \right)_+ - \left( \frac{\partial Q_i}{\partial \eta} \right)_- \right] \right\}.
\end{aligned} \tag{5.3}$$

In this equation, the volume and area terms are calculated by

$$\begin{aligned}
V &= r \, dx \, dr, \\
A_e &= A_w = r \, dr, \\
A_n &= r_n \, dx, \\
A_s &= r_s \, dx.
\end{aligned} \tag{5.4}$$

Due to the differencing methods used during the solution of the ODE's, some variable values are required at the midpoint of each face. These are typically scalar fluid properties, such as density and diffusivity, which are determined through linear interpolation methods. Due to the differences in advective and diffusive terms, different methods are used for each of the preceding situations. As an example, Eq. 5.5 demonstrates how this interpolation is conducted at the east face. This yields

$$\gamma_e A_e (u_\eta Q_i)_e \approx \gamma_e A_e U_{\eta,e} (f_e Q_{i,E} + (1 - f_e) Q_{i,P}), \tag{5.5}$$

where  $f_e$  represents the linear distance factor due to the cell spacing, subsequently providing the approximation of  $Q_{i,e}$  from the known values of  $Q_{i,P}$  and  $Q_{i,E}$ . In a similar fashion, the diffusive term is calculated at the cell face by the central differencing equation

$$-\gamma_e A_e \left( Dt \frac{\partial Q_i}{\partial x} \right)_e \approx -\gamma_e A_e \left( \frac{Dt}{\Delta x} \right)_e (Q_{i,E} - Q_{i,P}). \tag{5.6}$$

The spacing,  $\Delta x$  is determined by

$$\Delta x = x_E - x_P \tag{5.7}$$

In order to facilitate the numerical implementation of Eq. 5.3, each term is divided by  $V$ , such that

$$\begin{aligned}
& \frac{\gamma_e A_e}{\gamma_P V} \left( u_\eta Q_i - Dt \frac{\partial Q_i}{\partial x} \right)_e - \frac{\gamma_w A_w}{\gamma_P V} \left( u_\eta Q_i - Dt \frac{\partial Q_i}{\partial x} \right)_w + \\
& \frac{\gamma_n A_n}{\gamma_P V} \left( v_\eta Q_i - Dt \frac{\partial Q_i}{\partial r} \right)_n - \frac{\gamma_s A_s}{\gamma_P V} \left( v_\eta Q_i - Dt \frac{\partial Q_i}{\partial r} \right)_s - \\
& \frac{Q_i}{\gamma V} \left[ \frac{\gamma_e}{\gamma_P} (u_\eta A)_e - \frac{\gamma_w}{\gamma_P} (u_\eta A)_w + \frac{\gamma_n}{\gamma_P} (u_\eta A)_n - \frac{\gamma_s}{\gamma_P} (u_\eta A)_s \right] = \\
& \langle \omega_i | \eta \rangle + \frac{1}{2} \frac{\langle \chi | \eta \rangle}{\Delta \eta} \left[ \left( \frac{\partial Q_i}{\partial \eta} \right)_+ - \left( \frac{\partial Q_i}{\partial \eta} \right)_- \right].
\end{aligned} \tag{5.8}$$

Further, by defining the coefficients

$$\begin{aligned}
a_e &= \frac{\gamma_e A_e}{\gamma_P V} \left( -f u_\eta + \frac{Dt}{\Delta x} \right)_e, & a_w &= \frac{\gamma_w A_w}{\gamma_P V} \left( -f u_\eta + \frac{Dt}{\Delta x} \right)_w, \\
a_n &= \frac{\gamma_n A_n}{\gamma_P V} \left( -f v_\eta + \frac{Dt}{\Delta x} \right)_n, & a_s &= \frac{\gamma_s A_s}{\gamma_P V} \left( -f v_\eta + \frac{Dt}{\Delta x} \right)_s, \\
a_+ &= \frac{\langle \chi | \eta \rangle}{\Delta \eta \Delta \eta_+}, & a_- &= \frac{\langle \chi | \eta \rangle}{\Delta \eta \Delta \eta_-},
\end{aligned} \tag{5.9}$$

and also by defining specific mass flows across each of the faces as

$$\begin{aligned}
F_e &= \frac{(\gamma A u_\eta)_e}{\gamma V}, & F_w &= \frac{(\gamma A u_\eta)_w}{\gamma V} \\
F_n &= \frac{(\gamma A v_\eta)_n}{\gamma V}, & F_s &= \frac{(\gamma A v_\eta)_s}{\gamma V},
\end{aligned} \tag{5.10}$$

substitution of Eq. 5.9 and Eq. 5.10 into Eq. 5.8 yields

$$\begin{aligned}
& (a_e (Q_i - Q_{i,E}) + F_e Q_i) - (a_w (Q_i - Q_{i,W}) + F_w Q_i) \\
& + (a_n (Q_i - Q_{i,N}) + F_n Q_i) - (a_s (Q_i - Q_{i,S}) + F_s Q_i) \\
& = \omega_{\eta,i} + (a_+ (Q_{i,++} - Q_i) - a_- (Q_i - Q_{i,--})) + Q_i (F_e - F_w + F_n - F_s).
\end{aligned} \tag{5.11}$$

Eq. 5.11 represents the final discretised form of 5.3. Further rearrangement of this equation for  $Q_i$  yields

$$Q_i = \frac{\omega_{\eta,i} + \sum a_k Q_{i,K}}{a_P} \tag{5.12}$$

where  $k$  represents all boundaries (i.e.  $e, w, n, s, u, d$ , etc.) of a given node,  $K$ , and  $a_P = \sum a_k$ . This equation must be solved for all species, locations in physical space and locations in  $\eta$  space. The resulting size of the system of equations, combined with the inherent stiffness of the ODE's, necessitates a significant computational effort for solution.

## 5.2 Solution of Ordinary Differential Equations

Due to the nature of chemical interactions, specifically those used in modelling turbulent combustion and autoignition problems, a robust solver is required that is capable of dealing with large changes in chemical species over an extremely small time. These chemical interactions are known as stiff ODE's. The term stiff refers to the inherent instability in the equation, necessitating the use of a specialised solver and an extremely small time step during solution. Several different solvers have been created and used with various stiff chemistry interactions, such as LSODE [57], GEAR [60] and VODE [57]. Each of these solvers was developed at or in conjunction with the Lawrence Livermore National Laboratory with the intent of solving the stiff ODE's with minimal computational cost.

In the case of CMC, such a solver is required to capture the chemical interactions occurring within the CMC equations. Through testing and user feedback, it was determined that GEAR was unable to deal with sharp time variations present in some chemical mechanisms, which lead to the development of a more robust methodology [57]. The new solver produced through this work at the Lawrence Livermore Laboratory is the LSODE solver. Further development by the creators of the LSODE solver yielded significant improvements in terms of computational efficiency and reduction of computational resources required for a given problem. This revised solver is the version of VODE implemented in the CMC code used in this study. Further details of both the solver and its implementation are discussed in the Sec. 5.2.1 and Sec. 5.2.2, respectively.

### 5.2.1 VODE Solver

The Variable coefficient Ordinary Differential Equation (VODE) solver is chosen as the primary solver used in the current study for the solution of stiff ODE's occurring in the

CMC equations. VODE offers an increase in numerical stability and computational efficiency over other available solvers, such as GEAR and LSODE, respectively [57]. Through benchmarking studies conducted by the Lawrence Livermore Laboratory, it was determined that the improvements over LSODE could be up to 49%.

In order to provide a brief outline of the methodology of VODE, the following summary is provided. Further details on the structure and operation of VODE may be found in [57].

The initial step in solving the stiff chemical source term is to write the initial value problem, using

$$\dot{Y} = f(t, Y(t)), Y(t_0) = Y_0. \quad (5.13)$$

The basic linear multistep formulation for the chemical source term (stiff and non-stiff) is given by

$$\sum_{i=0}^{\kappa_1} \alpha_{n,i} Y_{n-i} + h_n \sum_{i=0}^{\kappa_2} \beta_{n,i} \dot{Y}_{n-i} = 0. \quad (5.14)$$

The variables  $\kappa_{1,2}$ ,  $\alpha_{n,i}$ ,  $\beta_{n,i}$  are calculated based on the stiffness of the problem as well as the results of the current and past timestep values in order to adapt to the solution at hand [57].

For the solution of these formulas, VODE uses a modified direct Newton iterative method. At the conclusion of the calculation for each timestep, the timestep size is modified to suit the kinetics. The solver continues in this fashion until the desired cumulative timestep or the maximum number of internal iterations are reached. The chemistry rate information is then returned to the CMC code.

The chemistry rate information provides the required details on the evolution of the various chemical species involved over a single timestep. These values are used in the CFD calculations to modify the flowfield for the following timestep.

## 5.2.2 Implementation of VODE Solver

As the VODE solver is required for the solution of stiff ODE's, it is called upon during the solution of the chemical source term equation. Specifically, the CMC code requires a solution of the equation

$$\frac{\partial Q_\alpha}{\partial t} = \frac{1}{2} \{ \langle \chi | \eta \rangle \} \frac{\partial^2 Q}{\partial \eta^2} + \frac{\langle \dot{\omega} | \eta \rangle}{\langle \rho | \eta \rangle}. \quad (5.15)$$

The solution of the chemical source term allows the CMC calculations to proceed with a revised mass fraction for each species, subsequently allowing for the calculation of all conditional species mass fractions, as well as Favre-averaged density and temperature. Competition between the mixing term,  $\frac{1}{2}\{\langle\chi|\eta\rangle\}\frac{\partial^2 Q}{\partial\eta^2}$ , and the chemical source term,  $\frac{\langle\dot{\omega}|\eta\rangle}{\langle\rho|\eta\rangle}$ , affect the overall rate of species evolution in Eq. 5.15.

The user interface of the VODE solver allows specification of the overall (CFD and CMC) timestep of the solution, which is broken up into a number of internal timesteps within the solver. The overall timestep employed in the current work on autoignition is  $1.0 \times 10^{-6}$ s. The VODE internal timesteps are limited to a maximum of 1000 per overall timestep, with a user specified internal solution relative tolerance of  $10^{-5}$  and an absolute tolerance of  $10^{-20}$ .

### 5.3 Chemical Mechanism

The hydrogen-oxygen chemical mechanism has been the focus of many studies, and various mechanisms have been published in order to provide some insight into the workings of this interaction. The kinetics proposed by Li et al. [50], O’Conaire et al. [51], Mueller et al. [52], Yetter et al. [53] and Konnov [54] all provide relevant mechanisms of varying levels of complexity with differing reaction steps and rate constants. In an effort to maintain continuity with the autoignition studies used in Ch. 7, the mechanism proposed by Yetter et al. [53] is chosen for both the validation study, Ch. 6, and the autoignition study, Ch. 7 in the present work.

In its original form, the mechanism proposed by Yetter et al. [53] is presented in Table 5.1. In this table, only the forward reaction coefficients are given for each reaction step, and it is stated that the reverse rate constants are to be computed from the forward rate constants and the equilibrium constants [53].

As the present computational code only accepts forward reactions, each of the reactions steps specified in Table 5.1 must be split into forward and reverse reactions with separate coefficients. Each of the forward and reverse reaction equations is seen as a separate and independent step by the code, with the net rate being equal to the sum of the forward and reverse rates. CHEMKIN, a chemical kinetics solver, is used to calculate the reverse rate coefficients from the information provided.

Table 5.1:  $H_2$ - $O_2$  reaction mechanism - forward reaction constants

Step		$A_f$	$n_f$	$E_{a_f}$
<i>H<sub>2</sub>-O<sub>2</sub> Chain Reactions</i>				
1	$H + O_2 = OH + O$	$1.91 \times 10^{14}$	0.0	16440
2	$H_2 + O = H + OH$	$5.08 \times 10^4$	2.67	6290
3	$OH + H_2 = H_2O + H$	$2.16 \times 10^8$	1.51	3430
4	$H_2O + O = OH + OH$	$2.02 \times 10^{14}$	2.02	13400
<i>H<sub>2</sub>-O<sub>2</sub> Dissociation/Recombination Reactions</i>				
5	$H_2 + N_2 = H + H + N_2$	$4.58 \times 10^{19}$	-1.4	104380
6	$O + O + N_2 = O_2 + N_2$	$6.16 \times 10^{15}$	-0.5	0.0
7	$O + H + N_2 = OH + N_2$	$4.71 \times 10^{18}$	-1.0	0.00
8	$H + OH + N_2 = H_2O + N_2$	$2.21 \times 10^{22}$	-2.0	0.0
<i>Formation and Consumption of HO<sub>2</sub></i>				
9	$H + O_2 + N_2 = HO_2 + N_2$	$3.5 \times 10^{16}$	-0.41	-1120
10	$HO_2 + H = H_2 + O_2$	$1.66 \times 10^{13}$	0.0	820
11	$HO_2 + H = OH + OH$	$7.08 \times 10^{13}$	0.0	300
12	$HO_2 + O = OH + O_2$	$3.25 \times 10^{13}$	0.0	0.0
13	$HO_2 + OH = H_2O + O_2$	$2.89 \times 10^{13}$	0.0	-500
<i>Formation and Consumption of H<sub>2</sub>O<sub>2</sub></i>				
14	$HO_2 + HO_2 = H_2O_2 + O_2$	$4.2 \times 10^{14}$	0.0	11980
14b	$HO_2 + HO_2 = H_2O_2 + O_2$	$1.3 \times 10^{11}$	0.0	-1630
15	$H_2O_2 + N_2 = OH + OH + N_2$	$1.2 \times 10^{17}$	0.0	45500
16	$H_2O_2 = H_2O + OH$	$2.41 \times 10^{13}$	0.0	3970
17	$H_2O_2 + H = H_2 + HO_2$	$4.82 \times 10^{13}$	0.0	7950
18	$H_2O_2 + O = OH + HO_2$	$9.55 \times 10^6$	0.0	3970
19	$H_2O_2 + OH = H_2OHO_2$	$1.00 \times 10^{12}$	0.0	0.0
19b	$H_2O_2 + OH = H_2OHO_2$	$5.80 \times 10^{14}$	0.0	9560

The reaction rates follow the Arrhenius rate law, given as [61]

$$k = AT^n \exp\left(\frac{-E_a}{RT}\right). \quad (5.16)$$

This expression is valid for both the forward and reverse reaction directions. In Eq. 5.16, the rate constant,  $k$ , is calculated using the pre-exponential factor,  $A$ , the temperature expressed in kelvin,  $T$ , the temperature dependence exponent,  $n$ , the activation energy,  $E_a$  and the universal gas constant,  $R$ . These rate coefficients, defined as  $k_{f_i}$  and  $k_{r_i}$  for the forward and reverse directions, respectively, can be combined to determine the equilibrium constant for reaction step  $i$ ,  $K_{C_i}$ , using the equation

$$K_{C_i} = \frac{k_{f_i}}{k_{r_i}}. \quad (5.17)$$

The equilibrium constant,  $K_{C_i}$ , is calculated in CHEMKIN by [62]

$$K_{C_i} = K_{P_i} \left(\frac{P_{atm}}{RT}\right)^{\sum_{k=1}^K \nu_{k_i}}, \quad (5.18)$$

with  $K$  representing the number of chemical species involved in reaction step  $i$ , and  $\nu_{k_i}$  representing the sum of the species coefficients in the stoichiometric reaction step equation. The values of the constants  $K_{P_i}$  are determined with the relationship

$$K_{P_i} = \exp\left(\frac{\Delta S_i^0}{R} - \frac{\Delta H_i^0}{RT}\right), \quad (5.19)$$

where  $\Delta S_i^0$  and  $\Delta H_i^0$  are the change in entropy and change in enthalpy in reaction  $i$ , respectively. These values are calculated via the thermophysical data input into CHEMKIN [62].

The forward and reverse activation energies,  $E_a^{(f)}$  and  $E_a^{(r)}$ , are related by the expression [61]

$$E_a^{(f)} - E_a^{(r)} = U_{products} - U_{reactants}. \quad (5.20)$$

Therefore, using the thermophysical data in conjunction with the forward activation energy, the reverse activation energy can be directly obtained.

Following the calculation of  $k_{f_i}$  and  $K_{C_i}$ , Eq. 5.17 is used to determine the reverse rate constant. This is combined with  $E_a^{(r)}$  in Eq. 5.16 to calculate  $A_r$ . These steps are repeated

for all of the individual reaction steps until the entire mechanism is fully defined. For the purposes of the calculation, it is assumed that the temperature dependence exponent,  $n$ , is independent of reaction direction [61].

This mechanism, as used in the current code is detailed in Tables 5.2 and 5.3. It should be noted that all relevant third body collisions occur using the  $N_2$  molecule, as other typical third body species, such as  $Ar$ , are not included in the simulation. This is done since the influence of  $Ar$  and other minor constituents acting as third bodies is negligible in comparison to the effects of  $N_2$ , and does not justify the increase in computational expense of adding another chemical species to the calculations.

Once the mechanism is fully defined, the output results in the present code are validated against CHEMKIN rate results under fixed conditions to ensure proper functionality.

## 5.4 Optimisation of CMC calculations

As mentioned in the introduction of Ch. 5, the computational expense of CMC calculations has the potential to be a major portion of the total calculation time. This problem is compounded when adding additional species to the mechanism, or additional refinements in  $\eta$ -space. Although the base calculations have not been modified to yield improved performance, two distinct strategies are presented which reduce the overall number of calculations required per iteration. Employing either of these strategies has the potential for significant reductions in computational expense, but other problems, such as instabilities and grid dependence may become significant if the proper care is not taken with implementation.

### 5.4.1 Dynamic CMC Grid

CMC calculations are very time consuming in comparison to the CFD calculations due to the complexity of the models and the solvers required. Any reduction in the effort required to solve these equations will therefore offer a noticeable improvement in the computational efficiency and usability of the code. Additionally, the CMC calculation grid must be set up to completely encompass the desired physical location of reaction, which is not always

Table 5.2:  $H_2$ - $O_2$  reaction mechanism - steps 1 - 13

Step		$A_f$	$n_f$	$E_{a_f}$
<i>H<sub>2</sub>-O<sub>2</sub> Chain Reactions</i>				
1-F	$H + O_2 \rightarrow OH + O$	$1.91 \times 10^{14}$	0.0	16440
1-R	$OH + O \rightarrow H + O_2$	$1.13 \times 10^{13}$	0.0	-330
2-F	$H_2 + O \rightarrow H + OH$	$5.08 \times 10^4$	2.67	6290
2-R	$H + OH \rightarrow H_2 + O$	$2.23 \times 10^4$	2.67	4440
3-F	$OH + H_2 \rightarrow H_2O + H$	$2.16 \times 10^8$	1.51	3430
3-R	$H_2O + H \rightarrow OH + H_2$	$9.95 \times 10^8$	1.51	18440
4-F	$H_2O + O \rightarrow OH + OH$	$2.02 \times 10^{14}$	2.02	13400
4-R	$OH + OH \rightarrow H_2O + O$	$2.02 \times 10^{14}$	2.02	-3480
<i>H<sub>2</sub>-O<sub>2</sub> Dissociation/Recombination Reactions</i>				
5-F	$H_2 + N_2 \rightarrow H + H + N_2$	$4.58 \times 10^{19}$	-1.4	104380
5-R	$H + H + N_2 \rightarrow H_2 + N_2$	$1.18 \times 10^{19}$	-1.4	180
6-F	$O + O + N_2 \rightarrow O_2 + N_2$	$6.16 \times 10^{15}$	-0.5	0.0
6-R	$O_2 + N_2 \rightarrow O + O + N_2$	$1.86 \times 10^{17}$	-0.5	119100
7-F	$O + H + N_2 \rightarrow OH + N_2$	$4.71 \times 10^{18}$	-1.0	0.00
7-R	$OH + N_2 \rightarrow O + H + N_2$	$8.35 \times 10^{18}$	-1.0	102300
8-F	$H + OH + N_2 \rightarrow H_2O + N_2$	$2.21 \times 10^{22}$	-2.0	0.0
8-R	$H_2O + N_2 \rightarrow H + OH + N_2$	$3.75 \times 10^{23}$	-2.0	119100
<i>Formation and Consumption of HO<sub>2</sub></i>				
9-F	$H + O_2 + N_2 \rightarrow HO_2 + N_2$	$3.5 \times 10^{16}$	-0.41	-1120
9-R	$HO_2 + N_2 \rightarrow H + O_2 + N_2$	$4.95 \times 10^{16}$	-0.41	47980
10-F	$HO_2 + H \rightarrow H_2 + O_2$	$1.66 \times 10^{13}$	0.0	820
10-R	$H_2 + O_2 \rightarrow HO_2 + H$	$4.55 \times 10^{13}$	0.0	55920
11-F	$HO_2 + H \rightarrow OH + OH$	$7.08 \times 10^{13}$	0.0	300
11-R	$OH + OH \rightarrow HO_2 + H$	$5.32 \times 10^{12}$	0.0	36770
12-F	$HO_2 + O \rightarrow OH + O_2$	$3.25 \times 10^{13}$	0.0	0.0
12-R	$OH + O_2 \rightarrow HO_2 + O$	$2.97 \times 10^{13}$	0.0	52230
13-F	$HO_2 + OH \rightarrow H_2O + O_2$	$2.89 \times 10^{13}$	0.0	-500
13-R	$H_2O + O_2 \rightarrow HO_2 + OH$	$3.48 \times 10^{14}$	0.0	69610

Table 5.3:  $H_2$ - $O_2$  reaction mechanism - steps 13 - 19

Step		$A_f$	$n_f$	$E_{a_f}$
Formation and Consumption of $H_2O_2$				
14-F	$HO_2 + HO_2 \rightarrow H_2O_2 + O_2$	$4.2 \times 10^{14}$	0.0	11980
14-R	$H_2O_2 + O_2 \rightarrow HO_2 + HO_2$	$3.24 \times 10^{15}$	0.0	50510
14b-F	$HO_2 + HO_2 \rightarrow H_2O_2 + O_2$	$1.3 \times 10^{11}$	0.0	-1630
14b-R	$H_2O_2 + O_2 \rightarrow HO_2 + HO_2$	$1.00 \times 10^{12}$	0.0	36900
15-F	$H_2O_2 + N_2 \rightarrow OH + OH + N_2$	$1.2 \times 10^{17}$	0.0	45500
15-R	$OH + OH + N_2 \rightarrow H_2O_2 + N_2$	$8.31 \times 10^{14}$	0.0	-5640
16-F	$H_2O_2 \rightarrow H_2O + OH$	$2.41 \times 10^{13}$	0.0	3970
16-R	$H_2O + OH \rightarrow H_2O_2$	$2.83 \times 10^{12}$	0.0	72020
17-F	$H_2O_2 + H \rightarrow H_2 + HO_2$	$4.82 \times 10^{13}$	0.0	7950
17-R	$H_2 + HO_2 \rightarrow H_2O_2 + H$	$1.71 \times 10^{13}$	0.0	24520
18-F	$H_2O_2 + O \rightarrow OH + HO_2$	$9.55 \times 10^6$	0.0	3970
18-R	$OH + HO_2 \rightarrow H_2O_2 + O$	$1.57 \times 10^6$	0.0	18670
19-F	$H_2O_2 + OH \rightarrow H_2OHO_2$	$1.00 \times 10^{12}$	0.0	0.0
19-R	$H_2O + HO_2 \rightarrow H_2O_2 + OH$	$1.56 \times 10^{12}$	0.0	31580
19b-F	$H_2O_2 + OH \rightarrow H_2OHO_2$	$5.80 \times 10^{14}$	0.0	9560
19b-R	$H_2O + HO_2 \rightarrow H_2O_2 + OH$	$9.05 \times 10^{14}$	0.0	41140

known beforehand. In order to combat these drawbacks, a dynamic CMC grid is used to provide a significant increase in the efficiency of calculations.

The dynamic grid is formulated on the assumption that relevant chemical reaction will not occur outside a given range of  $\tilde{\xi}$  values, such that

$$\eta_{min} \leq \tilde{\xi} \leq \eta_{max}. \quad (5.21)$$

The lower and upper bounds,  $\eta_{min}$  and  $\eta_{max}$ , respectively, are chosen such that the range encompasses any potentially reactive mixture fractions. When the value of  $\tilde{\xi}$  falls out of the range defined in Eq. 5.21, the CMC node is effectively turned off, and no calculations are performed at this location. An adjustable hysteresis value is set to limit boundary nodes turning on and off with slight fluctuations in  $\tilde{\xi}$  between subsequent timesteps. For example, at low mixture fraction values, a cell will become active at a slightly higher mean value than  $\eta_{min}$ , and in order for it to become inactive, the mean value must fall to a slightly lower mean value than  $\eta_{min}$ . A zero flux boundary is set for all of the CMC boundaries. The active nodes are updated at user specified time intervals.

The effects of the dynamic CMC grid are extremely noticeable at the early times of simulation and when there is very little fuel present in the domain, and in situations where there is no advanced knowledge of when or where chemical reaction may occur, such as with autoignition. This effect is demonstrated in Fig. 5.3, which is taken from an autoignition simulation. In Fig. 5.3 a), the black area represents the active CMC nodes at an early timestep of  $\tau = 0.500ms$  with approximately 10% of the CMC nodes active, while Fig. 5.3 b) represents the active CMC nodes at a later timestep of  $\tau = 2.000ms$ , with approximately 50% of the CMC nodes active. As it can be quite clearly seen from Fig. 5.3, there is a significant difference in the number of cells included in the calculation. This allows specification of a large initial CMC domain without the associated increase in computational cost.

Provided  $\eta_{min}$  and  $\eta_{max}$  are selected such that combustion does not occur at any of the CMC boundaries, there is no affect on the accuracy of the results.

Although the exact computational time savings are highly dependent on the flow parameters and area of simulation, the additional flexibility and usability afforded by this feature make the model significantly more accessible to industry type usage as opposed to solely being used in research.



(a) Active CMC Nodes (black) at an early timestep (b) Active CMC Nodes (black) at a later timestep

Figure 5.3: Dynamic CMC grid

### 5.4.2 CMC Grid Multiplier

As shown in previous work [10, 11], conditional average values of scalars have a weak radial dependence in self similar shear flows. In these studies, a cross-stream averaging technique is used to weight the conditional averages based on the PDF, yielding a single axial value. By reducing the number of CMC calculations required at each axial position, the computational efficiency of the simulations is significantly improved.

As it is shown that the grid sensitivity of CMC calculations can potentially be lower than the grid sensitivity of the CFD calculations, a provision is included in the current code that allows grouping of multiple CFD nodes into a single CMC node. This grid multiplier feature allows the user to specify the multiplier in any direction used within the simulation. For example, if the user wishes to specify a multiple of 3 in both the  $i$  and  $j$  directions, a single CMC node would overlap 9 CFD nodes (i.e. a 3x3 square). Therefore, under the aforementioned assumption that CMC calculations are less sensitive to spatial variations than the flowfield CFD calculations, a significant computational savings can potentially be realised.

Through a validation study completed, covered in greater detail in Ch. 6, it is observed that there is a significant axial dependence on the CMC grid spacing. Although cross-stream averaging techniques have proven successful in previous studies, the CMC grid multiplication feature is not used in either the axial or radial direction for the remainder of the study. Once baseline results have been established, future work in this area is advised

in order to demonstrate and refine the effectiveness of this method.

## 5.5 Summary

This chapter provides an examination of the method used to numerically implement the CMC model within the computational code used in the current work. The methods used to couple enthalpy and density back to the flowfield is highlighted. The finite volume discretisation of the CMC equations, which guarantees continuity with any grid spacing, is also presented in detail. Finally the solution of the chemical kinetics ODE's are outlined.

The detailed chemical mechanism used in this study is presented in a tabular form. It outlines each reversible reaction, broken into forward and reverse steps. The chemical rates are validated against CHEMKIN output to ensure proper calculation.

Although the solution of the CMC governing equation, Eq. 3.11, is inherently difficult and computationally expensive, several methods are discussed which may present a significant computational savings. The first, and most easily applied method, is the dynamic CMC grid. This method is shown to provide a significant reduction of computational expense when the flowfield or main reaction region is not known in advance. This allows the user more flexibility in defining the CMC domain without the risk of significant increase in the simulation time. The second method outlined was a CMC grid multiplier. This method was shown to be sensitive to grid spacing, requiring further experimentation. It is believed that with proper trials, it could be established to provide a reduction in computational expense proportional to the multiple used. Despite the potential for improvement, this is beyond the scope of the current work and it is recommended that future study be focused on this topic.

In summary, the CMC equations have been successfully and efficiently combined with a CFD code into a standalone package, not requiring a commercial or external code for flowfield solution. The code is easily configured for research work and is highly adaptable for many different flows and studies involving CMC, ranging from autoignition to fully developed flames.

The following chapter provides a detailed view of the initial validation study completed with the CFD-CMC code. The validation focuses on a steady state hydrogen jet flame into a quiescent ambient environment.

# Chapter 6

## Steady State Validation

The focus for this chapter is to outline the steps taken to validate the code against published results from an hydrogen jet flame. The preliminary validation allows an analysis of the characteristics of initial CFD and CMC model performance. The trends observed in the numerical prediction of the flowfield are compared to the known deficiencies with the  $k - \epsilon$  model. The conditional scalar results are presented for several locations in the flow in order to evaluate the general trends predicted by CMC. The predictions of  $\langle Y_{OH} | \eta \rangle$  are compared to experimental measurements in order to validate the chemical mechanism.

### 6.1 Boundary Conditions

The numerical study of this flame is carried out by reproducing the boundary conditions outlined in the experimental study [40]. The fuel inlet matches the experimental inlet of 3.75mm, and the outer diameter is correspondingly 4.8mm. As the flow has a Reynolds number of approximately 10000 [40], it is considered above the laminar-turbulent transition of 4000, and therefore follows the turbulent pipe flow profile which is relatively uniform across the diameter [63]. The velocity profile is therefore modelled as uniform across the fuel inlet. The fuel and coflow inlet are placed at the lower boundary of the domain, separate by an adiabatic wall representing the burner pipe thickness. The outer boundary of the domain was placed at a radial coordinate of 150mm, sufficiently far from the centreline

that boundary conditions had no impact on the flame structure. This outer boundary is modelled as an opening, allowing fluids to enter or exit the domain such that the flow remains unconfined. The top of the domain is modelled as an outlet boundary, allowing fluid to flow out of the domain without any restriction. The axial length of the domain is modelled as a total of 900mm, such that the flow exiting the domain was largely uniform. The planar boundaries confining the axisymmetric mesh slice are modelled as symmetry planes, meaning that all gradients perpendicular to these faces are held to zero.

The entire computational domain is represented by a structured hexahedral, axisymmetric mesh. The CFD mesh is composed of 188 nodes in the axial direction and 134 nodes in the radial direction. The areas of refinement are concentrated to areas where large spatial gradients in the flow are present, specifically in areas near the inlet and along the mixing surface between the jet and coflow. The final CFD grid is shown in Fig. 6.1.

The CMC calculations are performed using a grid directly overlapping the CFD grid. The lower boundary of the CMC domain begins approximately 20mm from the inlet and extends to 900mm axially downstream. In the radial direction, the CMC domain extends from the centreline to a radial coordinate of 150mm. Although the CMC grid is chosen in order to capture essentially the entire CFD grid, the dynamic CMC grid function was employed, automatically reducing the relevant calculation region only to the areas where significant chemical reaction occurs.

The CMC calculations are initialised by use of the flamelet combustion model, converged to  $10^{-4}$  residuals for mass and velocity, in which several flamelet libraries were used to provide a baseline initialisation of the various species mass fractions. Mixture fraction space was modelled using 60 nodes, with 40 of these concentrated in the region of 0 to  $4\eta_{st}$ . The remainder of the region was gridded using the remaining 20 nodes. The same mixture fraction grid is used for both the flamelet and CMC calculations, and is shown in Fig. 6.2 and Fig. 6.3.

The AMC mixing model, introduced in Sec. 3.5.1, was used for the steady flame in this chapter.

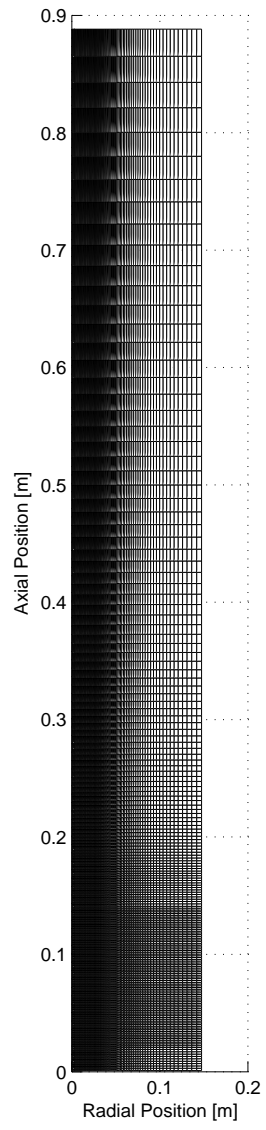


Figure 6.1: Final Steady State Mesh

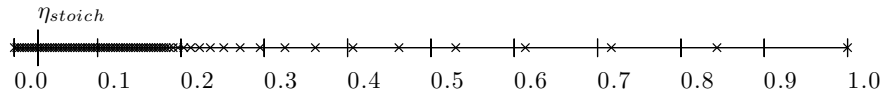


Figure 6.2: Full mixture fraction grid used for both flamelet and CMC calculations in steady state validation case

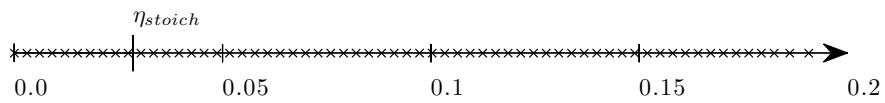


Figure 6.3: Partial mixture fraction grid between  $\eta = 0$  and  $\eta = 0.2$  used for both flamelet and CMC calculations in steady state validation case

## 6.2 CMC Grid Density Sensitivity Analysis

Originally introduced in Sec. 5.4.2, the CMC grid density multiples used are required to be odd positive integers, such that the centre of the CMC cell will always overlap exactly with the centre of a CFD cell. This restricts the value of the multiple to the numbers 1, 3, 5, 7, ..., etc. An internal algorithm is used to correctly match the CFD and CMC coordinates to allow for effective coupling of the calculations.

Initial experimentation with the CMC grid density multiplier investigated using a multiple of 3 in both the  $i$  and  $j$  directions, corresponding to one CMC cell overlapping 9 CFD cells. Although the initial trends noticed in computational expense were positive, with the modified grid taking only slightly more than  $1/9^{\text{th}}$  of the total computational time, it was immediately noticed that the revised CMC grid presented numerical difficulties. The results, calculated to the point where the solution would not converge further, indicated that large oscillations in temperature were occurring in the flowfield. These oscillations appeared in seemingly random, completely unphysical patterns. It was found that by refining the grid further, this unphysical behaviour in calculated temperatures disappears.

Although it was shown in Sec. 5.4.2 that CMC results are less sensitive to spatial grid spacing than CFD results, especially in the radial direction using cross-stream averaging techniques, it was demonstrated that there was still an inherent sensitivity to the calculations with both the axial and radial direction multipliers. The radial sensitivity may be eliminated by introducing a cross stream averaging technique [10, 11], the intent of this code is to provide a more general application of CMC, not restricting it to a single type of jet flow.

Through this experimentation, it was generally concluded that there is a maximum allowable grid spacing for which the CMC calculations can be performed with sufficient reliability, and that in the current flow, this limit is reached before the CFD calculations become sensitive to grid spacing. As the CMC calculations consume the majority of the computational time, this minimum CMC grid effectively determines the total calculation time required for a given simulation, and the impact of the CFD calculations are minimal in terms of the overall computational efficiency. It is possible that the observed spatial grid CMC sensitivities may change in differing flows, and requires further testing for validation of this effect.

For these reasons, the grid multiplier was not used in the remainder of this study.

## 6.3 Numerical and Experimental Comparison

The comparisons possible between the validation simulation and the experimental results are largely limited to those published in [40]. This section examines the differences in the CMC code predictions in comparison to the experimentally observed values by Barlow and Carter [40]. This limits the possible comparisons to temperature, mean mixture fraction and conditional  $OH$  mass fraction. Further, mean mixture fraction variance,  $\widetilde{Z''^2}$ , conditional temperature,  $\langle T | \eta \rangle$ , conditional  $H_2O$  mass fraction,  $\langle Y_{H_2O} | \eta \rangle$ , and conditional scalar dissipation rate,  $\langle \chi | \eta \rangle$ , will be presented at various locations in the flowfield. Velocity results, which were not included in the original publication, were made available through a subsequent numerical study published by Barlow et al. [41].

It should be noted that only the chemical mechanism presented in Sec. 5.3 will be used. Although various kinetics mechanisms are available for use, the mechanism presented by Yetter et al. [53] will be used for continuity with the existing autoignition studies compared in Ch. 7. Therefore, the qualitative and quantitative results are analysed accordingly. Analysis of the effects of various mechanisms is performed by Stanković et al. [47], and is discussed previously in Sec. 4.2.4.

### 6.3.1 Favre-Averaged Flowfield Results

#### Favre-Averaged Velocity

The initial stage of comparison with the experimental results is to examine the flowfield predicted by the computational code with that seen experimentally. A comparison of the Favre-averaged velocity and Favre-averaged mixture fraction values provides a good indication of how the code predicts the general mixing trends in the flowfield.

The centreline velocity predictions indicate that there is a general underprediction of jet velocities through the domain, shown in Fig. 6.4. Near the inlet, it can be seen that there is a sharp drop off in velocity as the jet mixes with the surrounding air. Proceeding along the centreline, the numerical predictions closely follow the trends demonstrated by

measurements; however the underpredictions remain consistent throughout the length of the domain. This underpredicted velocity corresponds to a general underprediction of jet penetration.

Radial velocity profiles in [41], are shown in Fig. 6.5. In Figs. 6.5 a) - c), the velocity profiles are shown in comparison to the experimental results at 3 locations:  $L/8$ ,  $L/2$  and  $3L/4$  [41]. The peak centreline velocities are underpredicted by approximately 35%, corresponding to the centreline plot in Fig. 6.4; however, it is qualitatively observed that the total jet momentum at a given axial location appears to be conserved, as the overprediction of spreading by the numerical simulation leads to higher velocities further from the centreline. The crossover point in experimental and numerical values moves outward as the jet spreads throughout the domain.

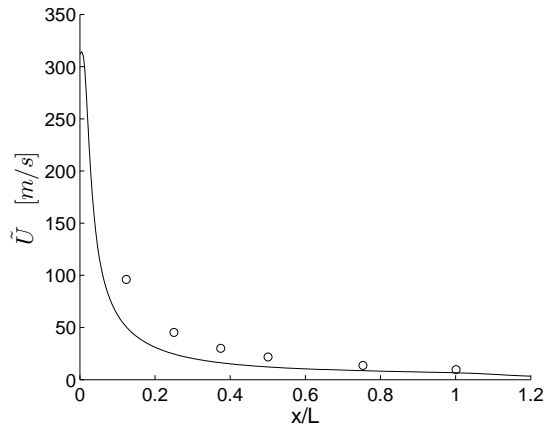
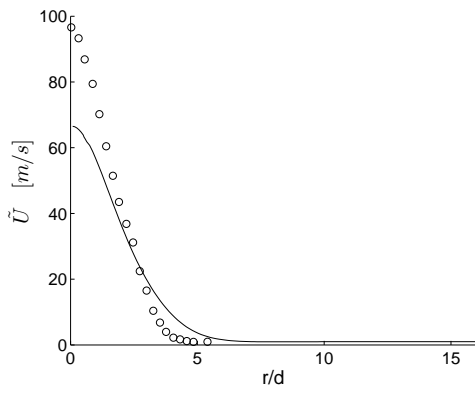


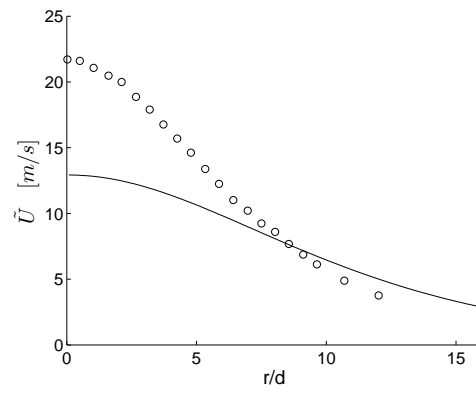
Figure 6.4: Centreline  $\tilde{U}$  [m/s] profile

### Mean Mixture Fraction

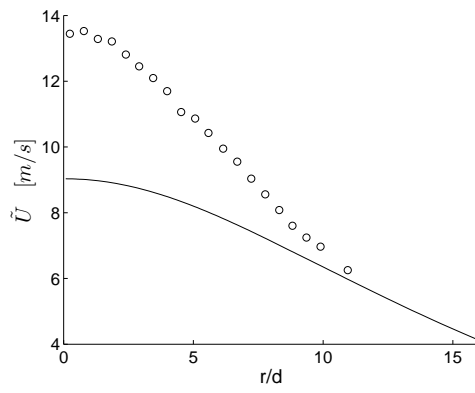
When examining the centreline values, Fig. 6.6, the underprediction in the radial profiles is clearly shown, similar to the velocity results in 6.4. Once again, it can be seen that the centreline numerical values drop off more suddenly than experimental values, a trend that is maintained through the length of the domain. As is expected, the trends in mean mixture fraction correlate well with those seen for velocity, indicating that the velocity and mixture fraction fields are closely related.



(a)  $L/8$



(b)  $L/2$



(c)  $3L/4$

Figure 6.5:  $\tilde{U}$  [m/s] radial profiles at different axial locations

In Figs. 6.7 a) - f), the numerical and experimental mixture fraction fields are compared at the  $L/8$ ,  $L/4$ ,  $3L/8$ ,  $L/2$ ,  $3L/4$  and  $L$  locations. Fig. 6.7 a) demonstrates that close to the inlet, there is a strong shear layer present, as there is a strong mixture fraction gradient moving outwards from the centreline. At this axial location, it can be seen that although the experimental and numerical results predict similar values at the  $r/d = 3$  location, the numerical results are beginning to overpredict spreading beyond this location. Moving further downstream to the  $L/4$  location, this trend continues, with an underprediction of the centreline mixture fraction by approximately 35%, and a corresponding overprediction of spreading beyond the  $r/d = 4$  position. At the  $3L/8$  position, shown in Fig. 6.7 c), the centreline underprediction remains at approximately 35% with the overprediction of spreading. This trend remains largely the same for the remainder of the measured locations, shown in Figs. 6.7 d) - f), with the crossover point between the experimental and numerical values moving outward proportional to the jet width. This outward movement indicates spreading of the mixing layer and the increase in the overall jet width. This appears to occur at approximately the same rate as with velocity, substantiating the previous results of mixing layer and jet spreading.

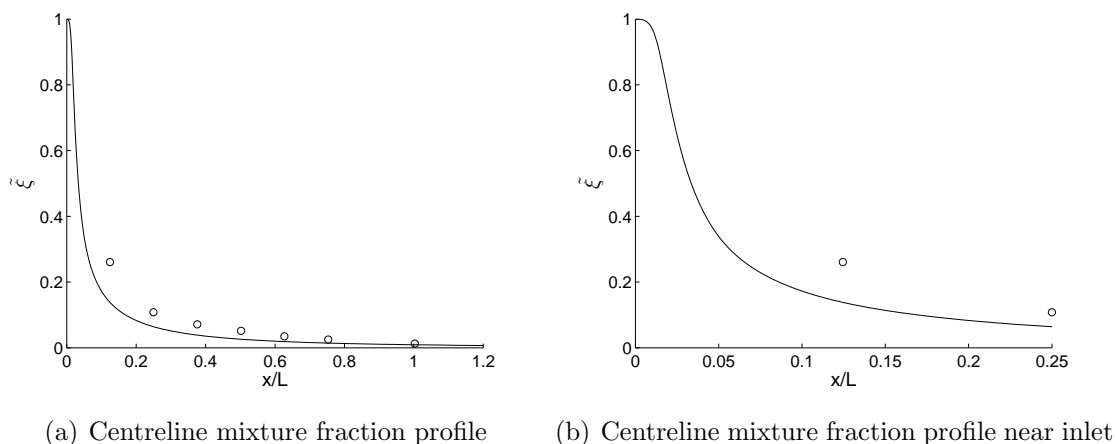


Figure 6.6: Centreline mixture fraction profile

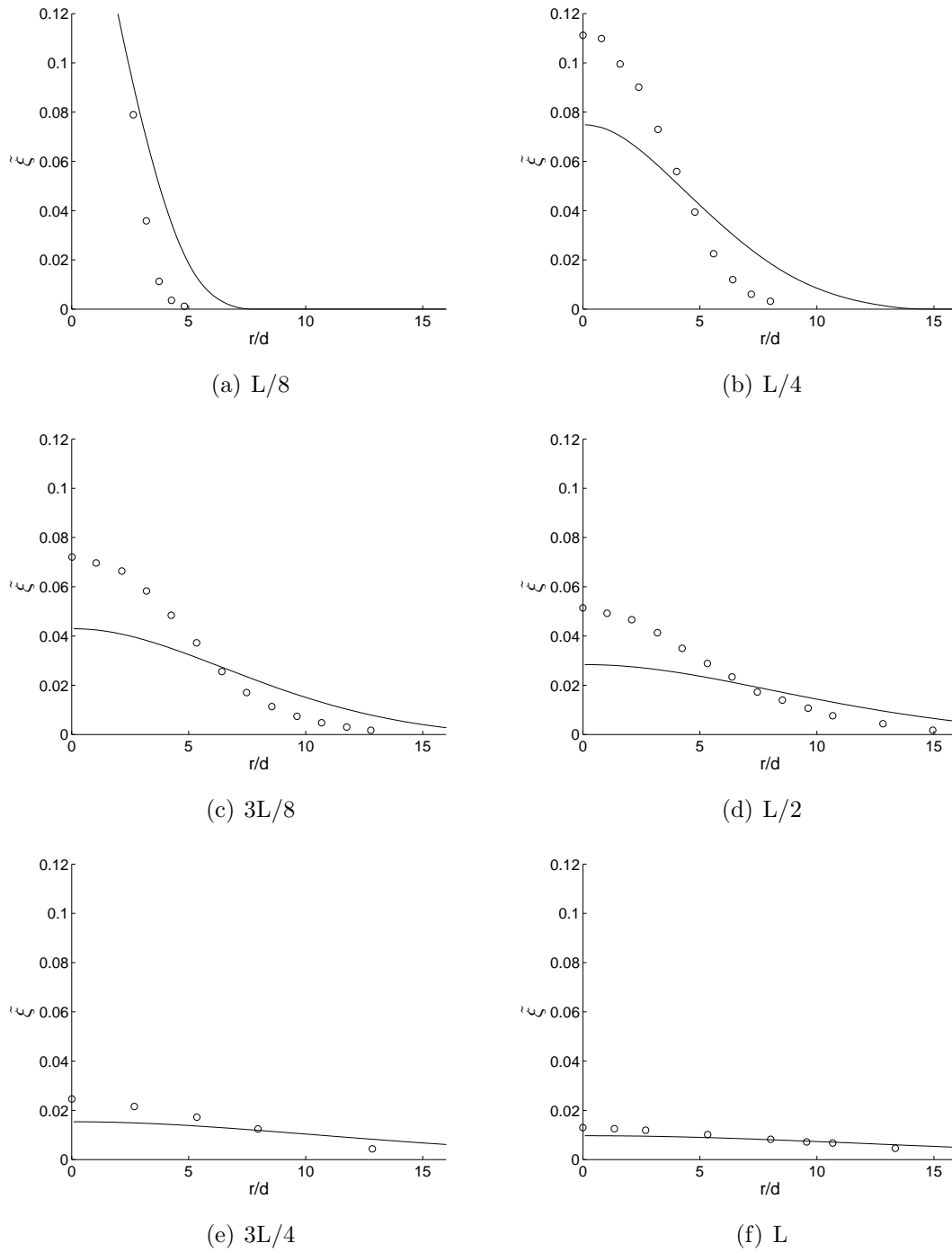


Figure 6.7: Mixture fraction radial profiles at different axial locations

## Favre-Averaged Temperature

Observation of the Favre-averaged temperatures predicted in the numerical domain provides the first insight into the functioning of the CMC calculations in conjunction with the specified chemical kinetics. Proper prediction of the Favre-averaged temperatures indicates that the calculations are predicting reasonable mixing rates within the flow as well as the proper species production and destruction rates.

In addition to demonstrating proper mixing and chemistry within the CMC calculations, the Favre-averaged temperature predictions are highly dependent on the spatial prediction of the mixture fraction field. Unlike mixture fraction and velocity, the temperature predictions are not only dependent on conservation equations, such as mass, momentum or mixing, but are also functions of several additional variables, such as the chemical mechanism and mixture fraction. As a result, peak flame temperatures are highly dependent on the mixture fraction, and are expected to closely follow the trends predicted in Fig. 6.7 and Fig. 6.6. It should be noted that the Favre-averaged temperature is not directly calculated, but rather is derived from the mixture enthalpy calculated by Eq. 5.1.

Following closely with the velocity and mixture fraction fields, the centreline temperature profile in Fig. 6.8 demonstrates a trend of overpredicting spreading, with earlier peak temperatures. The peaks occur earlier than the measured values due to the underprediction of centreline mixture fraction and reduction of the influence of convection at the centreline. The lower predictions of mixture fraction values result in the reaction zone moving upstream in comparison to experimental results, and correspondingly, the peak temperatures also shift upstream. The numerical results also demonstrate an earlier decline in temperature downstream of the reaction zone, which is a further indication of increased mixing and spreading of the mixture enthalpy throughout the computational domain.

The predicted Favre-averaged radial temperature profiles are shown in Figs. 6.9 a) - f). Comparisons to the measured values are made at  $L/8$ ,  $L/4$ ,  $3L/8$ ,  $L/2$ ,  $3L/4$  and  $L$  axial positions. In Fig. 6.9 a), it can be seen that the predicted temperatures follow the magnitude of the experimental results closely, once again with an overprediction of spreading. The peak temperatures are essentially identical to the experimental results, suggesting that although the jet spreading is overpredicted at the  $L/8$  location, the mixing and chemical kinetics predictions are a very good fit to the chemical interactions. It is apparent that the temperature peak exists off centre at this location, indicating that the jet core is still too rich for significant chemical interaction. Within the mixing layer at the

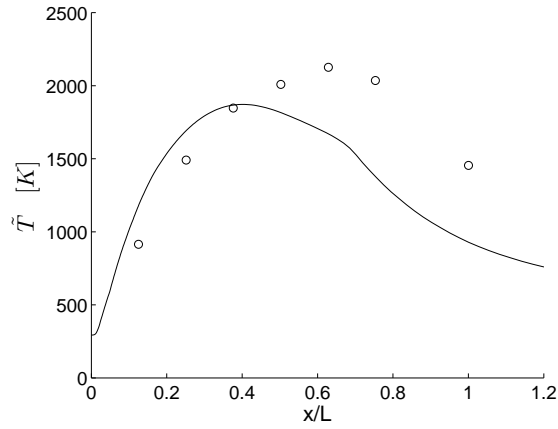


Figure 6.8: Centreline  $\tilde{T}$  [K] profile

edge of the jet, there is a locally stoichiometric mixture fraction region, shown previously in Fig. 6.7 b), and the chemical reactivity, and therefore temperature, peak in this area. Further downstream, as shown in Fig. 6.9 b), a similar, yet less defined radial temperature profile can be seen. At this location, the peak temperature predicted numerically is slightly lower than that measured experimentally. It is also observed that the jet core temperature is higher than the experimental measurements. This suggests that the level of mixing within the jet or the diffusion of heat is overpredicted. The cause of this is likely related to the general underprediction of jet penetration length and overprediction of spreading observed in the mixing field, i.e. at the lower predictions in centreline convection, resulting from lower velocities, is counteracted by a larger contribution of heat diffusion, pushing the flamefront and peak temperature upstream towards the inlet. At the  $3L/8$  location, shown in Fig. 6.9 c), the numerical temperature predictions no longer demonstrate a peak in temperatures due to reaction occurring at the edge of the jet, but rather show a peak occurring at the domain centreline. The lack of defined reaction zone indicates that sufficient mixing has occurred such that the core of the jet is now approaching stoichiometry and is beginning to increase in chemical reactivity and species evolution. This trend continues further downstream as shown in Fig. 6.9 d) to f). Although this mixing trend predicted numerically is reflected in the experimental results, it occurs further downstream in the experimental case, substantiated by the mixture fraction results, which show only a slight radial dependence at the  $3L/4$  location. Beyond this point, both the experimental and numerical results show significantly flatter curves due to the additional mixing and radial

diffusion of heat.

### Mean Mixture Fraction Variance

Although the mean mixture fraction variance, or  $\widetilde{Z''^2}$ , was not published with the experimental results, it provides a further metric of analysing the flowfield. The variance, which is a scalar quantity for which there is a transport equation solved, is used with the mean mixture fraction to ascertain a statistical distribution of the flow parameters, as described in Sec. 3.4.4. While the mean value provides an expected value for a fixed point in space, the variance represents the magnitude of the fluctuations about the mean value. Therefore, in well mixed areas, such as far downstream from the inlet, or at large radial coordinates, the variance is expected to be the lowest since these areas will either be fully mixed or no mixing will be present due to the absence of fuel. The highest  $\widetilde{Z''^2}$  values are likely to exist near the inlet or in the shear layer between the fuel and oxidiser, where the largest fluctuations occur in the flow.

The strong peak of the centreline variance, and the asymptotic decrease with increasing axial position, is clearly visible in Fig. 6.10. The shape of the centreline variance prediction is very similar to that obtained by Markides et al. [35], even though the study was completed using n-heptane instead of hydrogen. This result indicates that far downstream from the inlet, the fuel and oxidiser are well mixed, with peak variance occurring in the jet mixing layer.

At the L/8 position, Fig. 6.11 a), it can be seen that there is a peak in variance at  $r/d = 2$ . Although this indicates strong mixing and high levels of fluctuations, it does not correspond directly to a large Favre-averaged temperature, which peaks at approximately  $r/d = 4$  in Fig. 6.9 a). In fact, peak temperatures are observed to occur outside of the peak variance layer, indicating that the mixing layer reduces mixture temperatures. This is largely due to the fact that when the variance increases relative to the mean value, the PDF is spread further across  $\eta$ -space, resulting in weaker and wider peaks and a more constant profile overall. The resultant wide PDF due to the large variance means that the temperature obtained when performing Favre-averaging is influenced by a larger section of  $\eta$ -space, damping any peaks in conditional values. Moving outward radially, as the variance decreases, the area of influence in the conditional scalar curves narrows due to a sharper PDF, resulting in stronger peaks, and ultimately higher Favre-averaged temperatures due

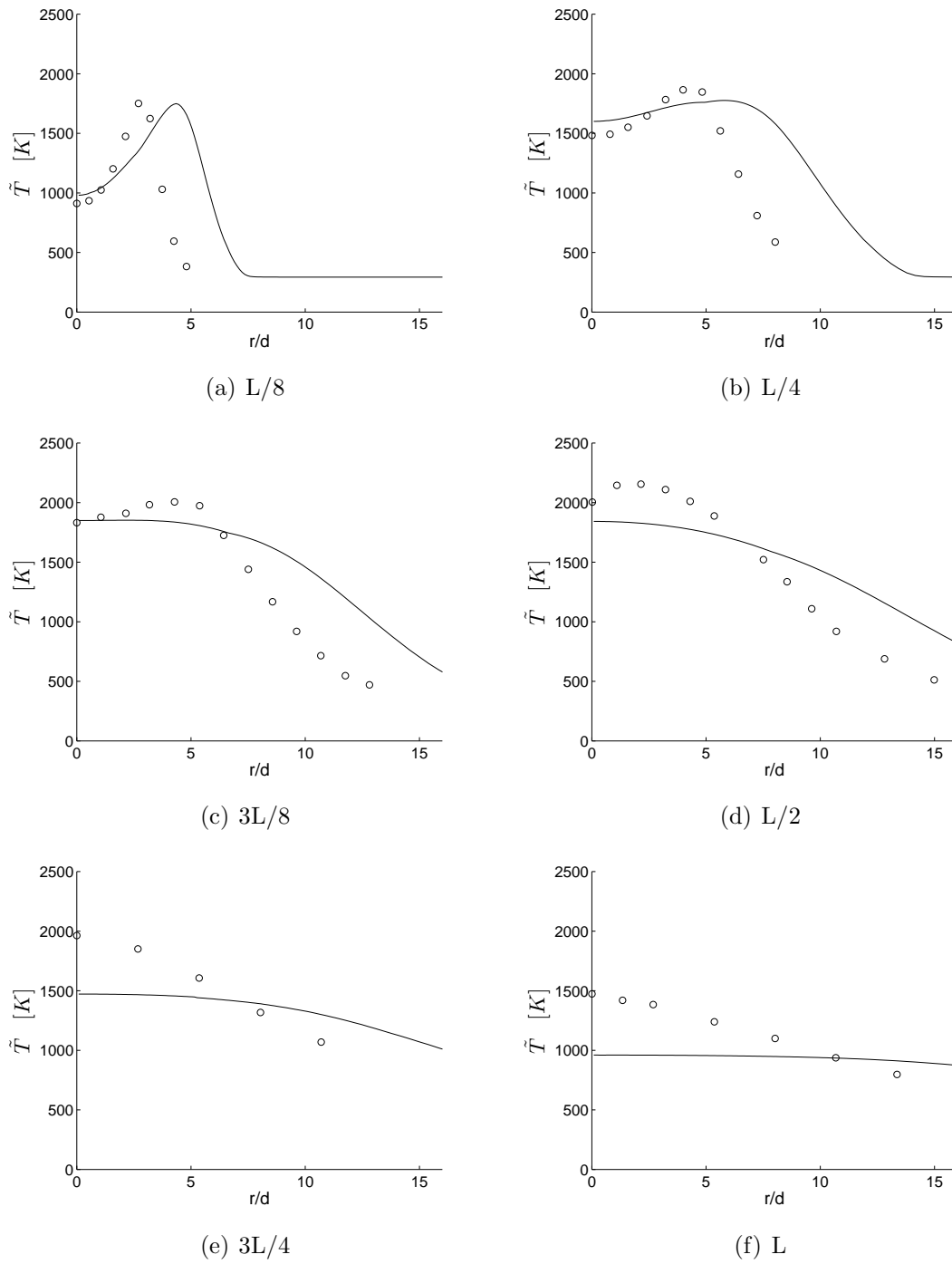


Figure 6.9:  $\tilde{T}$  Radial profiles at different axial locations

to peak chemical activity being captured. Proceeding further outward, the variance and mean mixture fraction values decrease further as the PDF moves away from the chemical peaks near stoichiometry in  $\eta$ -space. Proceeding downstream to the L/4 position, Fig. 6.11 b), it can be seen that although there is still a peak in variance due to the mixing layer, it has shifted outward radially and the magnitude has decreased significantly. Still further downstream, in Figs. 6.11 c) - f), the variance further decreases, with the peak moving outward radially. Please note that the scales are not constant in Figs. 6.11 a) - f) to best highlight the evolution of the radial variance profile.

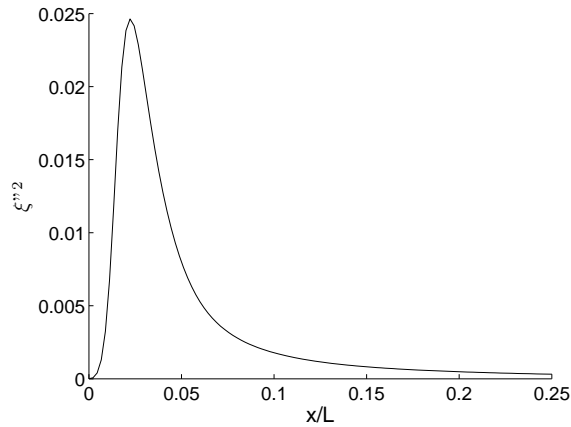


Figure 6.10: Centrelines  $\widetilde{Z''^2}$  profile

## Discussion of Favre-Averaged Results

The most immediately apparent observation when inspecting all of the Favre-averaged results is the underprediction of jet penetration and corresponding overprediction of spreading. This is a trend noticed in all of the Favre-averaged values presented: temperature, mixture fraction and velocity.

Although the underpredictions of the scalars  $\widetilde{U}$  and  $\widetilde{\xi}$  at the centreline appear to be significant, on the order of 35%, this result is not uncommon or unexpected when using the  $k - \epsilon$  turbulence model. Indeed, it has been widely documented that the constants,  $C_{\epsilon_1}$ ,  $C_{\epsilon_2}$ , and in some cases  $C_{\epsilon_3}$  [41], must be modified to obtain accurate results for the round-jet case [6, 64, 65, 66, 67]. No subsequent modification of the  $k - \epsilon$  model constants

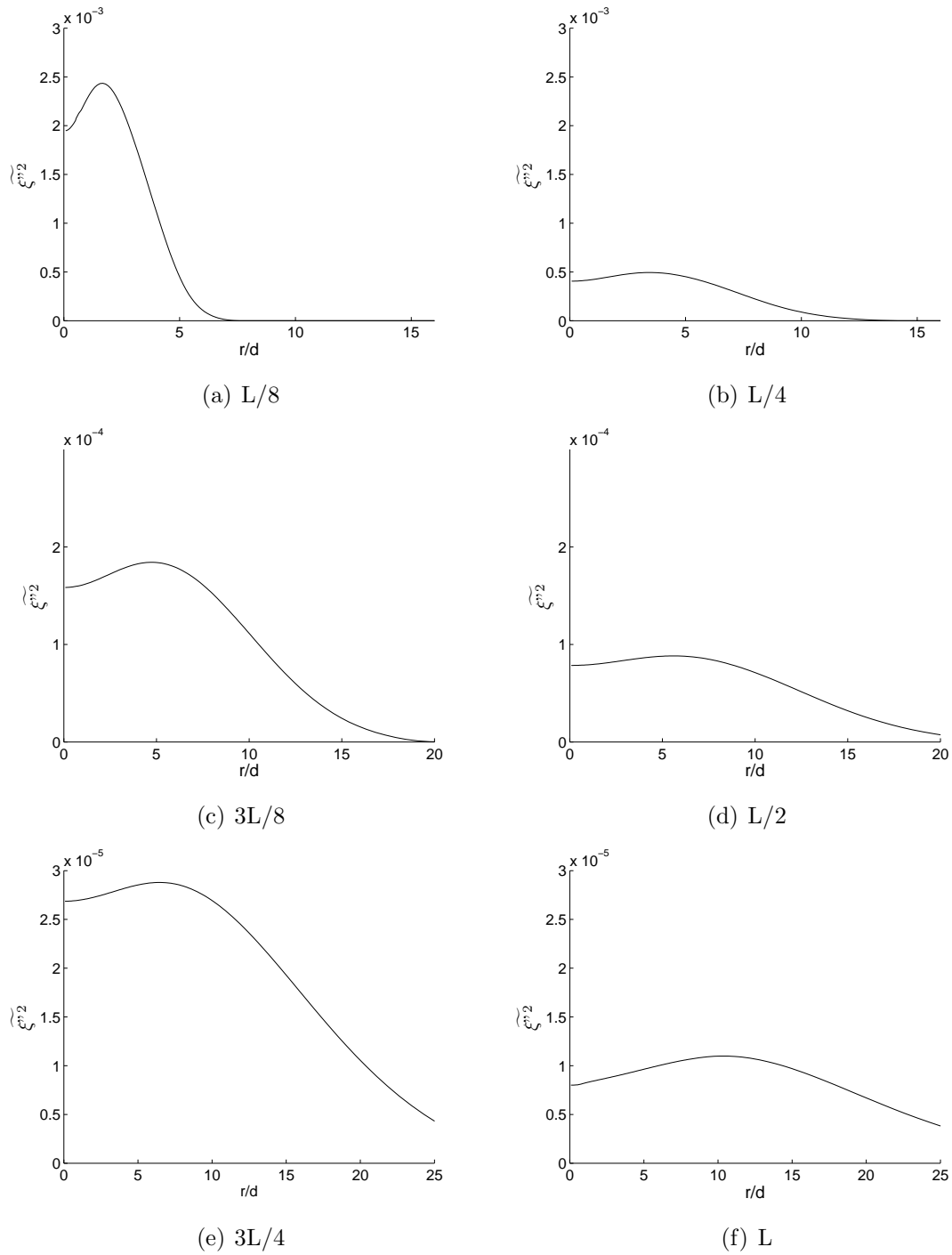


Figure 6.11: Mean mixture fraction variance,  $\overline{\xi''^2}$ , radial profiles at different axial locations, note that the axis scales are not constant

is made for the current simulation, as the intent of this chapter is only to characterise the overall performance of the model and not to exactly match experimental results, as the flow examined in Ch. 7 differs significantly from the current flow.

Despite the magnitude of the velocity and the mixture fraction being underpredicted along the centreline, it is encouraging to observe that the predicted radial temperature profiles are very close in magnitude to the experimental measurements. The centreline temperature profiles, however, appear to be shifted upstream in comparison to the measured results. This upstream shift can be attributed to the overall underprediction of jet penetration, i.e. the ignition and combustion processes occur further upstream in the numerical simulations than experimentally. This upstream shift occurs because the magnitude of  $\langle \chi | \eta \rangle$  is strongly linked to the prediction of the  $\tilde{\xi}$  and  $\widetilde{\xi''^2}$  fields. The overall peak centreline temperature is lower than what is observed experimentally. However, despite the lower centreline temperatures, the radial temperature profiles, especially upstream of the L/2 location, provide very similar magnitudes when compared to the measured values. These results indicate that there may be an underprediction of the conditional scalar dissipation rate near the fuel inlet, leading to the earlier onset of combustion, while there is an overprediction of the conditional scalar dissipation rate while moving downstream, evidenced by the lower peak temperatures seen numerically.

Although it is mainly focused on predictions of nitric oxide formation, a numerical study by Barlow and Carter [41] is available for the current hydrogen jet flame. In this study, modifications of the turbulence parameters, specifically  $C_{\epsilon_3}$ , are required in order to match the flowfield measurements [40, 41]. With this modification, excellent agreement with experimental results is obtained for velocity, mean mixture fraction and Favre-averaged temperature.

The results of the Barlow and Carter CMC study [41] show that the CMC model is capable of providing excellent Favre-averaged flowfield results when turbulence parameters are properly adjusted. Results from the current study in addition to the findings of Barlow and Carter [41] indicate that the present code has the ability to closely match what is seen experimentally.

### 6.3.2 Conditional Results

As a method of further investigation into the operation and accuracy of the CMC calculations, the conditional scalar values may be investigated. Conditional values, which are a function of position and  $\eta$ , show the possible values for a scalar at any mixture fraction value. Conditional values can be used to quantify mixing, temperature, species mass fraction, etc. In many cases, it is possible to measure intermediate species conditional mass fractions, which can subsequently be used as a means to validate chemistry mechanisms.

This section will present conditional values at various spatial positions for the scalars  $OH$  mass fraction,  $Y_{OH}$ , temperature,  $T$ , and scalar dissipation rate,  $\chi$ . A direct comparison is made between numerical and experimental  $OH$  mass fraction values.

#### Conditional Scalar Dissipation Rate

The conditional scalar dissipation rate,  $\langle \chi | \eta \rangle$ , is one of the most crucial conditional terms in combustion modelling, in particular CMC, as it represents the strength of mixing within the flow. The mixing largely controls the chemistry and can influence ignition and extinction performance of the fuel. As a result, the conditional temperature and conditional species mass fractions are largely dependent on the magnitude of the conditional scalar dissipation rate.

Although it was not measured experimentally, it is important to document the results seen with  $\langle \chi | \eta \rangle$  at various locations in the flow in order to further analyse other conditional results. Results are taken at three different axial locations,  $L/8$ ,  $3L/8$  and  $3L/4$ . At each of these axial locations, the results are subsequently split into 3 radial locations,  $r/d = 0$  (centreline),  $r/d = 5$  and  $r/d = 10$ . At the  $L/8$  location, an additional radial location at  $r/d = 2$  is included to capture the evolution of the profile near the centreline. Each of these locations is plotted under the same conditions for a small region of  $\eta$ -space around stoichiometry as well as the entirety of  $\eta$ -space. These different plots are placed alongside each other in Fig. 6.12.

The conditional scalar dissipation rates at the  $L/8$  axial position are shown in Fig. 6.12 a) and b). At this location, it can be seen that the mixing is strongest at the  $r/d = 2$  location, due to the presence of the mixing layer. The magnitude decreases both inward towards the centreline and outwards to the  $r/d = 5$  position, further decreasing to essen-

tially 0 by the time the  $r/d = 10$  position is reached. The strong mixing concentrated near the centreline will have a delaying effect on the onset of ignition, while lower mixing levels nearer the edge of the flame, combined with a near stoichiometric mixture fraction will promote the onset of ignition. At the  $r/d = 10$  location, the extremely low mixing predicted is an indication of little to no fuel being present so far outside the mixing layer. This is substantiated by the predictions of mean mixture fraction in Fig. 6.7 a), which also indicates essentially zero fuel present at this radial extent. At the  $3L/8$  location, shown in Fig. 6.12 c) and d), peak mixing can be seen at the  $r/d = 5$  location. The conditional scalar dissipation rate decreases once again towards the centreline as well as radially outward. This once again indicates the presence of a mixing layer near the edge of the jet. This mixing layer moves outward with increasing axial distance. The  $3L/4$  location, Fig. 6.12 e) and f), shows further development of the strong mixing layer. The peak  $\langle \chi | \eta \rangle$  values are seen further outward, at the  $r/d = 10$  location. In all cases, the peaks appear to follow the progression of the radial variance plots, seen in Fig. 6.11 a), c) and e). At all locations, the  $\langle \chi | \eta \rangle$  profiles dictated by the AMC model, as shown in Fig. 3.1.

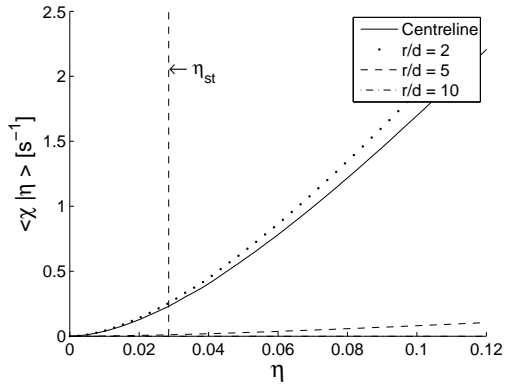
The presence of the mixing layer will have a delaying affect on the ignition in this region, or in locations where the mixture is already burning, the level of mixing will suppress peak temperatures. The proper prediction of  $\langle \chi | \eta \rangle$  is one of the most important aspects of performing accurate CMC calculations. This will be discussed further in Ch. 7 where an additional mixing model, the inhomogeneous model, is implemented.

### Conditional *OH* Mass Fraction

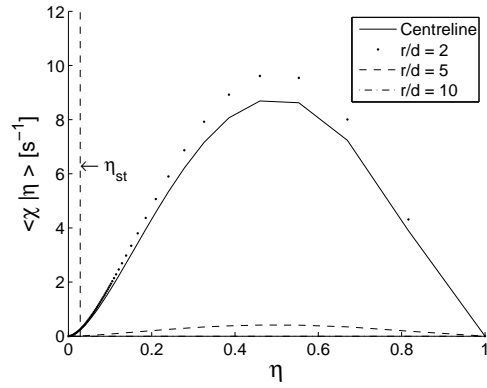
The radical *OH* is an intermediate species in the hydrogen combustion mechanism. This radical, which is short lived in the combustion process, provides information about the state of the radical pool [40] and is responsible for the chemiluminescence that occurs during the combustion process [42]. As a result, the *OH* radical is often used as a metric for comparison between experimental and numerical results.

The conditional *OH* mass fraction is the only experimentally available conditional value from the study by Barlow and Carter [40]. Measurements were performed along the centreline of the flame in 3 axial locations,  $L/8$ ,  $3L/8$  and  $3L/4$ . These are presented in the form of a scatter plot [40].

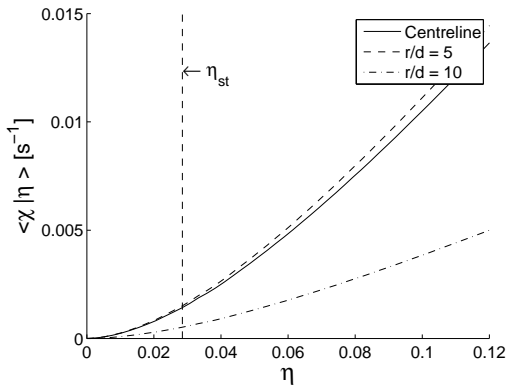
It can be seen in Fig. 6.13 a) to c) that there is a narrow band of chemical activity where



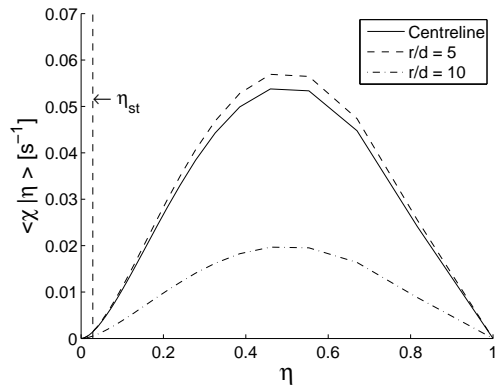
(a) Partial Profile at  $L/8$



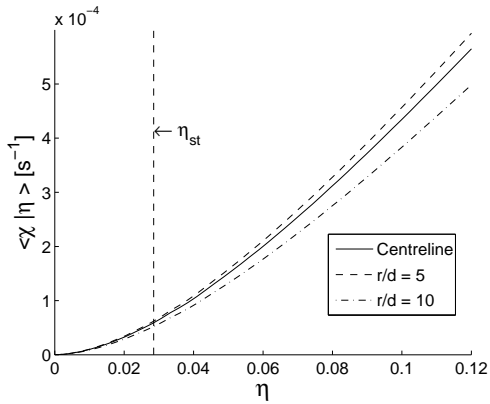
(b) Full Profile at  $L/8$



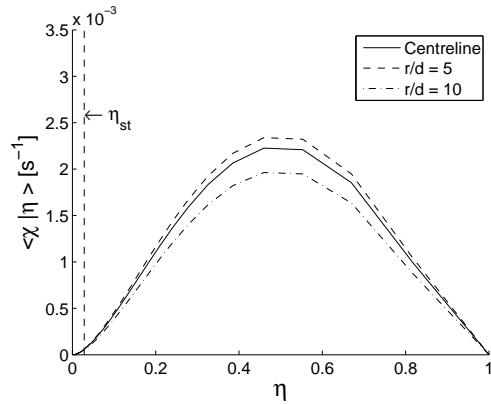
(c) Partial Profile at  $3L/8$



(d) Full Profile at  $3L/8$



(e) Partial Profile at  $3L/4$



(f) Full Profile at  $3L/4$

Figure 6.12:  $\langle \chi | \eta \rangle$  profiles at multiple axial and radial positions

the OH radical exists in significant quantities, focused mainly around the stoichiometric mixture fraction. At the L/8 position shown in Fig. 6.13 a), where mixing is the most intense, the experimental results show the largest variation in values, with a maximum  $Y_{OH}$  of around 0.02. To the rich side of the peak in the numerical results, it can be seen that the predictions closely follow the experimental measurements, while on the lean side of the peak, there is a slight underprediction of the conditional OH mass fraction. At this location, the discrepancy in experimental and numerical results may be caused by the difference in chemical reactivity, indicated by the centreline temperature profile in Fig. 6.8. Moving downstream to the 3L/8 and 3L/4 locations, Fig. 6.13 b) and c), respectively, the numerical predictions provide excellent agreement with the experimental results. The predicted OH conditional mass fraction curves follow the distribution of experimental datapoints, indicating that the chemistry and mixing interaction yield an accurate representation of the actual physical and chemical processes occurring. In general, the predictions of OH do not show a strong dependence on the rate of mixing. The profiles encompass approximately the same area of  $\eta$ -space and provide a similar magnitude in all of the examined cases. The most noticeable difference is the distribution of experimental data points, which is representative of the changing  $\tilde{\xi}$  and  $\tilde{\xi}''^2$  of the flow.

## Conditional Temperature

The conditional temperature is a calculated value that is highly dependent upon other scalars in the flow. Since conditional temperature is defined by the Eq. 5.1, it is highly dependent on species composition of the flow. In general, there are three major factors influencing the overall conditional temperature profile, as given by Eq. 3.11. The first factor is the level of mixing, as defined by the  $\langle \chi | \eta \rangle$ . The second major influence on the species production, and therefore temperature, is the convective term, largely dependent on the conditional velocity  $\langle u_i | \eta \rangle$ . The final major term is the diffusive term, which is dependent on the spatial gradient of the conditional species mass fraction,  $\langle Y_i | \eta \rangle$ . Depending on the influence of these terms, they can be expected to cause a change in the conditional temperature for a given mixture fraction while also shifting the location of the peak temperature due to the resulting changes in chemical reactivity.

The first location used for output of conditional temperature data is the L/8 position, shown in Fig. 6.14 a). At this axial position, it can be seen that there is a relatively large

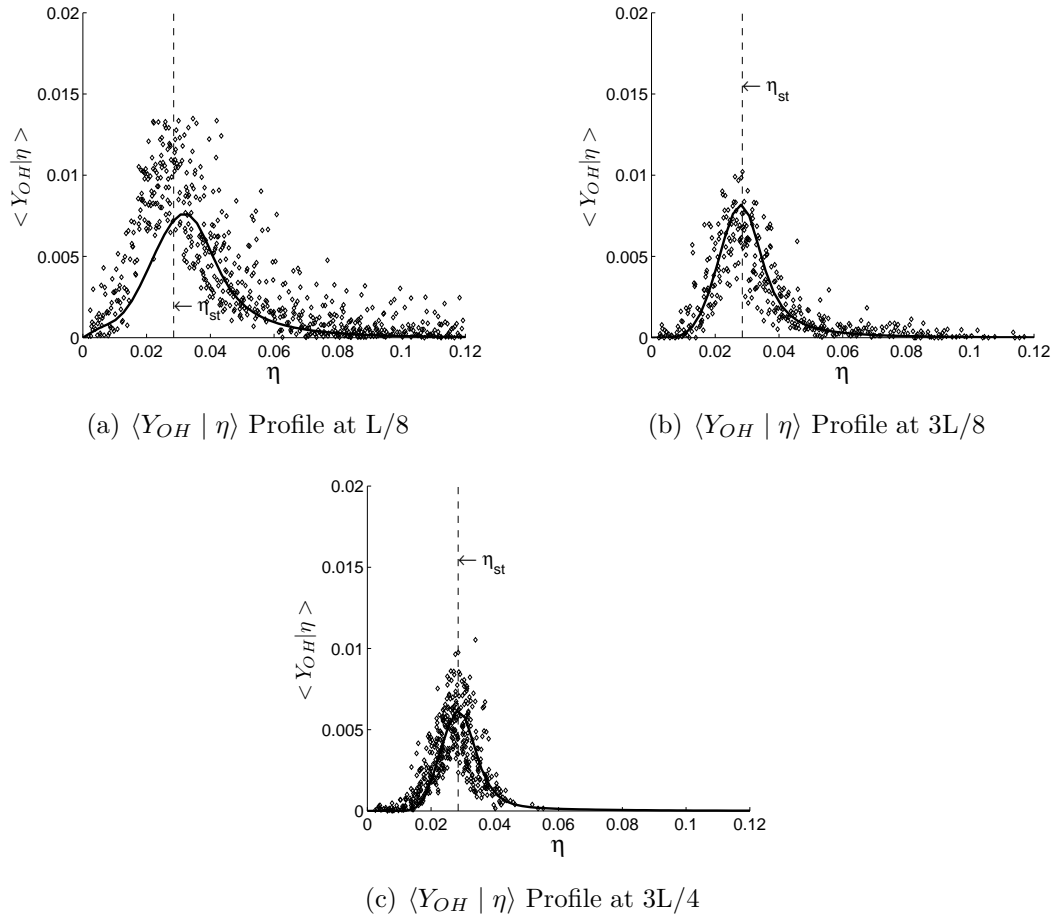


Figure 6.13:  $\langle Y_{OH} | \eta \rangle$  profiles at different axial locations, with the solid line representing numerical predictions and the diamond markers representing experimental data [40]

radial variation in the predicted conditional temperature of the mixture. The peak conditional temperatures are also similar to the peak Favre-averaged temperatures predictions shown in Fig. 6.9 and Fig. 6.8. This radial variation is likely caused by 2 major factors: the change in  $\langle \chi | \eta \rangle$ , as shown in Fig. 6.12 a), and the change in the convective term, due to changing velocity, as shown in Fig. 6.5 a). At this location, the  $r/d = 5$  and  $r/d = 10$  locations show the highest conditional temperatures, especially at lean mixture fraction values. This is likely due to the lower influence of the convective term, due to the locally small axial velocity, and corresponding increase in the importance of the diffusive term, which is driven by large mass fraction gradients. The  $\langle \chi | \eta \rangle$  at further radial locations is also significantly lower than near the centreline, leading to the higher temperature curve, especially for lean and stoichiometric mixtures. At the centreline, where there is a significant amount of mixing occurring, the conditional temperature peak occurs on the fuel rich side of stoichiometry, at approximately  $\tilde{\xi} \approx 0.04$ , where the increased chemical reactivity overcomes for the higher mixing and convection terms. The conditional temperatures remain fairly constant throughout the centre of the core, as seen through comparing the centreline and  $r/d = 2$  curves, which have similar mixing rates even though the local velocity is quickly changing. At the  $3L/8$  location, seen in Fig. 6.14 b), shows that there is a reduced cross-stream variation. The curves are essentially identical across the shown radial locations, with only a slight peak occurring at the  $r/d = 10$  location around stoichiometry. The two major differences in conditions at this location are the reduced velocity and lower  $\langle \chi | \eta \rangle$ . The combination of the reduced mixing and the reduction of heat conducted away from this location allows the mixture to obtain a higher overall temperature at and around stoichiometry than at the  $L/8$  location. At the location furthest downstream from the fuel inlet, shown in Fig. 6.14 c), the essentially uniform conditions present across the flow result in very little variation between the predicted conditional temperature profiles at the different radial locations. The reduced influence of the convective term and the small variation in mixing provide an effectively constant radial profile in conditional temperature. These conditions provide the highest conditional temperature curve. The peak conditional temperatures are observed at approximately stoichiometric mixture fraction, approaching a maximum of 2430K.

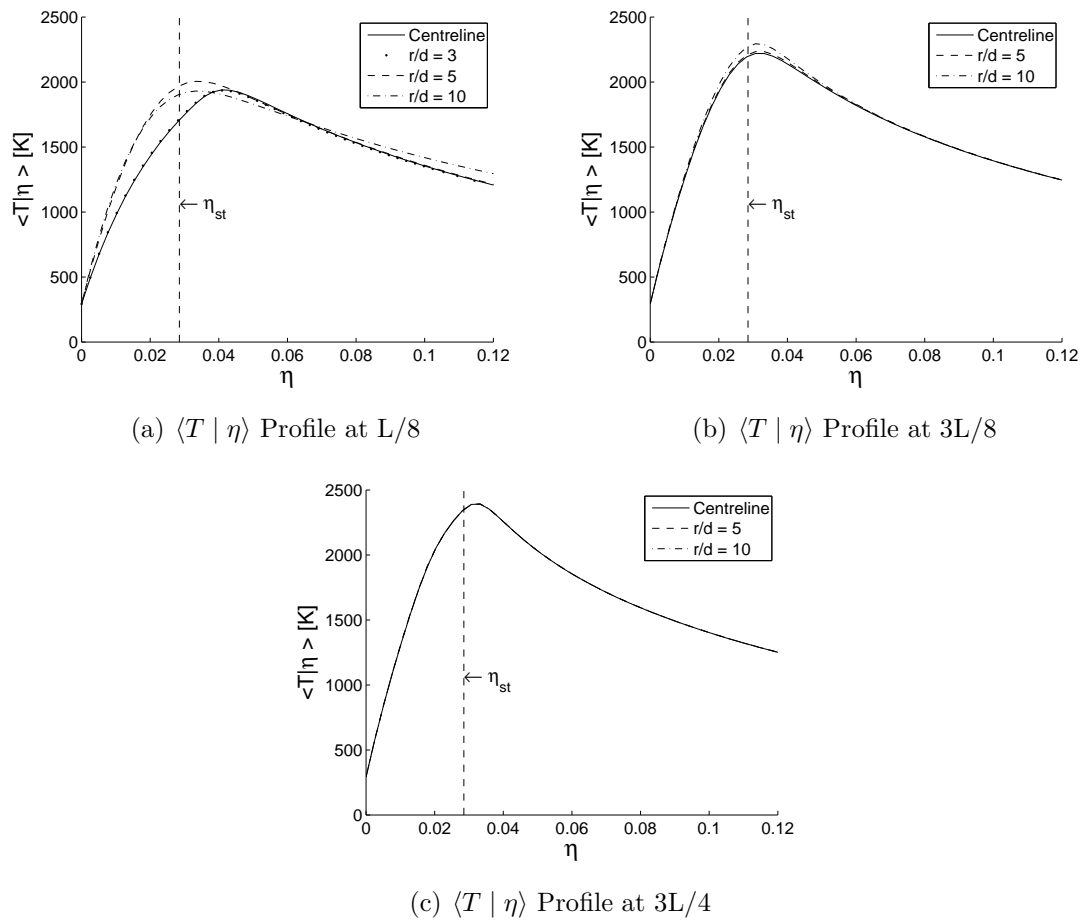


Figure 6.14:  $\langle T | \eta \rangle$  [K] profiles at multiple axial and radial locations

### 6.3.3 Discussion of Results

#### Conditional Results

Although the only available results from the experiment relate to the conditional  $OH$  mass fraction, it is shown that the chemistry and mixing model interaction provide excellent agreement with the measured results. The predicted values fall well within the experimental scatter, and the shape of the curve follows the distribution closely. Despite the excellent agreement generally seen, it is observed that the conditional  $OH$  mass fraction is underpredicted for fuel lean conditions in areas of very high mixing, notably at the L/8 location.

From analysis of the conditional scalar dissipation rate, it is apparent that there is an intense area of mixing forming near the shear layer of the jet. This area is seen to move outwards radially at an increased axial distance from the fuel inlet as the jet spreads and mixes with the coflow. This mixing area is observed to have an impact on the predicted conditional temperatures, reducing chemical activity and temperatures within areas of intense mixing. Areas with higher levels of mixing and large local velocities, especially within the mixing layer, are seen to have relatively low peak conditional temperatures, with the peak occurring on the fuel rich side of stoichiometry. The mechanism causing this is a combination of the intense mixing and the increased importance of the convective term in areas of high flow velocity, which remove enthalpy from the reacting parcel and distributing it or convect it towards less reactive areas. As  $\langle \chi | \eta \rangle$  decreases, the conditional temperatures are seen to peak closer to stoichiometry. When far downstream from the fuel inlet, the conditions across the flow are very similar, with the importance of the convective, diffusive and mixing terms all diminishing, resulting in little cross-stream variation in the conditional temperature profile. At this far downstream locations, the conditional temperatures are also seen to peak resulting from the nearly uniform flow. This reduced impact at locations far downstream from the inlet indicates that the conditional scalar dissipation rate has the largest affect on the flow at high values, while at low values, such as far downstream, the overall effect is dampened.

Once again, some comparison can be made between the experimental study by Barlow and Carter [40] and the numerical work by Barlow et al. [41]. Conditional  $OH$  mass fraction results show a general underprediction in comparison to experiments at all axial locations. Agreement with the conditional  $OH$  mass fraction tends to worsen with increasing

axial distance, which is in contrast to the current simulation, which shows an improvement with increasing axial distance. This difference in results may be attributed to the tuning of the flowfield and resulting mixing differences that arise from this modification. Conditional temperature values are slightly underpredicted at low axial distances, but show excellent agreement with the  $L/2$  and  $3L/4$  locations. Conditional scalar dissipation rate is not presented in either the numerical or experimental study, so no direct comparison of magnitude throughout the domain with the current results is possible.

## 6.4 Summary

The purpose of this chapter is to provide a validation test case of the computational code with a measured flow. It is seen that the code exhibits common characteristics of the  $k - \epsilon$  turbulence model, with predictions of  $\tilde{\xi}$  and  $\tilde{U}$  approximately 35% below the experimentally observed values. This result is not unexpected, as this performance is well documented when the  $k - \epsilon$  is applied to a round jet. Although various strategies have been employed to tune the model performance, this is not desired in the current study, as the autoigniting flow in the following chapter is significantly different than the current jet flow.

The temperature, velocity and mixture fraction fields are seen to follow expected trends: there is a large amount of momentum transfer and mixing occurring between the jet and the coflow, leading to the spreading of the jet and dispersion of the fuel. The predicted temperatures peak around the stoichiometric mixture fraction, which is typical of a jet flame. Peak temperatures are slightly underpredicted in comparison to measured results, which may be attributed to conditional scalar dissipation rate overpredictions as well as the effects of the  $k - \epsilon$  model.

The conditional  $OH$  mass fraction, temperature and scalar dissipation rate are presented at various locations in the flow. Numerical results are in excellent agreement for the  $OH$  mass fraction measurements at locations downstream of the  $L/8$  axial location. At the  $L/8$  location, the fuel rich predictions are in good agreement, however, in the fuel lean regime, the conditional mass fractions are underpredicted. The conditional temperature profiles are closely linked to the conditional scalar dissipation rate, convection and diffusion terms in the CMC equation, as seen in Eq. 3.11. In areas where the conditional scalar

dissipation rate is high, and the cross stream variation is large, it can be seen that there is a large impact on the conditional temperature peaks. At locations where the conditional scalar dissipation rate is low, there is very little cross stream variation in the conditional temperature profiles or magnitudes.

Overall, the computational code has demonstrated that it provides accurate temperature predictions while the calculated flowfield displays trends characteristic of the turbulence model used.

The following chapter uses the computational code to predict hydrogen autoignition predictions with two different mixing models. These results are analysed in detail and compared to various other studies of the same flow.

# Chapter 7

## Autoigniting Flame

The focus of this chapter is to provide an analysis of the performance of the current CMC code when used to predict autoignition in a transient flow. The steps taken to provide the required numerical setup of the simulation are outlined, including boundary conditions, grid selection and timestep selection. The results of the model are provided in terms of the ignition length prediction. Comparison between the AMC mixing model and the inhomogeneous model is also presented, including an analysis of the predictions of both models at different locations and times during the simulation. The performance of the inhomogeneous model is detailed, including a term-by-term analysis of the performance of the model.

### 7.1 Current Numerical Setup

In an effort to align the current work with previous numerical studies, the same set of conditions used by Jones and Navarro-Martinez [44], Jones et al. [45] and Patwardhan and Lakshmisha [43] is applied to the simulations. The fuel temperature is held at 750K for all simulations, the fuel and coflow velocities are maintained at 26m/s, and every effort is made to accurately represent the physical conditions present in the experimental work. Sections 7.2 to 7.5 outline the details used in setting up the numerical simulations used in this work, as well as some of the numerical difficulties encountered during the study.

## 7.2 Computational Domain and Boundary Conditions

To best represent the experimental apparatus, the computational domain is set up to have the same geometric configuration. Therefore, the computational domain is composed of an axisymmetric slice representing the central burner, the coflow inlet, the wall of the quartz tube and the flow outlet. The selection of inappropriate boundary conditions can potentially have a negative influence on the flow and quality of results, so each of the boundary conditions is chosen to best represent the actual flow condition.

Since the flow under consideration is confined within a quartz tube, the domain is selected to match the physical width of the experiment, while capturing the axial area of interest for autoignition results. That is, the computational domain has a radius of 12.5mm and a total length of 150mm.

The fuel and coflow inlets are placed along the base of the domain. The fuel inlet is located along the centreline, with the coflow inlet occupying the remaining area. The conditions at the fuel inlet provide a fuel velocity of 26m/s, and a fuel composition of  $Y_{H_2} = 0.13$  and  $Y_{N_2} = 0.87$ . The fuel temperature is held constant at 750K. The total width of the inlet matches the experimental diameter of 2.25mm. It is separated from the coflow by an adiabatic wall. The coflow boundary is modelled as an inlet of pure air,  $Y_{O_2} = 0.232$  and  $Y_{N_2} = 0.768$ , extending from a radial coordinate of 1.125mm (radius of fuel inlet) to the domain radius of 12.5mm. Depending on the scenario used for simulation, the coflow temperature is varied between 940K and 1080K, with the velocity held constant at 26m/s. The conditions across both the fuel and coflow inlets provide a uniform distribution of flow parameters, such as velocity, temperature, density, etc. Although the experimental turbulence intensity for the coflow is measured at approximately 13%, the turbulence intensity is set to 8% for the simulations due to numerical sensitivities in the mixing models, which is discussed further in Sec. 7.5.

The outer boundary, representing the surface of the quartz tube containing the flow is modelled as an adiabatic, no-slip wall. This boundary condition most closely represents the flow, as during the experiments the apparatus is allowed to run until the temperature loss throughout the domain is minimal. The no-slip boundary condition is representative of the surface of the quartz tube, as there is no surface velocity.

The outlet is placed along the entire top boundary of the domain. The outlet boundary forces a zero gradient condition on any flow parameter, i.e. pressure, velocity, temperature,

etc. Therefore, this boundary must be placed sufficiently far from the flow that this forced zero gradient does not impact the region of interest.

### 7.3 Timestep and Grid Refinement

As with the jet simulated in Ch. 6, selection of an appropriate computational grid is of large importance to the accuracy of simulation results. A grid that is unable to capture the spatial gradients and temporal changes with suitable accuracy will lead to error in the results. Therefore, refinements in the grid are required where these phenomena are expected to be at a maximum.

The major contrast between the autoigniting flow studied in the present chapter and the jet flame studied in Ch. 6 is the velocity field. While there is a large variation in velocity with the pure  $H_2$  jet flame studied in Ch. 6, the current flow has a nearly uniform velocity throughout the domain. Therefore, appropriate mesh refinements will be focused on capturing species gradients rather than significant velocity gradients. In addition, autoignition inherently involves transient flows, so the areas of large gradient will vary as the convection and diffusion within the domain affects the temporal flow patterns. With this knowledge, the mesh refinements are focused on the area around the axial centreline of the domain, restricted mainly to the area just downstream of the inlet where the largest species concentration gradients are expected. Experimental results are used as a guideline for appropriate refinement regions in order to best capture the chemical reactivity of the flows. The resultant mesh is refined until it is deemed that no further improvements in accuracy are made by further reduction of grid spacing.

The final mesh used in the current set of simulations contains 195 nodes in the axial direction and 29 nodes in the radial direction. The large difference between the number of axial and radial nodes is due to the large aspect ratio of the domain. As with the mesh used in Ch. 6, the mesh refinements near the inlet strive to obtain an aspect ratio of unity. The area of finest mesh spacing yields cells of 0.3mm x 0.3mm. The final computational grid is shown in Fig. 7.1.

As the accuracy of the CMC calculations are highly dependent on proper calculations within mixture fraction space, or  $\eta$ -space, selection of a proper mixture fraction mesh is also crucial. The simulations conducted in Ch. 6 are for the purpose of calculating a

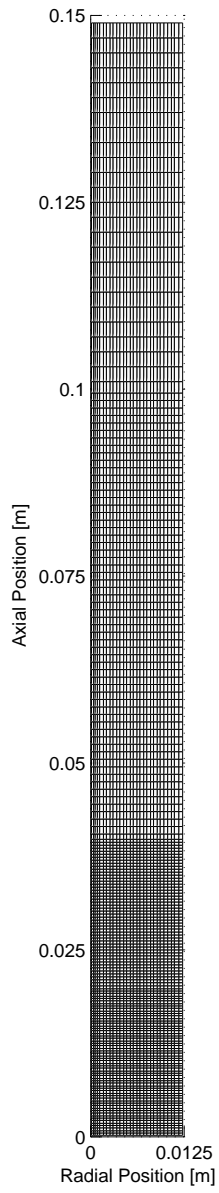


Figure 7.1: Final Autoignition Mesh

fully formed flame, with reactions occurring across large regions of  $\eta$ -space, and required a distribution of  $\eta$  points that captured this performance. The primary concern is capturing chemical reactivity in the vicinity of stoichiometry, so the highest grid density is in this region. Additionally, in the current study, several simulations are continued past the point of autoignition in order to evaluate the differences in mixing models, so it is important to retain sufficient grid spacing throughout  $\eta$ -space in order to capture all of the chemical kinetics present in the developed flame.

The final mixture fraction grid used for the autoignition simulations is shown in Fig. 7.2. This mesh consists of 80 nodes, with 60 nodes placed between 0 and  $\eta_{st}$ , which is highlighted in Fig. 7.3. Consistent with what is observed by Stanković [46], the most reactive mixture fraction,  $\eta_{mr}$ , occurs lean of stoichiometry in all cases. Therefore, refinements in the area between 0 and  $\eta_{st}$  will capture the region around  $\eta_{mr}$ . The remaining 20 nodes in  $\eta$ -space define the region between  $\eta_{st}$  and 1. The increased grid density for lean  $\eta$  values is used in order to properly capture the chemical interactions occurring around stoichiometry prior to autoignition.

In addition to ensuring spatial and mixture fraction grid independence, it must also be demonstrated that the simulation is not dependent on the chosen timestep. Adaptive timestepping is not used in the present code, so a user defined timestep must be applied to the simulation that provides sufficient resolution to capture the fast reaction rates and changes in species mass fraction during the autoignition process. Although the VODE solver uses an internal timestepping algorithm for solution of chemical interactions, the CFD/CMC timestep must also be sufficiently small to facilitate the accurate solution of the CMC equation. In the present study, a fixed timestep of  $1 \times 10^{-6}s$  is selected. Flowfield and CMC values are output from the code every 5 timesteps ( $5 \times 10^{-6}s$ ).

The spatial and mixture fraction grids, as well as simulation timestep, are tested and the present results are determined to be grid independent.

## 7.4 Simulation Conditions

In the current study, several different aspects of the simulation are studied. The first of these aspects is the effect of mixing constants on the flowfield. As was shown in Ch. 6, the velocity,  $\tilde{\xi}$  and  $\widetilde{\xi'^2}$  fields have a large impact on the CMC calculations. As the effects of

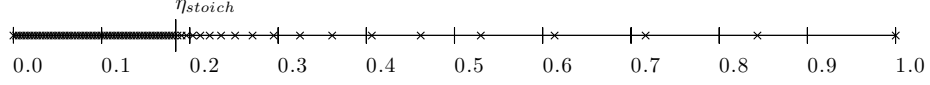


Figure 7.2: Full mixture fraction grid used for CMC autoignition calculations

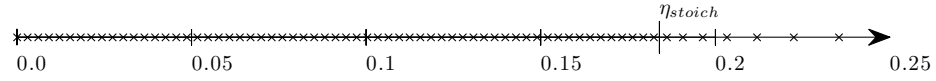


Figure 7.3: Partial mixture fraction grid between  $\eta = 0$  and  $\eta = 0.25$  used for CMC autoignition calculations in steady state validation case

the  $k - \epsilon$  model have not been studied in the current flow to the same extent as with the jet flow in Ch. 6, it is not known what combination of turbulence constants will provide the most accurate flow simulation. As an initial step into the analysis of the effects of these parameters on the the flowfield, three sets of parameters are tested. These parameters are summarised in Table 7.1. The first case is undertaken to ascertain a baseline

Table 7.1: Sets of turbulence and mixing parameters used in autoignition simulations

Parameter Case	$C_{\epsilon_1}$	$Sc_t$
Case 1 - Standard Constants	1.44	0.7
Case 2 - Modified $C_{\epsilon_1}$	0.40	0.7
Case 3 - Modified $Sc_t$	1.44	0.5

level of performance with the standard turbulence and mixing constants. This is taken as the base level of performance and used to compare the effects of the modification of any other constants. Reduction of the turbulent Schmidt number,  $Sc_t$ , for Case 2 follows the study of Patwardhan and Lakshmisha [43], where in addition to the modification of  $Sc_t$ ,

modification of  $C_{\epsilon_1}$  and  $C_\chi$  is also undertaken in the same case [43]. Reduction of the value of  $Sc_t$  also follows the method of Markides et al. [68] in a study of a similar flow using *n*-heptane as a fuel instead of a mixture of  $H_2 - N_2$ . Case 3 is undertaken to isolate the effect of  $C_{\epsilon_1}$  modification in relation to the flowfield. The relatively large change of  $C_{\epsilon_1}$ , from the standard 1.44 to a modified 0.4, is chosen to provide an estimate of the magnitude of the changes relative to the magnitude of the change in the constant. Each of these 3 cases is run under steady state conditions to evaluate the flowfield.

Following the characterisation of the flowfield, each of the 3 cases in Table 7.1 is used to simulate autoignition at 7 different coflow temperatures using the AMC model. The range of coflow temperatures used is 940K, 950K, 960K, 980K, 1000K, 1020K and 1080K.

After the autoignition simulations are carried out using the AMC model, investigation of the inhomogeneous mixing model is undertaken. This involves a set of simulations following the standard constants used in Case 1 with each of the coflow temperatures. The impacts of the different mixing model are evaluated in comparison to those seen with the AMC model.

As a final metric for comparison between the two models, the AMC model and inhomogeneous model are each used to simulate a steady flame under identical conditions, both with the Case 1 constants. This comparison allows analysis of the effect of the mixing model on flame structure and species production.

## 7.5 Numerical Difficulties

During testing of the inhomogeneous model implementation, it was found that the  $\langle \chi | \eta \rangle$  predictions are particularly sensitive to the flow variance. If the values of  $\widetilde{\xi''^2}$  become too large, the profiles of  $\tilde{I}_1$  and  $\tilde{I}_2$  in Eq. 3.55 become discontinuous, subsequently resulting in a discontinuous  $\langle \chi | \eta \rangle$  profile. Several techniques to correct this were attempted, including applying a scaling factor to the final profile to match known boundary conditions; however, none of these produced satisfactory performance that matched the results provided by Devaud et al. [3]. Instead, it was found that reducing the turbulence intensity of the simulations provided the requisite reduction in variance to make the model perform properly, requiring no further numerical correction. It is thought that this was not seen in previous testing in [11, 3, 39] due to the formulation of the flow, which typically resulted

in a smaller magnitude  $\widetilde{\xi''^2}$  field. In general, this discontinuity is avoided if the magnitude of  $\widetilde{\xi''^2}$  is kept below approximately  $0.1\widetilde{\xi}$ .

## 7.6 AMC Model Results

### 7.6.1 Effects of Turbulence and Mixing Constants on Steady Flowfield

For each of the 3 cases given in Table 7.1, a steady state fully burning CMC simulation with  $T_{coflow} = 980K$  is run such that velocity and mass residuals converge below  $1.0 \times 10^{-4}$ . The flowfield in each of the 3 cases is examined primarily to determine the  $\widetilde{\xi}$  and  $\widetilde{\xi''^2}$  distribution within the flow. No analysis of the velocity field is provided, as the flow is largely absent of shear and velocity gradients, especially when compared to the jet flow in Ch. 6.

As there are no measurements made on the steady flowfield during experimentation [47], the analysis of steady conditions is undertaken only to evaluate relative changes in the model, and not the absolute accuracy of the predictions.

### 7.6.2 Mean Mixture Fraction

The prediction of the mean mixture fraction field,  $\widetilde{\xi}$ , is of extreme importance to the prediction of autoignition. Parameters that affect the distribution of fuel within the flowfield must be well understood, as modification may lead to a resultant spatial shift in the occurrence of conditions that support or preclude autoignition. The areas in the domain containing fuel at a lean mixture fraction are critical for predicting autoignition properties, as the peak chemical activity during autoignition occurs lean of  $\eta_{st}$  [46].

The centreline  $\widetilde{\xi}$  distribution, as shown in Fig. 7.4, shows the distribution resulting from the 3 different cases. With the mixing constants in Case 1, it can be seen that a significantly higher mean mixture fraction is predicted in comparison to the other tested cases. The constants for Case 2 and Case 3 yield very similar curves to each other, with a significantly lower prediction in values than Case 1, especially in the region between  $x/d$

= 5 and  $x/d = 15$ . The difference in values indicates that a higher level of mixing is seen along the centreline in Case 2 and Case 3.

Examining several radial profiles in Fig. 7.5, located at  $x/d = 5$ ,  $x/d = 10$  and  $x/d = 15$ , it can be seen that Case 1 does indeed predict a higher  $\tilde{\xi}$  near the centreline of the domain. The  $\tilde{\xi}$  fields are similar to each other for Case 2 and Case 3, with any difference in the curves reducing with an increase in radial position. The constants used in Case 2, with  $C_{\epsilon_1} = 0.40$ , do consistently provide values slightly closer to the Case 1 predictions than does Case 3. Case 2 predictions range from a 20% underprediction compared to Case 1 at an axial location of 5d, increasing to a 40% underprediction at an axial location of 15d. Case 3 predictions range from a 25% underprediction compared to Case 1 at an axial location of 5d, increasing to a 50% underprediction at an axial location of 15d. Therefore, for a 72% reduction of  $C_{\epsilon_1}$  in Case 2, the difference in centreline  $\tilde{\xi}$  ranges from approximately 20-40% in the axial region investigated, while for a 29% reduction in the value of  $S_{C_t}$ , a reduction of approximately 25-50% is observed for this same region. This indicates that the predictions of  $\tilde{\xi}$  are more sensitive to modification of  $S_{C_t}$  than modification of  $C_{\epsilon_1}$ .

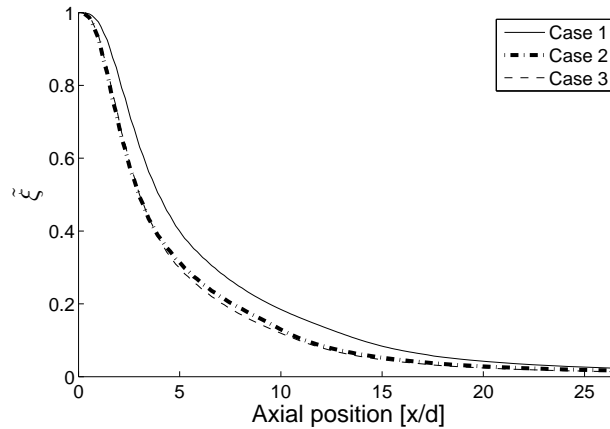


Figure 7.4: Centreline  $\tilde{\xi}$  profile

### 7.6.3 Mean Mixture Fraction Variance

The centreline  $\tilde{\xi}''^2$  distribution, Fig. 7.6, shows much larger differences between cases than was seen with  $\tilde{\xi}$  in Fig. 7.4. At the early stages of mixing, i.e. near the fuel inlet, between

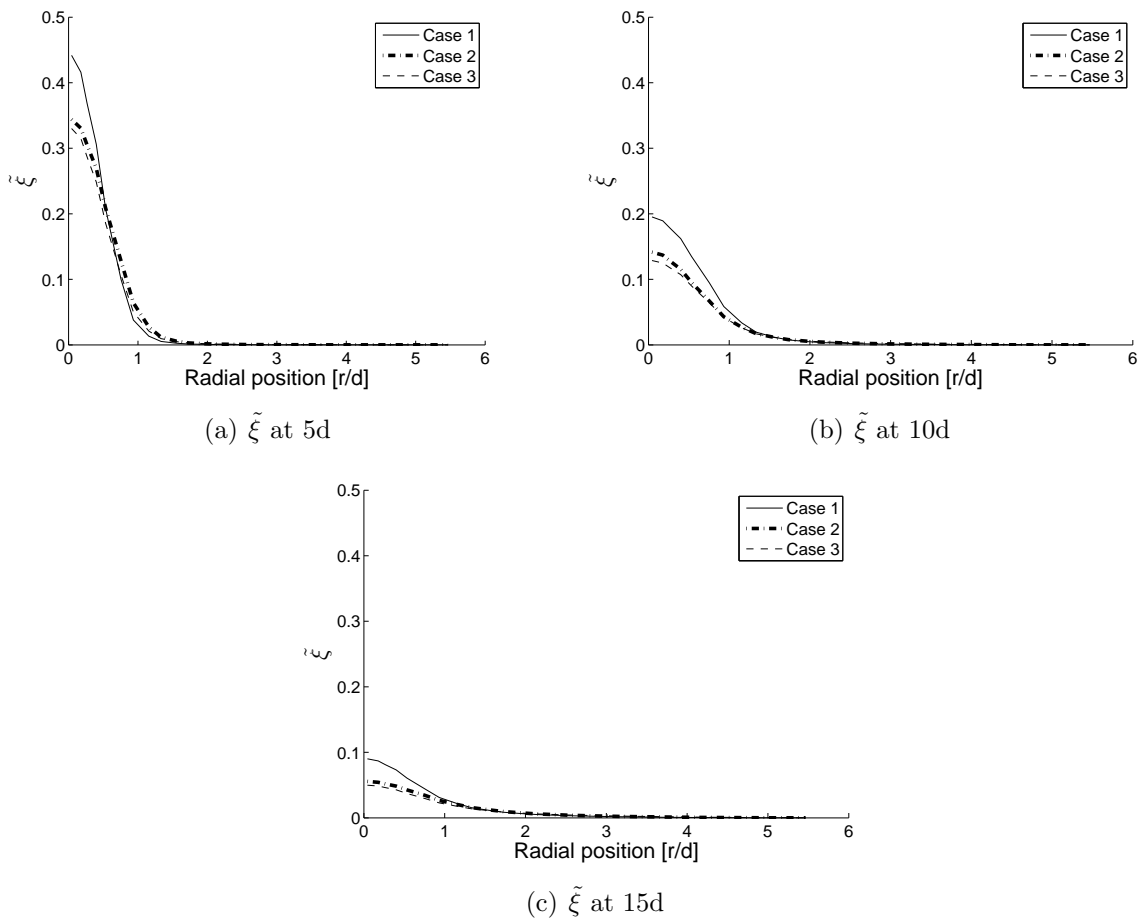


Figure 7.5:  $\tilde{\xi}$  Radial profiles at different locations

$x/d = 0$  and  $x/d = 3$ , Case 1 exhibits the lowest variance. In comparison, Case 2 and Case 3 predict a larger variance value in this region near the inlet. This large variance indicates that this is a very strong region of mixing, and this mixing corresponds to the large gradient seen in mixture fraction near the inlet seen in Case 2 and Case 3, shown in Fig. 7.4. Further from the inlet, shown between approximately  $x/d = 3$  and  $x/d = 7$ , a significantly stronger peak in variance is seen for the constants in Case 2, with an increase of approximately 30% in comparison to the peak Case 1 baseline results. The variance values in Case 3, although larger than the values of Case 1 prior to  $x/d = 3$ , show an early peak and drop off, falling below the predictions of the standard constants of Case 1. The peak  $\widetilde{\xi''^2}$  values seen in Case 3 are approximately 27% lower than the peak predicted by Case 1. This pattern indicates that although both Case 2 and 3 show strong initial mixing, the effects of the change in  $Sc_t$  with Case 3 are greatest near the inlet, and then decrease throughout the remainder of the domain, while modifications of  $C_{e1}$  have an effect throughout the majority of the domain.

Further comparison of  $\widetilde{\xi''^2}$  between the 3 cases is performed by analysis of radial profiles. In Fig. 7.7 a), the radial  $\widetilde{\xi''^2}$  field at the  $x/d = 5$  axial location is seen. At this location, the profiles between Case 1 and Case 2 are very similar, as indicated in Fig. 7.6. Case 3 yields a much lower  $\widetilde{\xi''^2}$  value near the centreline; however, beyond the  $r/d = 1.5$  radial location, the 3 curves become quite similar in magnitude to each other. At the  $x/d = 10$  location, shown in Fig. 7.7 b), it can be seen that the difference between Case 1 and Case 2 is increasing near the centreline, while Case 3 predicts the lowest variance once again. This is representative of the trends seen in Fig. 7.6 at the  $x/d = 10$  axial location, where the Case 1 and Case 2 predictions begin to diverge slightly. The curves begin to converge as the radial distance from the centreline increases, however at this axial location, it does not happen until approximately the  $r/d = 2$  position. At the  $x/d = 15$  location, Fig. 7.7 c), much the same trends are seen as at the  $x/d = 10$  location, however the magnitude of the variance has decreased noticeably. The convergence between radial profiles occurs after the  $r/d = 3$  position, indicating that the effects of mixing constants is spreading throughout the domain radially with the fuel. It is also observed that the difference between the predictions tends to be largest near the centreline, while differences tend to become smaller as the radial distance from the centreline is increased.

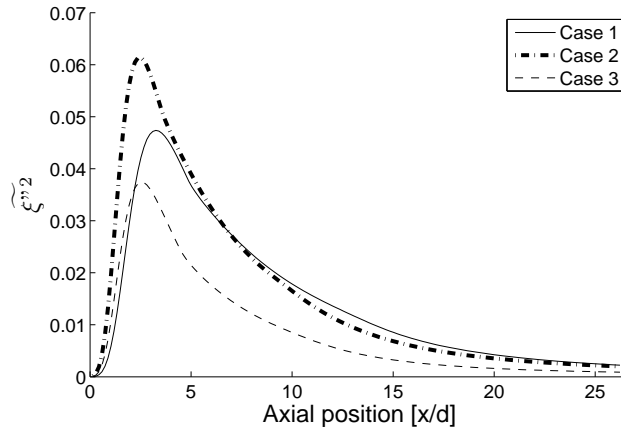


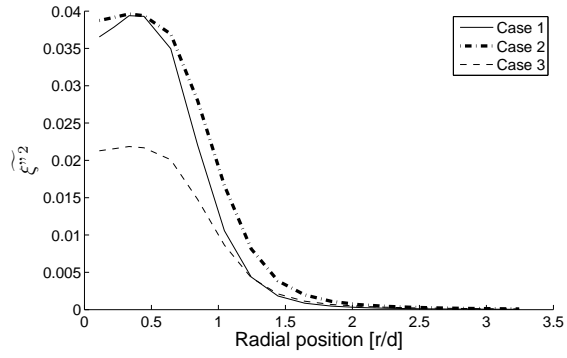
Figure 7.6: Centreline  $\xi''^2$  profile

#### 7.6.4 Predictions of Ignition Length

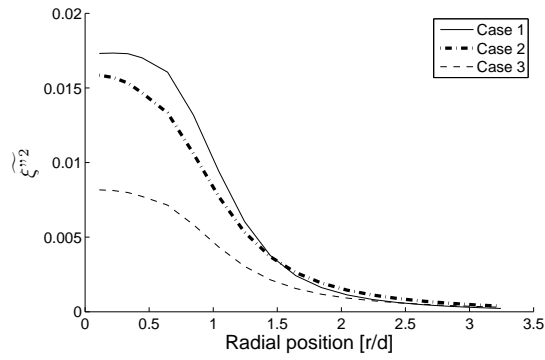
The autoignition simulations conducted in the present study are divided into two major parts. The first part, which employs the AMC mixing model, provides a characterisation of the effects of temperature and mixing constants on the autoignition conditions. As a result, for each of the 3 cases in Table 7.1, 7 different coflow temperatures are simulated. The resulting 21 simulations provide a characterisation of the effects of turbulence parameters on the autoignition event, as well as a baseline for expected flow and mixing conditions which support autoignition. The second part provides an investigation into the effects of mixing model selection. This is conducted via implementation of the inhomogeneous mixing model with the mixing constants used in Case 1. The second part of this study is presented in Sec. 7.7.

The autoignition length or delay is a metric used in assessing the time it takes for a fuel in an unmixed state to mix with the oxidiser and reach the specified ignition criteria, which, in this study, is a 1% increase in Favre-averaged temperature. The autoignition length is highly dependent on the predictions of the mixture fraction and mixing fields, so varying constants which affect the development of these fields can affect the autoignition predictions.

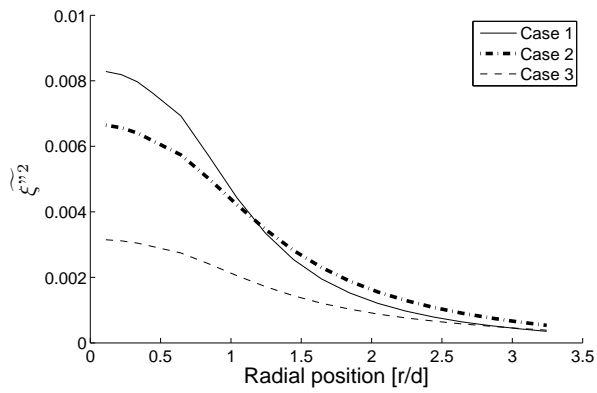
A summary of autoignition results is presented in Table 7.2 for the AMC model. Table 7.2 includes the autoignition length at which the autoignition criterion is met,  $L_{ign}$ , the mean mixture fraction at the location of autoignition,  $\tilde{\xi}_{mr}$ , the conditional scalar dissipa-



(a) 5d



(b) 10d



(c) 15d

Figure 7.7:  $\xi''^2$  Radial profiles at different locations

tion rate at the most reactive mean mixture fraction,  $\langle \chi \mid \eta = \tilde{\xi}_{mr} \rangle$ , and the reference time at which ignition occurs relative to the start of the simulation,  $\tau_{ign}$ . For the purposes of this analysis, the most reactive mixture fraction is taken as the mean mixture fraction value at which ignition occurs.

In Fig. 7.8, results from the simulations undertaken in both the first and second parts of the study are summarised with the experimental measurements. At almost all temperatures, the largest  $L_{ign}$  is predicted by Case 2. Case 1 provides intermediate predictions, while Case 3 constants yield the shortest ignition lengths, correlating with the lowest  $\tilde{\xi}''^2$  predictions. At high temperatures, the difference between the cases is reduced, and all cases predict essentially the same value of  $L_{ign}$ . For each of the different cases presented with the AMC model, the length predictions do not cross over each other. The reduction of  $L_{ign}$  with increasing  $T_{coflow}$ , and a corresponding reduction in the sensitivity to the selection of model constants indicates an increasing importance of the chemical source term in the CMC equation. The effects of the mixing fields have less of an impact on ignition predictions in this high temperature region.

The results for the AMC model indicate a general underprediction of the experimental ignition length. Although there are only 5 data points available for comparison, the slope in the experimental results indicates a strong correlation between  $T_{coflow}$  and  $L_{ign}$ .

Following the presentation method of Stanković [46], as a method of comparison, the experimental results are shifted by 10K to the left in Fig. 7.9. The choice of a 10K shift corresponds with the stated experimental error, which is approximately 1% [42]. With this shift, it is found that the numerical results from the present study provide much better agreement with the experimental results, with only slight underpredictions. Using the results from the Case 1 baseline, prior to the 10K shift in experimental results, with  $T_{coflow} = 950K$ , there is an underprediction of approximately 44%, and at  $T_{coflow} = 960K$ , the underprediction is approximately 41%. Following the 10K shift, at  $T_{coflow} = 940K$  there is an underprediction of approximately 17%, while with  $T_{coflow} = 950K$  there is an underprediction of approximately a 19%. The slope followed with the experimental results is closely matched, indicating that the trends seen numerically are a good representation of the actual physical processes occurring.

Although the predicted values of  $L_{ign}$  stay within approximately 5% for all simulations using the AMC model, the effects of mixing constants is more clearly seen through analysis of  $\tilde{\xi}_{mr}$  in Fig. 7.10. In general, all of the cases tested show a tendency for  $\tilde{\xi}_{mr}$  to

Table 7.2: Autoignition results with AMC mixing model

Temperature [K]	$L_{ign}$ [m]	$\xi_{mr}$	$\langle \chi   \eta = \tilde{\xi}_{mr} \rangle [s^{-1}]$
Case 1	Standard $k - \epsilon$ ,	$Sc_t = 0.7$	
1080	0.0038	0.0665	73.8
1020	0.0075	0.0661	43.1
1000	0.0102	0.0524	23.0
980	0.0142	0.0534	14.9
960	0.0224	0.0491	6.9
950	0.0304	0.0455	4.3
940	0.0455	0.0310	1.9
Case 2	$C_{\epsilon_1} = 0.40$ ,	$Sc_t = 0.7$	
1080	0.0042	0.0649	105.0
1020	0.0078	0.0658	58.5
1000	0.00108	0.0624	35.8
980	0.0155	0.0635	21.4
960	0.0248	0.0629	10.4
950	0.0320	0.0484	5.5
940	0.0465	0.0298	1.9
Case 3	Standard $k - \epsilon$ ,	$Sc_t = 0.5$	
1080	0.0042	0.0405	32.7
1020	0.0075	0.0447	21.8
1000	0.0098	0.0500	17.8
980	0.0135	0.0500	11.1
960	0.0212	0.0405	4.4
950	0.0292	0.0383	2.7
940	0.0435	0.0217	0.9

Table 7.3: Autoignition results with inhomogeneous mixing model

Temperature [K]	$L_{ign}$ [m]	$\xi_{mr}$	$\langle \chi   \eta = \tilde{\xi}_{mr} \rangle [s^{-1}]$
Case 1	Standard $k - \epsilon$ ,	$Sc_t = 0.7$	
1080	0.0038	0.0500	20.8
1020	0.0068	0.0542	16.8
1000	0.0092	0.0414	12.9
980	0.0125	0.0474	8.0
960	0.0196	0.0449	3.9
950	0.0268	0.0335	2.7
940	0.0338	0.0303	1.6

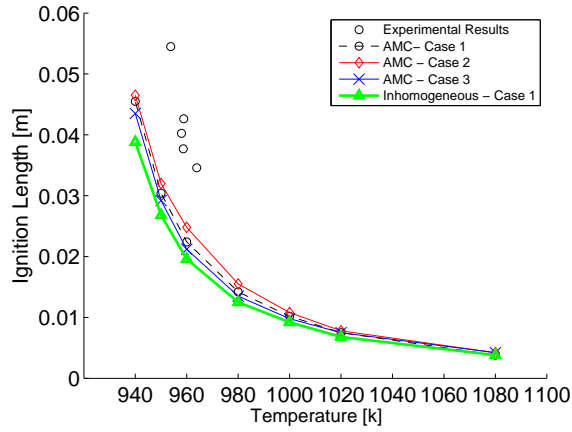


Figure 7.8: Ignition length comparison for AMC and Inhomogeneous mixing model with different mixing constants

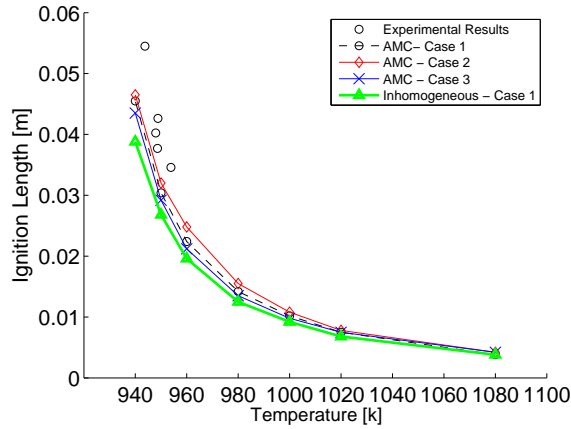


Figure 7.9: Ignition length comparison for AMC and Inhomogeneous mixing model with different mixing constants, experimental results shifted by -10K

decrease with decreasing temperatures, especially as the "no ignition" experimental region is approached. This decrease at low temperatures, which matches what is seen experimentally as the ignition limit, may be an indication of the chemical mechanism favouring lean mixture fractions for improved ignition kinetics. At higher temperatures, specifically at or above  $T_{coflow} = 1000K$ , the value of  $\xi_{mr}$  becomes less sensitive to the coflow temperature. This closely follows the findings of Stanković [46], indicating that the region of peak chemical activity does not have a strong temperature dependence in the higher temperature region. This is indication that the chemical source term in the CMC equation is the most dominant term, with the spatial and mixing terms having little influence on the results.

The effect of mixing constant selection is also seen in Fig. 7.10 and Fig. 7.11. The highest values of  $\tilde{\xi}_{mr}$  and  $\langle \chi | \eta = \tilde{\xi}_{mr} \rangle$  are seen for the Case 2 constants with the AMC mixing model throughout the majority of the temperature range. As this corresponds to the highest  $\tilde{\xi}''^2$  seen in Fig. 7.6, it follows that an increase in  $\tilde{\xi}''^2$ , and therefore  $\tilde{\chi}$ , favours a higher  $\tilde{\xi}_{mr}$  at the time of ignition. The Case 1 baseline provided the next highest predictions of  $\tilde{\xi}_{mr}$  and  $\langle \chi | \eta = \tilde{\xi}_{mr} \rangle$ , with Case 3 providing the lowest predictions. This corresponds to the magnitude of centreline  $\tilde{\xi}''^2$  for each of Case 2 and Case 3.

As a general trend, it can be observed that as  $T_{coflow}$  decreases, the values of  $\xi_{mr}$  and  $\langle \chi | \eta = \tilde{\xi}_{mr} \rangle$  decrease sharply. Although there was no instance in which ignition was not observed to occur, the sharp downward trends with decreasing temperature indicate that the "no ignition" boundary is not likely far below the minimum value of  $T_{coflow} = 940K$

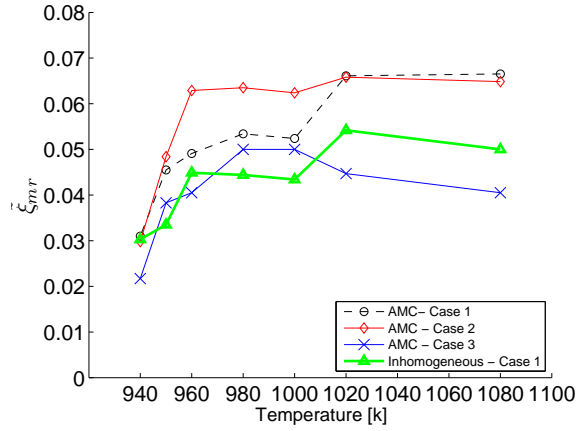


Figure 7.10:  $\tilde{\xi}_{mr}$  comparison for AMC and Inhomogeneous mixing model with different mixing constants

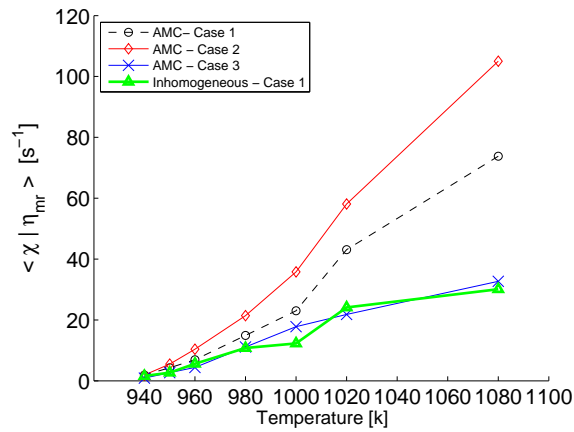


Figure 7.11:  $\langle \chi | \eta = \tilde{\xi}_{mr} \rangle$  comparison for AMC and Inhomogeneous mixing model with different mixing constants

used in the simulations. These trends are explained by the dependence of the chemical source term,  $\dot{\omega}$ , on  $T_{coflow}$ . At low temperatures,  $\dot{\omega}$  is a smaller magnitude and is in competition with the effects of mixing, convection and diffusion. Therefore the timescales associated with ignition are larger and of a similar order to the mixing timescales, meaning that the predictions of  $\langle \chi | \eta \rangle$  have a larger influence on  $L_{ign}$ . At high temperatures,  $\dot{\omega}$  dominates the CMC equation, and the associated timescales with the ignition process decrease. As a result, the ignition predictions become less dependent on the mixing field due to the magnitude of  $\dot{\omega}$ . This is exemplified by the spread of  $L_{ign}$  predictions at low temperatures, which range approximately 3mm from largest to smallest, while at higher temperatures, the spread is reduced to approximately 0.5mm.

## 7.7 Comparison of Mixing Models

This section provides a detailed comparison between the results obtained with both the AMC and inhomogeneous mixing models. The predictions of ignition length of the inhomogeneous model are presented in relation to the AMC model. Conditional values are provided for both models at 3 different  $T_{coflow}$ , 1080K, 980K and 950K. Included is an analysis of the temporal evolution of the conditional scalar dissipation rate, the conditional species mass fractions and conditional temperature. The steady flame predictions of each model are also compared.

### 7.7.1 Predictions of Ignition Length

As it is shown in Sec. 7.6.4, the choice of turbulence constants only leads to a difference of approximately 5% in the predictions of ignition length when using the AMC mixing model. Upon simulation with the inhomogeneous mixing model, the ignition length is seen to decrease throughout the domain, especially at lower  $T_{coflow}$ , as shown in Fig. 7.8. The  $L_{ign}$  results from the inhomogeneous model stay within approximately 15% of Case 1 constants with the AMC model for the range of coflow temperatures tested. It is seen that the difference between mixing model predictions is at the largest for low  $T_{coflow}$ . This

is explained by the temperature dependence of the chemistry, i.e. as  $T_{coflow}$  increases, the magnitude of the chemical source term increases to the point that ignition is not largely dependent on the predictions of mixing intensity.

The flow conditions at which ignition occurs are seen to be slightly different depending on the mixing model chosen. In Fig. 7.10, Case 1 constants for the AMC model and the inhomogeneous model display similar trends, while the predicted values of  $\tilde{\xi}_{mr}$  for the inhomogeneous model remain slightly lower in magnitude. The temperature dependence at low  $T_{coflow}$  is again demonstrated, with a sharp increase in the value of  $\tilde{\xi}_{mr}$  as temperature increases, while at higher temperatures this dependence is not seen. The same mechanism responsible for this trend with the AMC model is also responsible for the predictions of the inhomogeneous model: as the temperature increases, the rate of reaction increases, seen with a larger chemical source term in the CMC equation, and the ignition process is controlled less by mixing and more by time available for reaction to occur, resulting in similar values regardless of the model and constants chosen.

## 7.7.2 Conditional Scalar Dissipation Rate Temporal Evolution

This analysis examines three different coflow temperatures for the AMC and inhomogeneous mixing model, both using the Case 1 mixing constants. The coflow temperatures used for analysis are 1080K, 980K and 950K.

Since the flowfields of both the AMC model and inhomogeneous model are identical up to the point of ignition, any differences in the ignition predictions from the CMC equation, Eq. 3.11 are due to the evolution of  $\langle \chi | \eta \rangle$ . By its nature, the AMC model provides regular distributions of  $\langle \chi | \eta \rangle$ , according to Eq. 3.47. The shape of the inhomogeneous model is not constant in  $\eta$ -space, but rather is dependent on multiple scalars and vectors, as defined in Eq. 3.54. This varying influence of the flowfield allows the shape of the  $\langle \chi | \eta \rangle$  to vary with time and location.

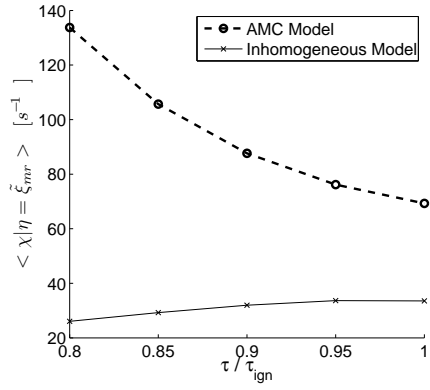
The first basis of comparison of the two models is performed with  $T_{coflow} = 1080K$ . In Fig. 7.12 a), a temporal evolution of  $\langle \chi | \eta = \xi_{mr} \rangle$  is shown for the different mixing models. It is immediately apparent that the choice of model provides a large difference in the  $\langle \chi | \eta = \xi_{mr} \rangle$  evolution. At times leading up to ignition, the AMC model is seen to predict a large spike in values, while the inhomogeneous model predicts a steady increase.

It can also be seen that there is a large gap in the predictions of  $\langle \chi | \eta = \xi_{mr} \rangle$  at  $\tau_{ign}$ . The high coflow temperatures involved in this simulation therefore allow for a large range of  $\langle \chi | \eta = \xi_{mr} \rangle$  and  $\tilde{\xi}$  for which ignition is possible.

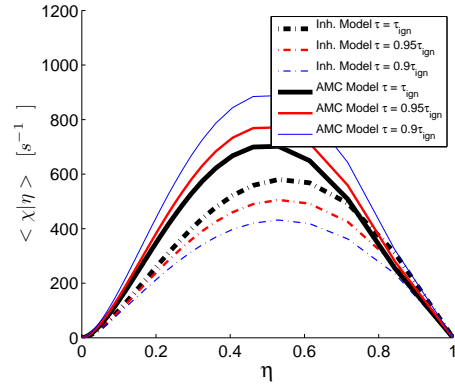
In Fig. 7.12 b) and c), the respective curves for  $\langle \chi | \eta \rangle$  at different times show opposing trends for the two models. The overall magnitude of the AMC curve is seen to decrease as  $\tau_{ign}$  is approached, while the overall magnitude of the inhomogeneous model is seen to increase as  $\tau_{ign}$  is approached. Despite the contrasting predictions, the value of  $\tilde{\chi}$  does indeed increase with time at  $L_{ign}$  for both models. The cause of this difference in predictions is largely due to the position and shape of the PDF. As  $\tilde{\chi}$  is given by  $\int_0^1 P(\eta) \langle \chi | \eta \rangle d\eta$ , the subsequent shift in the distribution of the PDF changes the main  $\eta$  region of influence on the  $\langle \chi | \eta \rangle$  curve. With the AMC model, this shift leads to a net decrease of the magnitude of the curve, while providing an increase in  $\tilde{\chi}$ . The inhomogeneous model demonstrates the opposite trend, where the change of the PDF relative to the change in the  $\langle \chi | \eta \rangle$  profile leads to a net increase in magnitude of the curve.

The shape of the  $\langle \chi | \eta \rangle$  curves provided by both mixing models are similar in shape; however, some differences may be seen by examining Fig. 7.12 b) and c). Both models predict what is approximately a bell shaped distribution, however, the peak for the inhomogeneous model is predicted slightly rich of  $\eta = 0.5$ , yielding an asymmetric profile. In the area lean of  $\eta = 0.05$ , the inhomogeneous model provides only small changes in  $\langle \chi | \eta \rangle$  values as time progresses. This lack of temporal change of the curve indicates that the mixing is only weakly dependent on time in this region with the inhomogeneous model. Conversely, with the AMC model, the magnitude of  $\langle \chi | \eta \rangle$  in this region decreases proportional to the peak value on the curve, as its shape is defined by a single function. Therefore, the AMC model indicates that the mixing is indeed a strong function of time. In the portion of the curve rich of  $\eta \approx 0.9$ , the predictions begin to overlap between the two models, with the inhomogeneous model predicting higher levels of mixing in this region despite the rest of the curve being lower. As time progresses, the molecular mixing in this region increases. Despite this change in mixing trends predicted at large  $\eta$ , the influence of this region on the Favre-averaged values is minimal, as the probability in this area of the curve is essentially zero.

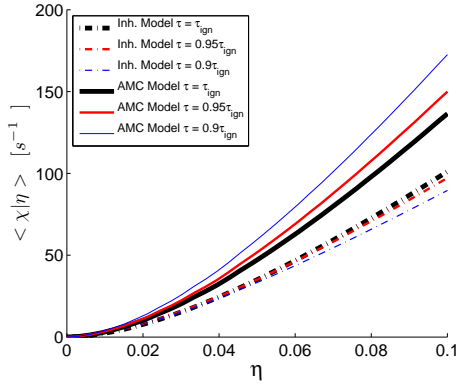
The second temperature examined is  $T_{coflow} = 980K$ . At this temperature, the predictions of  $\langle \chi | \eta = \xi_{mr} \rangle$  in Fig. 7.13 a) closely follow the trends outlined previously in Fig. 7.12 a). The AMC model shows a large peak, then a fast decline as ignition is approached,



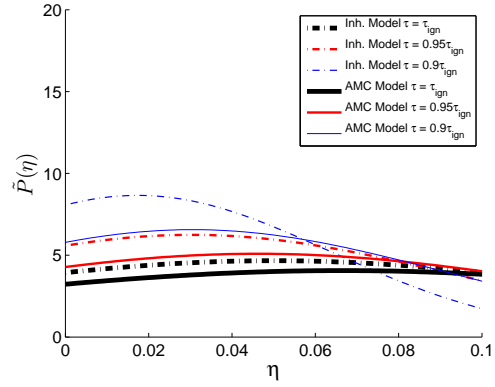
(a)  $\langle \chi | \eta = \xi_{mr} \rangle$  temporal evolution



(b)  $\langle \chi | \eta \rangle$  temporal evolution

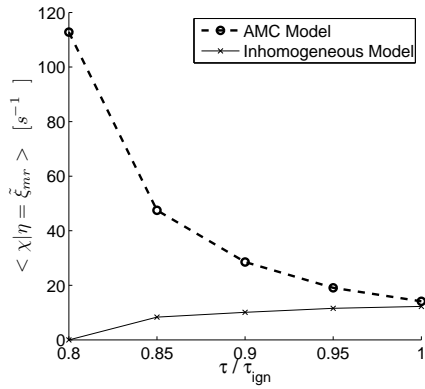


(c)  $\langle \chi | \eta \rangle$  temporal evolution,  $0 \le \eta \le 0.1$

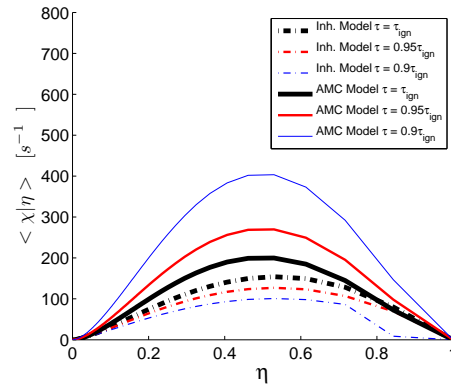


(d)  $P(\eta)$  temporal evolution,  $0 \le \eta \le 0.1$

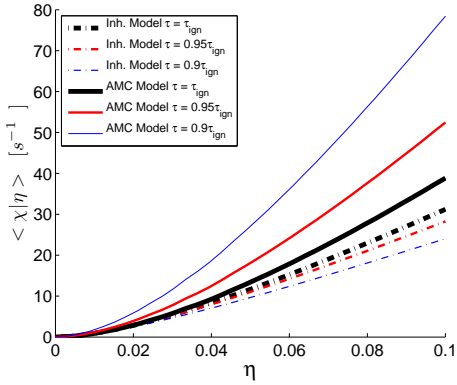
Figure 7.12:  $\langle \chi | \eta \rangle$  and PDF evolution at  $L_{ign}$  for  $T_{coflow} = 1080K$



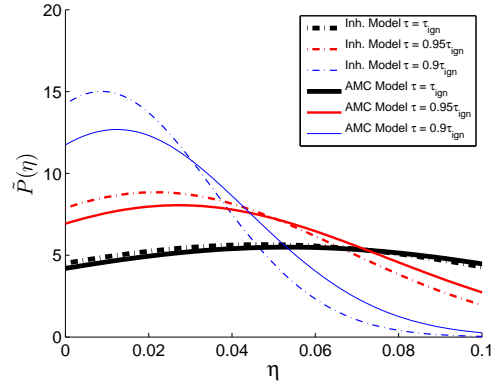
(a)  $\langle \chi | \eta = \xi_{mr} \rangle$  temporal evolution



(b)  $\langle \chi | \eta \rangle$  temporal evolution



(c)  $\langle \chi | \eta \rangle$  temporal evolution,  $0 \le \eta \le 0.1$

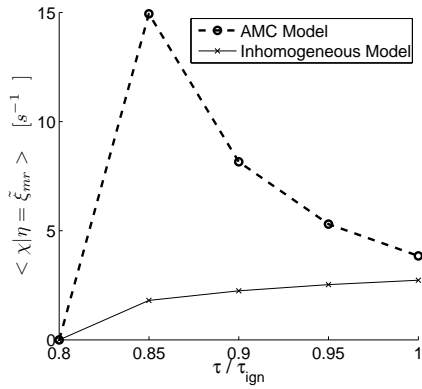


(d)  $P(\eta)$  temporal evolution,  $0 \le \eta \le 0.1$

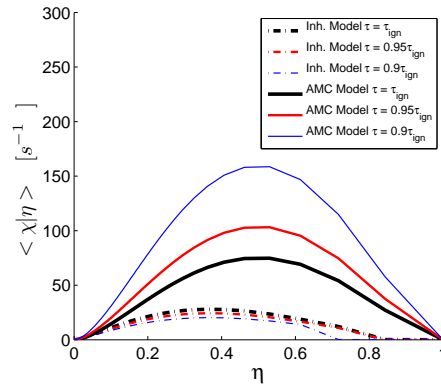
Figure 7.13:  $\langle \chi | \eta \rangle$  and PDF evolution at  $L_{ign}$  for  $T_{coflow} = 980K$

while the inhomogeneous model again shows a steady increase up to the time of ignition. This is reflected in the predictions of  $L_{ign}$ , where this peak has a delaying effect, pushing ignition to a distance further downstream of the fuel inlet. The values at which ignition occur are beginning to converge for the two different models, with only a small gap present, indicating that at this lower temperature the chemistry is more sensitive to mixing than with  $T_{coflow} = 1080K$ . The magnitudes of  $\langle \chi | \eta \rangle$  for the different models are illustrated in Fig. 7.13 b). The trends previously observed for  $\langle \chi | \eta = \xi_{mr} \rangle$  are reproduced in the relative magnitudes of the curve, with the inhomogeneous model predicting a steady increase and the AMC model providing a relatively fast decrease in  $\langle \chi | \eta = \xi_{mr} \rangle$ . In Fig. 7.13 c), the relative changes between the models can be seen, substantiating what is seen in Fig. 7.13 a) with a slow increase of  $\langle \chi | \eta = \xi_{mr} \rangle$  for the inhomogeneous model and a fast decrease for the AMC model. Fig. 7.13 d) demonstrates the PDF values for the different ignition locations at various timesteps. The results indicate that at early stages the PDF for the inhomogeneous model shows a stronger and narrower peak than with the AMC model, however, as time progresses, the distribution becomes very similar at ignition. The wide spread of the PDF indicates that a large range of  $\eta$ -space has a strong influence on the calculation of the Favre-averaged values for both models.

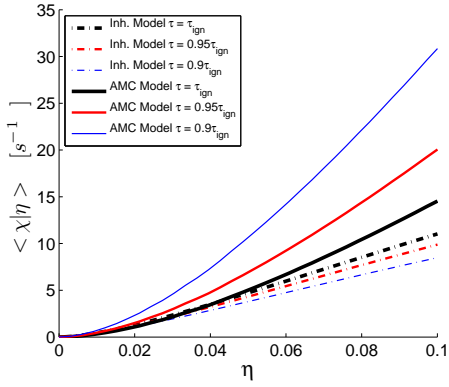
The final temperature used for comparison between the models is  $T_{coflow} = 950K$ . At this temperature, there is a longer delay in ignition, and the lower temperatures result in ignition occurring in an area of lower mixing. The tendency towards reaction at a reduced  $\langle \chi | \eta = \tilde{\xi}_{mr} \rangle$  is highlighted in Fig. 7.14 a), which shows significantly lower values than seen at 980K or 1080K. The gap in the  $\langle \chi | \eta = \tilde{\xi}_{mr} \rangle$  values between the two models is further reduced at this temperature, which is a further indication that the temperature sensitivity is playing an increasingly dominant role in the simulations. At  $T_{coflow} = 1080K$ , the gap between the  $\langle \chi | \eta = \tilde{\xi}_{mr} \rangle$  predictions of the two models is large, on the order of  $40s^{-1}$ , while at  $T_{coflow} = 980K$ , this reduces to  $3s^{-1}$  and at  $T_{coflow} = 950K$  this is further reduced to approximately  $1s^{-1}$ . This reduction indicates that the chemical source term is competing more with the  $\langle \chi | \eta \rangle$  predictions as the coflow temperature decreases, limiting chemical reaction rates and providing an overall increase in autoignition lengths. The  $\langle \chi | \eta \rangle$  curves, shown in Fig. 7.14 b) and c), show further demonstration of the trends observed at higher coflow temperatures. While the AMC model predicts a sharp decrease as time progresses, the inhomogeneous model shows an essentially constant value between  $0 \leq \eta \leq 0.03$ , which is close to  $\tilde{\xi}_{mr}$ . The best agreement between the two models is also in this region. The PDF



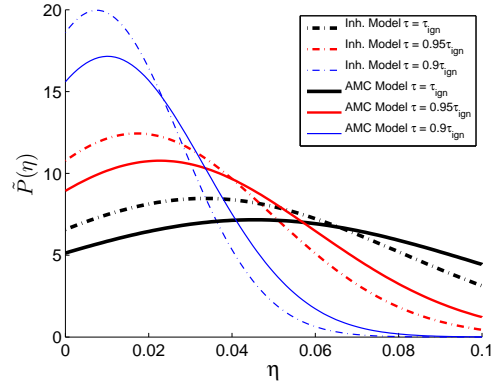
(a)  $\langle \chi | \eta = \xi_{mr} \rangle$  temporal evolution



(b)  $\langle \chi | \eta \rangle$  temporal evolution



(c)  $\langle \chi | \eta \rangle$  temporal evolution,  $0 \le \eta \le 0.1$



(d)  $P(\eta)$  temporal evolution,  $0 \le \eta \le 0.1$

Figure 7.14:  $\langle \chi | \eta \rangle$  and PDF evolution at  $L_{ign}$  for  $T_{coflow} = 950K$

evolution for both models is shown in Fig. 7.14 d), where the inhomogeneous model once again predicts ignition in areas with a slightly lower mean and lower variance, resulting in narrower, stronger peaks in the PDF. Therefore, Favre-averaging with the PDF provided by the AMC model tends to smear out any peaks in conditional temperature or species productions, further delaying ignition.

Through examining the  $\langle \chi | \eta \rangle$  curves for both models leading up to and at the time of ignition, the reasons for the reduced  $L_{ign}$  values predicted by the inhomogeneous model can be explained by examining the temporal  $\langle \chi | \eta \rangle$  evolution. The nature of the AMC model and the fixed shape of the  $\langle \chi | \eta \rangle$  distribution provides unexpected behaviour: leading up to the point of ignition, shifts in the PDF due to changes in the value of  $\tilde{\xi}$  at the ignition location result in the  $\langle \chi | \eta \rangle$  distribution decreasing the magnitude of the distribution as time progresses, despite a net increase in  $\tilde{\chi}$ . The inhomogeneous model displays the opposite trend, with the magnitude of  $\langle \chi | \eta \rangle$  increasing with  $\tilde{\chi}$ . At low  $T_{coflow}$ , the overall increased mixing provided with the AMC model precludes early ignition at locations which are predicted by the inhomogeneous model. At high  $T_{coflow}$ , despite the differences in predicted  $\langle \chi | \eta = \tilde{\xi}_{mr} \rangle$ , little difference in  $L_{ign}$  is observed due to the increasing magnitude of the chemical source term in the CMC equation.

### 7.7.3 Conditional Scalars

As the predictions of  $\langle \chi | \eta \rangle$  directly affect the chemistry calculations, examining the predictions of conditional species mass fractions is a direct indication of the performance of the inhomogeneous and AMC mixing models. This section provides a comparison of the conditional values for  $\chi$ ,  $\tilde{P}(\eta)$ ,  $Y_{OH}$ , and  $T$  taken at the ignition location. In this comparison, the  $T_{coflow} = 980K$  scenario is used, with plots taken 0.02ms prior to ignition, or  $\tau/\tau_{ign} = 0.95$ , as well as at the time of ignition.

In order to aid in the interpretation of the conditional predictions, the PDF for both the AMC and inhomogeneous mixing model is provided in Fig. 7.15 a). It can be seen for both models that there is a change in the mean value as time progresses, indicated by a shift in the peak values of the respective curves. This is due to the fuel penetrating further into the domain, and the local  $\tilde{\xi}$  values increasing as time passes. As  $\tilde{\xi}$  increases,  $\tilde{\xi}''^2$  also increases, leading to a wider and flatter PDF curve. As the PDF spreads, the

influence of conditional values from a wider  $\eta$  range become increasingly important to the Favre-averaged values. The PDFs relating to the inhomogeneous model are centered at leaner  $\eta$  values and possess a smaller variance, due to ignition occurring further upstream in the domain with the inhomogeneous model.

The  $\langle \chi | \eta \rangle$  profiles for both the AMC model and the inhomogeneous model are shown in Fig. 7.15 b). The previous trends identified in Fig. 7.12 b) and c), Fig. 7.13 b) and c), and Fig. 7.14 b) and c) are once again represented, with the AMC model predicting a decrease in the magnitude of the  $\langle \chi | \eta \rangle$  curve as time progresses, and the inhomogeneous model predicting an increase in the  $\langle \chi | \eta \rangle$  curve as time progresses. In the region of  $\xi_{mr}$ , which for the AMC model is  $\xi_{mr} = 0.0534$  and for the inhomogeneous model is  $\xi_{mr} = 0.0474$ , the AMC model predicts a significant reduction of  $\langle \chi | \eta = \xi_{mr} \rangle$  over the timestep shown, on the order of 10-20%, while the inhomogeneous model predicts an essentially unchanged level of conditional scalar dissipation rate. This overall lower level of mixing, as well as a less time dependent prediction around  $\xi_{mr}$  seen with the inhomogeneous model is expected to provide an increase in the chemical activity at this location, and earlier predictions of ignition.

The conditional  $OH$  mass fraction,  $\langle Y_{OH} | \eta \rangle$ , is an important precursor to ignition. In previous studies [46, 47], it is used as a measure of determining the time at which ignition occurs. Therefore, any difference seen in the predictions of  $\langle Y_{OH} | \eta \rangle$  can influence the overall ignition and combustion results. In Fig. 7.15 c), the  $\langle Y_{OH} | \eta \rangle$  values from both models are shown. At both times shown, the inhomogeneous model predicts a higher level of  $OH$  radicals present in the flow. This is an indication that the lower  $\langle \chi | \eta \rangle$  leading up to ignition predicted by the inhomogeneous model allows for an earlier buildup of the concentration of radicals. The larger peak  $OH$  concentration for the inhomogeneous model is also an indication of the lower overall  $\langle \chi | \eta \rangle$  at the time of ignition with the inhomogeneous model.

Although the calculations of  $\langle T | \eta \rangle$  occur following the chemistry calculation, the predicted values are still a good indication of the overall chemical activity occurring at a location, without investigating each individual species separately. Large reaction rates at a given  $\eta$  yield large amounts of evolved enthalpy, which causes a corresponding increase in the conditional temperature. Fig. 7.15 d) indicates that the  $\langle T | \eta \rangle$  trends closely follow the  $\langle Y_{OH} | \eta \rangle$  seen in Fig. 7.15 c). Again, the lower predictions of  $\langle \chi | \eta \rangle$  made by the inhomogeneous model allow increased chemical activity and increased conditional

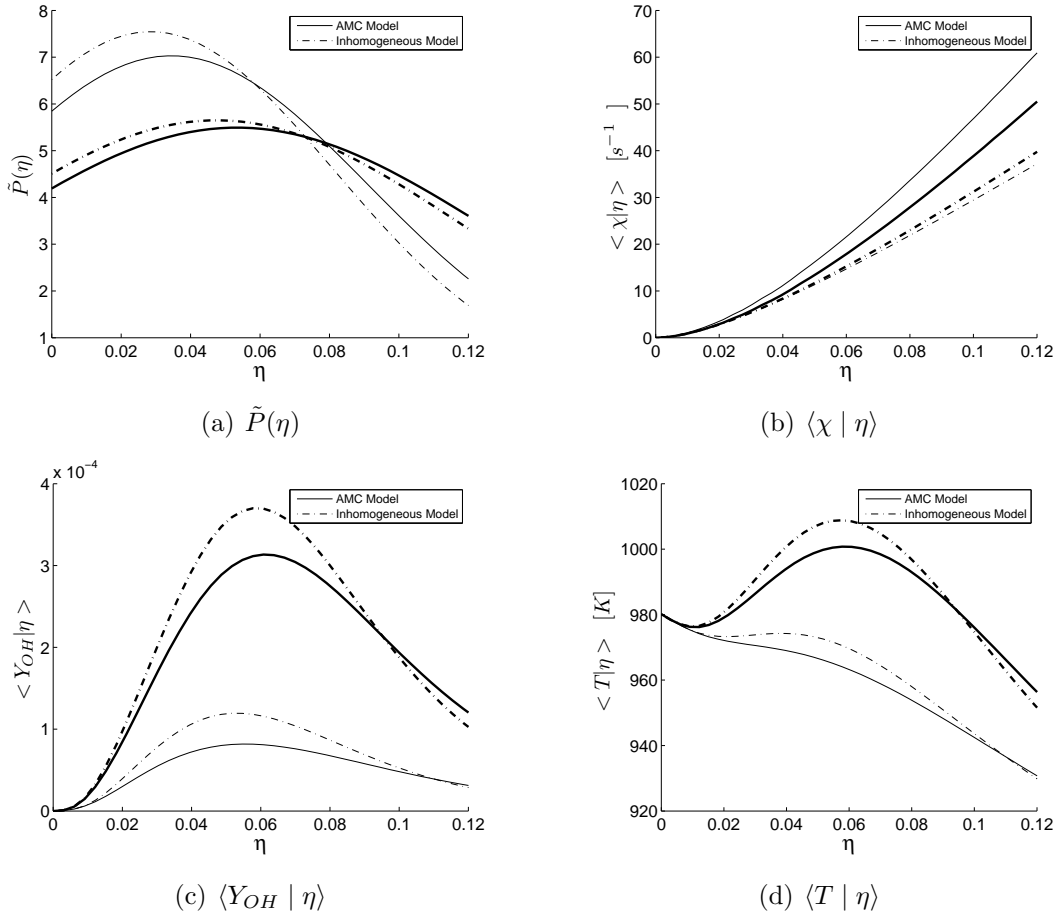


Figure 7.15: Conditional values at  $\tau/\tau_{ign} = 0.95$  (thin lines) and at the time of ignition (thick lines), all taken at  $L_{ign}$

temperatures in comparison to what is seen with the AMC model. The buildup of  $\langle T | \eta \rangle$  appears once again to be more gradual due to the steady increase of  $\langle \chi | \eta \rangle$ , while the AMC model predicts a peak  $\langle \chi | \eta \rangle$  occurring before ignition, which further delays predictions of ignition.

The trends seen in the conditional values further substantiate the trends indicated previously in Figs. 7.12 - 7.14, with a steady increase of  $\langle \chi | \eta = \xi_{mr} \rangle$  predicted with the inhomogeneous model and a peak, then rapid decrease of  $\langle \chi | \eta = \xi_{mr} \rangle$  predicted with the AMC model. The behaviour of the AMC model leading up to ignition provides an explanation of why the predictions of  $L_{ign}$  are larger than that produced with the inhomogeneous model.

### 7.7.4 Steady Flame Predictions

Following the predictions of autoignition, the case with  $T_{cflow} = 980K$  is run until steady state is reached with both the AMC and inhomogeneous model. Although there are no experimental data available to validate the numerical results, this provides a useful comparison of the performance of the AMC and inhomogeneous models in comparison to each other when applied to a steady flame.

The comparison between the models is performed by comparing predictions at 4 locations in the flow, as shown in Table 7.7.4. Position 1 and Position 2 are taken at the same axial location but different radial locations. Position 3 is taken further downstream along the centreline of the flow, and Position 4 is taken still further downstream, where temperatures are in decline. Only centreline values at downstream positions in the flow are taken for comparison, as there is little cross-stream variation in the  $\langle \chi | \eta \rangle$  curves predicted.

Examining the  $\tilde{\xi}$  field along the domain centreline, shown in Fig. 7.16, it is apparent

Table 7.4: Sample locations for comparison between AMC and inhomogeneous models

Position	Axial Location [x/d]	Radial Location [r/d]
Position 1	5	0 (Centreline)
Position 2	5	1.0
Position 3	10	0 (Centreline)
Position 4	15	0 (Centreline)

that there is virtually no difference between the AMC model and inhomogeneous model calculations. Any differences in the flowfield values are due to different temperature and density predictions, which cause a slight change in the mixing fields. The centreline  $\widetilde{\xi}''^2$ , not shown, is also similar for the two sets of simulations.

The centreline  $\widetilde{T}$  is an indication of the relative reaction progress for each of the two

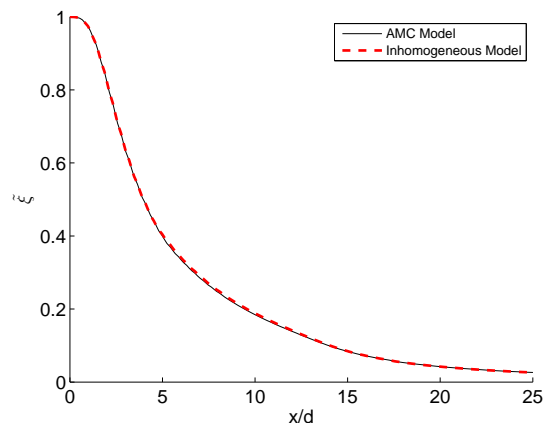


Figure 7.16: Centreline steady  $\widetilde{\xi}$  profile

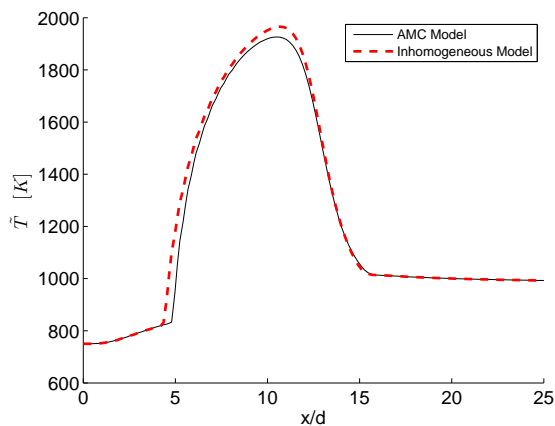


Figure 7.17: Centreline steady  $\widetilde{T}$  profile

models tested, shown in Fig. 7.17. The differences between the models become much more apparent than seen with the  $\widetilde{\xi}$  or  $\widetilde{\xi}''^2$ . The temperature begins to increase further upstream

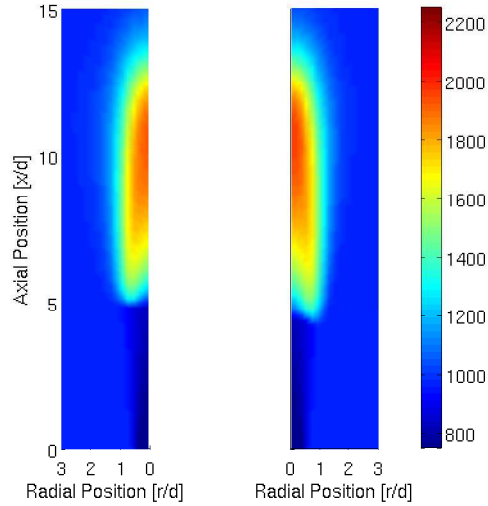


Figure 7.18:  $\tilde{T}$  [K] distribution within the computational domain, with the AMC model shown on the left and the inhomogeneous model shown on the right. The plots are mirrored along the centreline to provide easier visual comparison

for the inhomogeneous model, indicating an earlier onset of chemical reaction. Temperature peaks are also higher for the inhomogeneous model, but begin to decline earlier than what is seen with the AMC model. The peak temperatures are approximately 1970K for the inhomogeneous model and 1930K for the AMC model. To provide a more complete view of the temperature distribution within the domain, 2-Dimensional coloured plot is provided in Fig. 7.18. In this plot, it can be seen that the AMC and inhomogeneous model temperatures follow a similar pattern throughout the domain, with the inhomogeneous model indicating a flame position slightly closer to the inlet.

The results at Position 1 are summarised in Fig. 7.19, which provides a comparison of the  $\tilde{P}(\eta)$  distributions for the two models at this location. Since the flowfields in Fig. 7.19 a) have been shown to be nearly equivalent for both of the models, the PDF for each of the two models are expected to be similar, which is demonstrated. Fig. 7.19 b) shows that there are some differences between  $\langle \chi | \eta \rangle$  curves for the two models. The inhomogeneous model predicts a slightly lower value at  $\eta \leq 0.5$ , while for  $\eta \geq 0.5$ , the AMC model predicts lower values. Although both curves return the same  $\tilde{\chi}$ , the distribution in the inhomogeneous model favours higher levels of chemical activity, due to the reduced magnitude of the mixing term in the CMC equation. Accordingly, it can be seen in Fig. 7.19 c) that

the  $\langle Y_{OH} | \eta \rangle$  calculations from the inhomogeneous model indicate reaction is occurring at this location, while at the same location there is virtually no  $OH$  production for the AMC model. This is also reflected in the conditional temperatures, shown in Fig. 7.19 d), where the inhomogeneous model indicates a slight increase in temperature for lean mixture fraction values, while at this point, the AMC model is showing pure mixing without reaction. This finding substantiates the earlier centreline temperature results in Fig. 7.17, with the AMC model predicting a later ignition location than the inhomogeneous model.

Position 2 provides further insight into the differences between the AMC and inho-

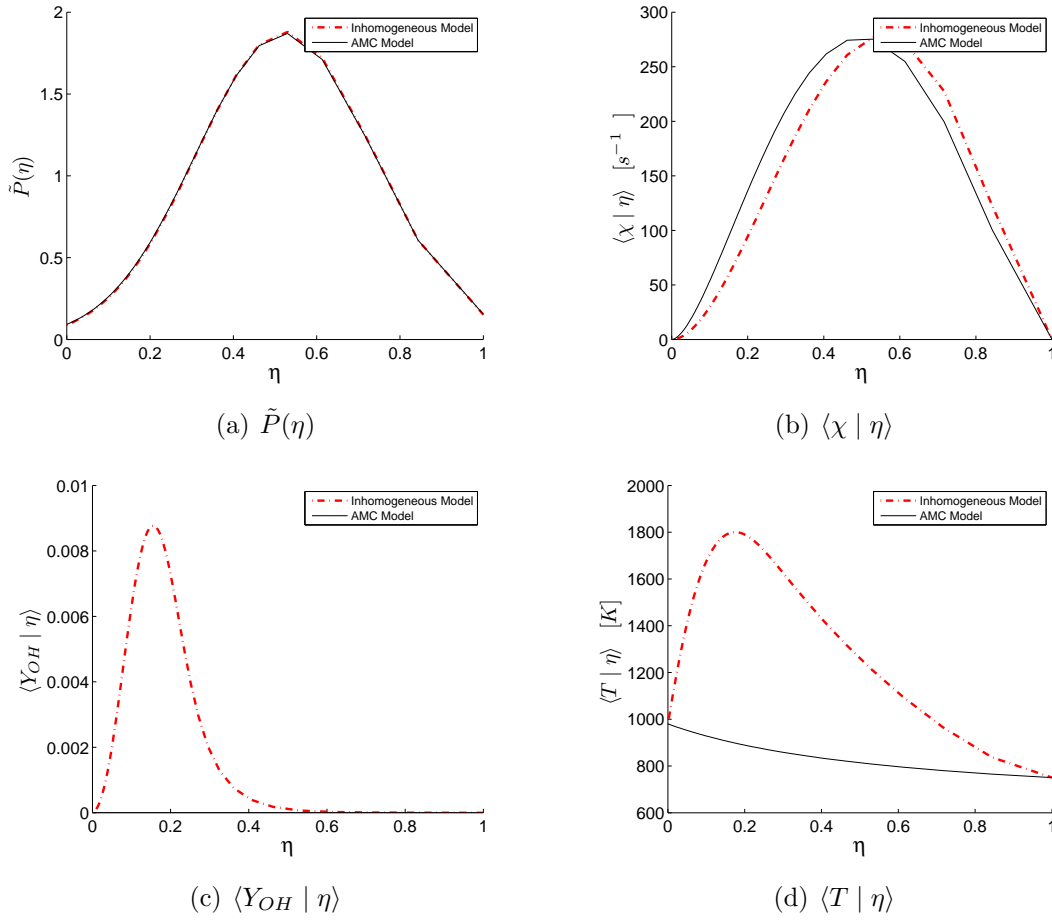
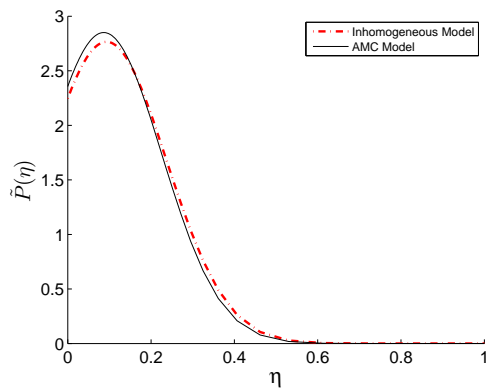
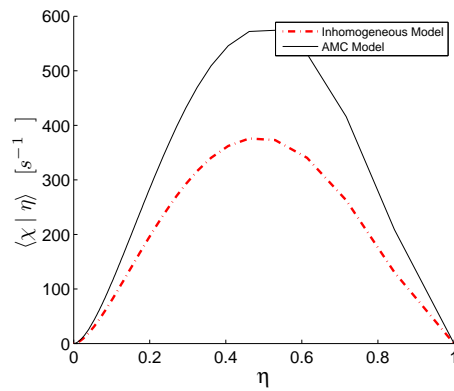


Figure 7.19:  $\tilde{P}(\eta)$ ,  $\langle \chi | \eta \rangle$ ,  $\langle Y_{OH} | \eta \rangle$  and  $\langle T | \eta \rangle$  at Position 1

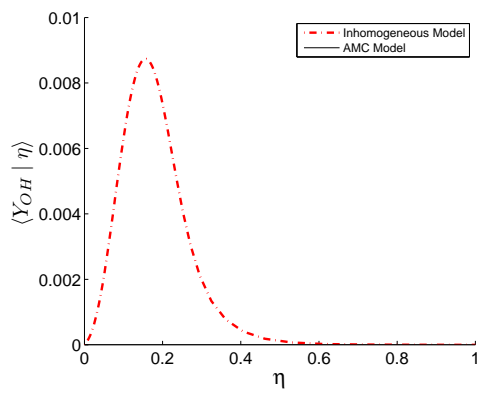
mogeneous model. Fig. 7.20 a) shows the PDFs for each of the respective flows. Despite the flowfields being extremely close in terms of predictions of  $\tilde{\xi}$  or  $\tilde{\xi}''^2$ , small variations



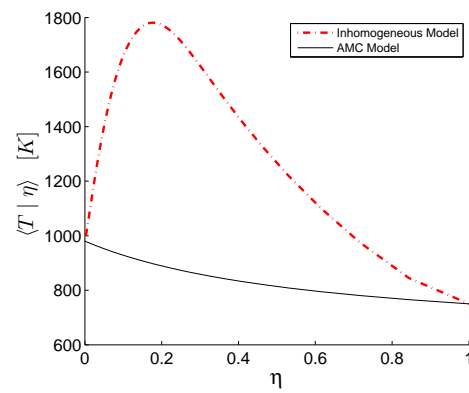
(a)  $\tilde{P}(\eta)$



(b)  $\langle \chi | \eta \rangle$



(c)  $\langle Y_{OH} | \eta \rangle$



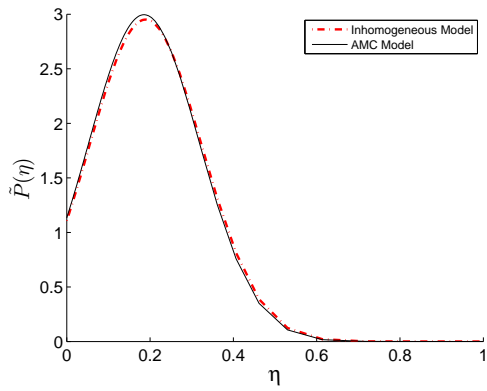
(d)  $\langle T | \eta \rangle$

Figure 7.20:  $\tilde{P}(\eta)$ ,  $\langle \chi | \eta \rangle$ ,  $\langle Y_{OH} | \eta \rangle$  and  $\langle T | \eta \rangle$  at Position 2

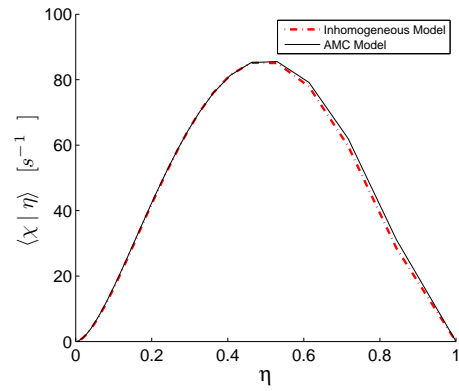
occur due to the onset of ignition. The earlier ignition demonstrated with the inhomogeneous causes a local decrease in density, thus affecting the  $\tilde{\xi}$  or  $\tilde{\xi}''^2$ . The resulting PDF for the inhomogeneous model is wider and possesses a smaller peak than with the AMC model. Although the respective changes are small, the effects are large in terms of the scalar dissipation rate and chemical reaction. The conditional scalar dissipation rate, Fig. 7.20, is significantly different between the two models. Once again, both curves return the same, or very similar,  $\tilde{\chi}$ ; however, it is mainly the difference in PDF which produces the discrepancy in magnitude, while further discrepancy may be attributed to differences in  $\tilde{\chi}$  resulting from flowfield differences between the two models. This effect is similar to what is observed, for example, in Fig. 7.12, where the magnitude of the AMC model curve shows a strong dependence on the local  $\tilde{\xi}$  and thus the PDF. The  $OH$  concentrations are shown in Fig. 7.20 c). The inhomogeneous model shows much higher levels of chemical activity, where the AMC model does not indicate significant changes in  $OH$  concentrations from the non-reacting case. The conditional temperature again reflects the  $Y_{OH}$  changes seen, as the conditional temperature begins to increase for the inhomogeneous model, while remains as the mixing case for the AMC model.

The results from Position 3, which lies on the centreline, but further downstream from Position 1, are shown in Figs. 7.21 a) - d). At this location, both models indicate significant reaction and the difference between the PDF values is small, as shown in Fig. 7.21 a). In addition, the AMC and inhomogeneous models predict similar  $\langle \chi | \eta \rangle$  curves, which is illustrated in Fig. 7.21 b). Despite the PDF and  $\langle \chi | \eta \rangle$  for both models being almost identical, there are still significant differences in  $OH$  levels. This difference can be attributed to the influence of the convective and diffusive terms in the CMC equation. The larger  $Y_{OH}$  predicted by the inhomogeneous model can be partially attributed to convection of this radical from areas with higher concentrations upstream of Position 3, while at the same time, diffusion driven by higher downstream temperatures leads to an increase in mixture enthalpy and higher reaction rates for a given  $\langle \chi | \eta \rangle$ . Fig. 7.21 d), showing  $\langle T | \eta \rangle$ , is further indication of the increased diffusive contribution, as the increased mixture enthalpy leads to higher conditional temperatures with the inhomogeneous model.

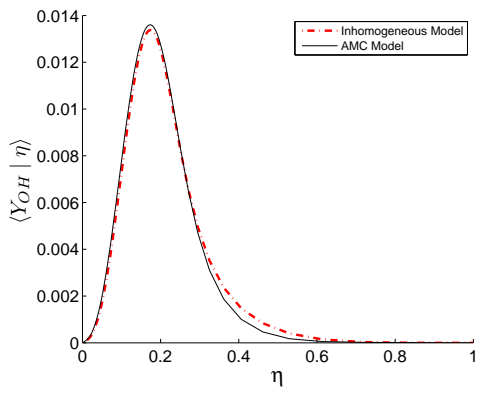
The final position investigated is also the furthest downstream from the fuel inlet. At this location, the majority of the reaction has taken place, and the centreline temperature predictions between the two models, Fig. 7.17, are very similar, indicating that mixture enthalpy and composition are very similar as well. Similar to Position 3, the PDF for



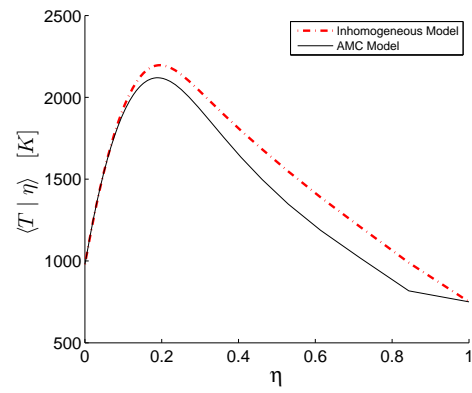
(a)  $\tilde{P}(\eta)$



(b)  $\langle \chi | \eta \rangle$



(c)  $\langle Y_{OH} | \eta \rangle$



(d)  $\langle T | \eta \rangle$

Figure 7.21:  $\tilde{P}(\eta)$ ,  $\langle \chi | \eta \rangle$ ,  $\langle Y_{OH} | \eta \rangle$  and  $\langle T | \eta \rangle$  at Position 3

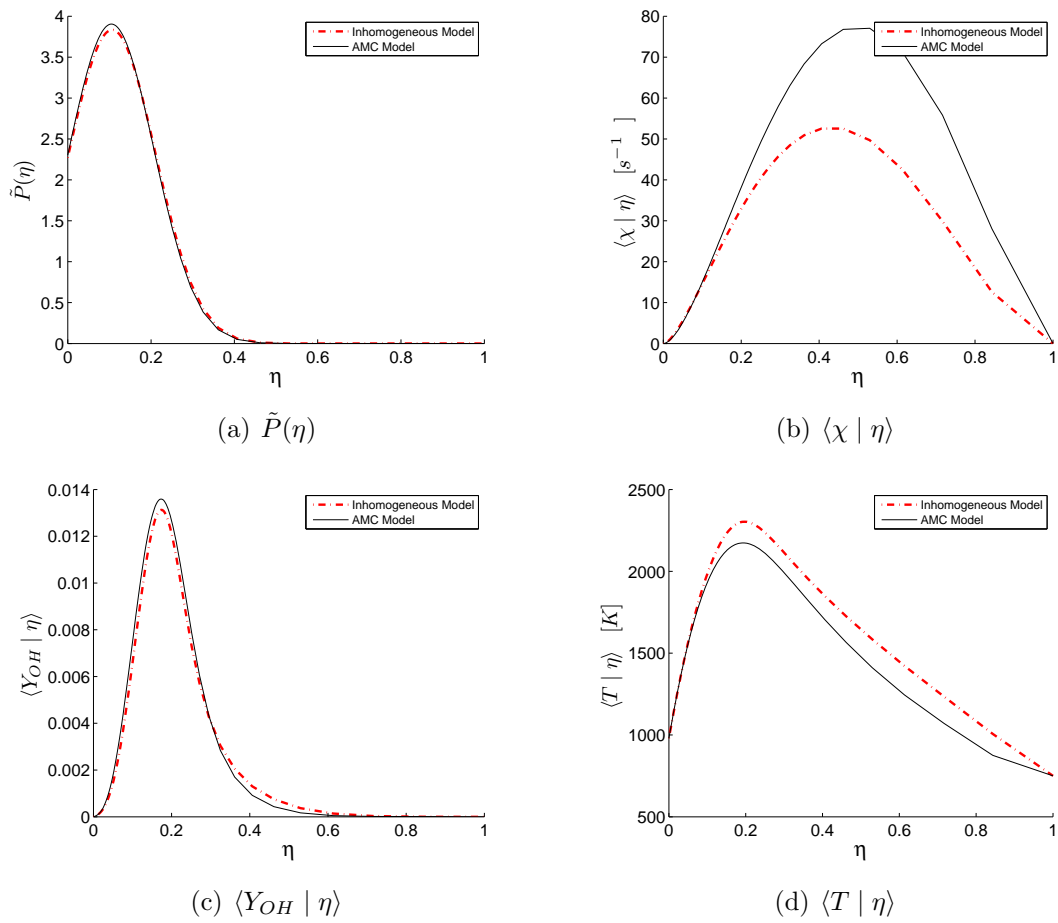


Figure 7.22:  $\tilde{P}(\eta)$ ,  $\langle \chi | \eta \rangle$ ,  $\langle Y_{OH} | \eta \rangle$  and  $\langle T | \eta \rangle$  at Position 4

both models at Position 4, Fig. 7.22 a) are almost identical. Only very small variations can be seen, with the AMC model predicting a narrower, and slightly higher peak. Fig. 7.22 b) presents  $\langle \chi | \eta \rangle$ . For  $\eta \leq 0.1$ , the inhomogeneous model predicts slightly higher mixing values, while for  $\eta \geq 0.1$ , the AMC model predicts higher values. Consequently, the  $\langle Y_{OH} | \eta \rangle$  profile shown in Fig. 7.22 c) indicates larger values for the AMC model for  $\eta \leq 0.1$ , corresponding to a lower  $\langle \chi | \eta \rangle$ , while the inhomogeneous model predicts larger  $\langle Y_{OH} | \eta \rangle$  for  $\eta \geq 0.1$ , where it has a lower  $\langle \chi | \eta \rangle$ . In general, both curves see a reduction in peak  $\langle Y_{OH} | \eta \rangle$  and  $\langle \chi | \eta \rangle$  values in comparison to Position 3, indicating that chemical activity is slowing at this location.  $\langle T | \eta \rangle$ , shown in Fig. 7.22 d), shows a higher predictions once again for the inhomogeneous model. This can also be attributed to the lower  $\langle \chi | \eta \rangle$  predicted by the inhomogeneous model for  $\eta \geq 0.1$ . The reduction in mixing prolongs the chemical reaction for this region of  $\eta$ -space, partially contributing to the higher  $\langle T | \eta \rangle$ . It is also seen that both curves for  $\langle T | \eta \rangle$  are higher than at any other location, indicating the increasing influence of the diffusive term in the CMC equation.

All other  $T_{coflow}$  are run to steady convergence, with mass and velocity residuals

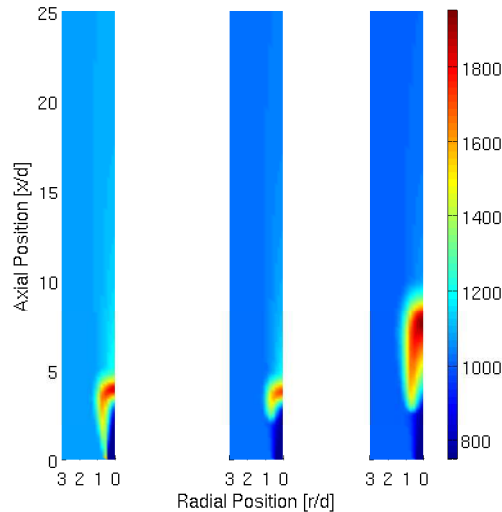


Figure 7.23: Steady flame  $\tilde{T}$  [K] predictions,  $T_{coflow} = 1080K$  on the left,  $T_{coflow} = 1020K$  in the centre,  $T_{coflow} = 1000K$  on the right

below  $1.0 \times 10^{-4}$ . Although the results are not presented in detail, the final flame structure of each scenario is of interest to this study, and is presented in Fig. 7.23 and Fig.

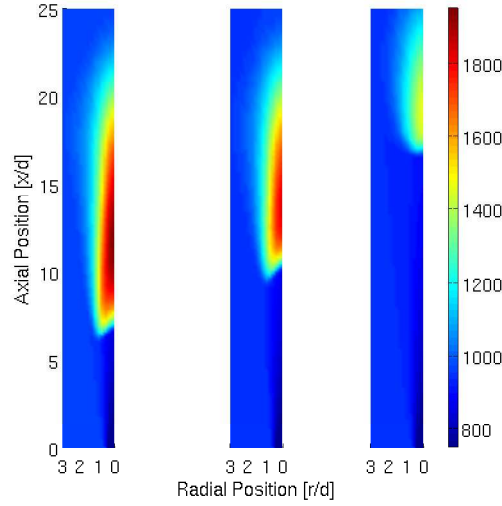


Figure 7.24: Steady flame  $\tilde{T}$  [K] predictions,  $T_{coflow} = 960K$  on the left,  $T_{coflow} = 950K$  in the centre,  $T_{coflow} = 940K$  on the right

7.24. The random spots regime and no ignition regimes, as defined by Markides and Mastorakos [42], are not observed for the range of  $T_{coflow}$  tested. Similar to the conclusions by Patwardhan and Lakshmisha [43], it is believed that the averaging nature of RANS type simulations dampen the turbulent fluctuations sufficiently that the random spots regime is not observed. Lifted flames are observed in the range of  $940K \leq T_{coflow} \leq 1020K$ , while flashback is observed for  $T_{coflow} = 1080K$ . This is seen to be independent of the present mixing model used. It is also seen that in the lifted flame predictions, the liftoff distance is inversely proportional to  $T_{coflow}$ , with higher temperatures leading to a flame stabilised nearer the fuel inlet. This is an indication of the increase in the influence of diffusion and chemical reactivity at elevated temperatures, allowing combustion to occur for higher  $\tilde{\chi}$  with increasing coflow temperatures.

Overall, the inhomogeneous model is seen to predict the onset of combustion closer to the fuel inlet with higher overall temperatures, both Favre-averaged and conditional. This is the result of the  $\langle \chi | \eta \rangle$  distributions, which allow for increased chemical activity further upstream in the domain. The enthalpy evolved is then convected downstream, encouraging further reaction and higher conditional temperatures at subsequent locations. At areas far from the inlet, such as Position 4, although the  $\tilde{\chi}$  values are similar for both models, the distribution predicted by the inhomogeneous model provides a higher overall conditional

temperature curve and increased chemical activity at large  $\eta$ .

## 7.8 Inhomogeneous Model Results

This section focuses on analysis of the results of the inhomogeneous mixing model. The inhomogeneous model conditional scalar dissipation rate is examined on a term-by-term basis to determine how and why the model provides different results at different locations in comparison to the AMC model.

### 7.8.1 Equation Budgets

In Eq. 3.55, reproduced as:

$$\frac{1}{2}\tilde{P}(\eta)\langle\chi|\eta\rangle = \underbrace{-\frac{\partial}{\partial t}\tilde{I}_1(\eta)}_{\text{Term 1}} + \underbrace{\left[-\tilde{u}_i\frac{\partial\tilde{I}_1(\eta)}{\partial x_i}\right]}_{\text{Term 2}} + \underbrace{\left[-D_t\frac{\partial\tilde{\xi}}{\partial x_i}\frac{\partial}{\partial x_i}\left(\frac{\tilde{I}_2(\eta)}{\tilde{\xi}''^2}\right)\right]}_{\text{Term 3}} + \underbrace{\left(\frac{\tilde{I}_2(\eta)}{\tilde{\xi}''^2}\right)\left[\frac{\partial\tilde{\xi}}{\partial t} + \tilde{u}_i\frac{\partial\tilde{\xi}}{\partial x_i}\right]}_{\text{Term 4}},$$

4 different terms are identified, each of which represents a contribution to the molecular mixing,  $\langle\chi|\eta\rangle$ . Term 1 is the temporal derivative of  $\tilde{I}_1$ , and represents the changes due to the transient nature of the flowfield. In steady simulations this term is equal to zero. Term 2 represents the convective term, and is largely influenced by the magnitude of the velocity. Term 2 is also dependent on the spatial gradients of  $\tilde{I}_1$ , which is a function of the PDF, as defined by Eq. 3.51. Term 3 represents the diffusion occurring in space, and is a function of the turbulent diffusivity, spatial gradient of  $\tilde{\xi}$ , and the gradient of  $\frac{\tilde{I}_2}{\tilde{\xi}''^2}$ . The final term, Term 4, is a function of the value of  $\tilde{\xi}''^2$  multiplied by the total derivative of  $\tilde{\xi}$ , making it heavily dependent on the flowfield predictions.

For simplicity, the comparison is conducted using a single coflow temperature,  $T_{coflow} = 980K$ , and multiple axial and radial locations within the flow. By using the results at the

Table 7.5:  $\tilde{\xi}$  and  $\tilde{\xi}''^2$  of locations studied for inhomogeneous model equation budgets

Axial Position [ $L/L_{ign}$ ]	Radial Position [ $r/d$ ]	$\tilde{\xi}$	$\tilde{\xi}''^2$
0.5	0.0	0.6783	0.0460
	0.5	0.3917	0.0634
	1.0	0.0154	0.0041
1.0	0.0	0.0479	0.0051
	0.5	0.0444	0.0046
	1.0	0.0159	0.0019
1.25	0.0	0.0016	$9.4 \times 10^{-5}$
	0.5	0.0020	$1.1 \times 10^{-4}$
	1.0	0.0016	$1.0 \times 10^{-4}$

time of ignition, it is possible to investigate various regions of the flow close to the inlet, where the temporal changes in the mixing field are smaller, and further into the domain, beyond the location of ignition, where the fuel flow has not yet fully developed at the timestep of interest. As such, the axial locations taken are  $0.5L_{ign}$ ,  $1.0L_{ign}$  and  $1.25L_{ign}$ . Investigation into locations beyond  $1.25L_{ign}$  is not possible at the time of ignition, as the  $\tilde{\xi}$  values beyond this location have not yet surpassed  $\eta_{min}$  required for the dynamic CMC cells to become active, as outlined in Sec. 5.4.1. Likewise, the radial coordinates are selected to investigate the extents of the active CMC grid. This results in radial coordinates of  $r/d = 0$ ,  $r/d = 0.5$ ,  $r/d = 1.0$ . At each of the locations, the contribution of each of the terms in Eq. 3.55 is examined. Table 7.5 provides  $\tilde{\xi}$  and  $\tilde{\xi}''^2$  for each location examined.

At the axial location nearest the fuel inlet,  $x = 0.5L_{ign}$ , it can be seen in Fig. 7.25 that the inhomogeneous model predicts a nearly symmetrical  $\langle \chi | \eta \rangle$ . The centreline, or  $r/d = 0$  predictions indicate peak mixing occurs at approximately  $\eta = 0.5$ , and follows the typical AMC curve the most closely. Progressing further outward, at  $r/d = 0.5$ , the curve demonstrates higher  $\langle \chi | \eta \rangle$  values for all  $\eta$ . This corresponds to a position within the mixing layer mixing layer, as identified previously in Fig. 7.7 a), with the peak variance values occurring off centre. The peak of this curve is shifted slightly rich of  $\eta = 0.5$ . Following this peak magnitude in mixing seen at  $r/d = 0.5$ , the  $\langle \chi | \eta \rangle$  values at  $r/d = 1.0$  decrease once again. The magnitude of the curves shown in Fig. 7.7 indicates that peak mixing occurs somewhere away from the centreline, where the fuel and oxidiser streams both interact.

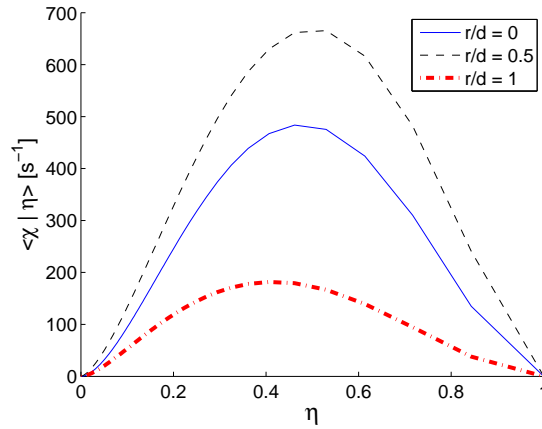
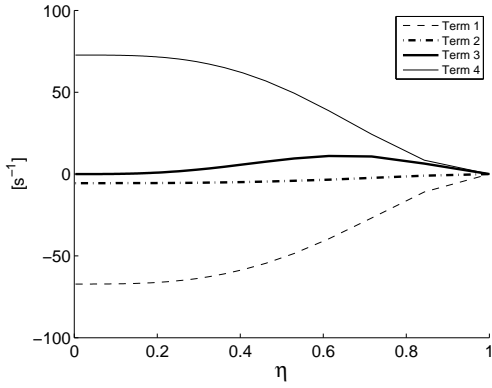


Figure 7.25:  $\langle \chi | \eta \rangle$  at  $r/d = 0, 0.5$  and  $1.0$ ,  $x = 0.5L_{ign}$

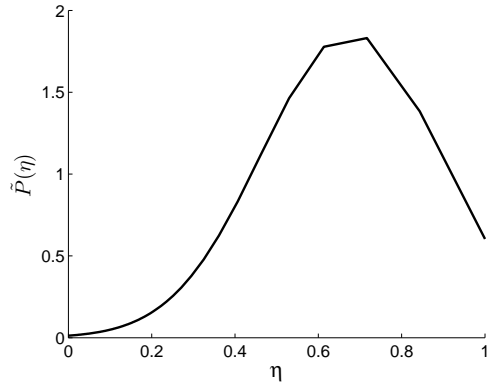
To identify the cause for the differences seen in Fig. 7.25, the individual terms of the inhomogeneous model as well as the PDF are examined in Fig. 7.26. Fig. 7.26 a) provides a breakdown of the inhomogeneous terms and Fig. 7.26 b) provides the PDF. At this location, Term 1 and Term 4 are seen to provide the largest contribution. The magnitude of Term 1, the temporal term, indicates that the flowfield is still unsteady and subject to relatively large changes. The evolution of  $\tilde{I}_1$  near the inlet over a short period of time increases the magnitude of the term. Due to the negative sign on Term 1, its magnitude remains entirely negative for all  $\eta$ . The contribution of Term 4, the  $\tilde{\xi}$  field dependent term, provides a similarly large positive contribution. Term 4 provides further agreement with the large temporal gradients seen in Term 1, largely cancelling the influence of Term 1. Term 3 provides a relatively minor overall contribution to the inhomogeneous formulation; however it is seen to closely follow the shape and magnitude of the  $\tilde{P}(\eta)$  predictions shown at this location. This term is a measure of the influence of diffusion, which appears to be at a maximum near  $\eta = 0.6$ . Term 2 is seen to provide a negligible impact in the formulation, as there are no large velocity gradients in the flow prior to ignition. Moving outward radially to the  $r/d = 0.5$  location, with the inhomogeneous terms shown in Fig. 7.26 c) and the PDF in Fig. 7.26 d), the influence of Term 1 has fallen to almost negligible levels relative to the remaining terms, while the magnitude of Term 4 has increased by nearly a factor of 10. This indicates a decrease in the significance of the temporal gradient of  $\tilde{I}_1$ , while the spatial gradients of  $\tilde{\xi}$  have increased in importance. This is largely due to the steep drop off in  $\tilde{\xi}$  as the edge of the mixing layer is approached. Term 2, the convective

term, provides a larger contribution at this location as well. This is a result of the increased spatial gradient of  $\tilde{I}_1$ , which is dependent on the  $\tilde{\xi}$  field. Term 3 once again closely follows the PDF, however, in this location it becomes the most significant term at large  $\eta$ . At the  $r/d = 1.0$  location, it is seen in Fig. 7.26 e) and f) that the value of  $\tilde{\xi}$  is significantly lower than seen in the previous locations. The effect on the model terms is immediately obvious as well, with Term 1 and Term 3 becoming small relative to the remaining terms. This is an indication that temporal gradients are small, and the influence of diffusion is also relatively minor at this location, both largely due to the lack of influence of the fuel stream. Term 2 indicates that the convective effects dominate in this area, as diffusion is shown to be minor. It is interesting to note that the magnitude of Term 2 has changed sign when compared to Fig. 7.26 c), indicating that a change of direction of the general convection influence has occurred, possibly due to local variations in either axial or radial velocity. As the velocity gradients are small, relatively small changes in either axial or radial velocity could effect this change. Term 4 remains large because of the gradients in  $\tilde{I}_2$  at the edge of the mixing layer.

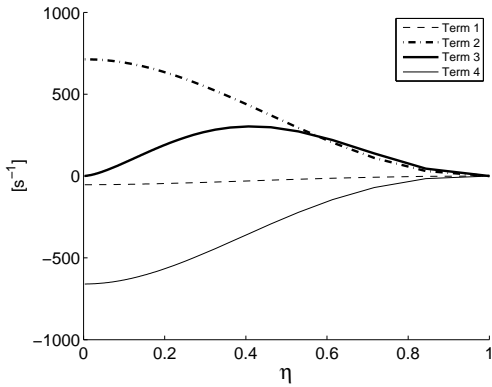
Moving to the axial location of ignition, i.e.  $x = L_{ign}$ , shown in Fig. 7.27, it can be seen that there is a smaller cross-stream variation in  $\langle \chi | \eta \rangle$ , especially at small  $\eta$ . Indeed, it can be seen that at either the centreline location or  $r/d = 0.5$  location, the  $\langle \chi | \eta \rangle$  predictions are nearly identical up to approximately  $\eta = 0.1$ . The predictions given at  $r/d = 1.0$  fall slightly in comparison to the locations closer to the centre of the flow, but still provides a similar shape in the  $\langle \chi | \eta \rangle$  curve. At large  $\eta$ , particularly above  $\eta = 0.8$ , the values at  $r/d = 1.0$  are seen to exceed those at  $r/d = 0.5$ . Despite this, the distribution of  $\tilde{P}(\eta)$  is largest at small  $\eta$ , making this difference essentially negligible. The inhomogeneous model contributions and PDF at the  $r/d = 0$  location, shown in Fig. 7.28 a) and b), respectively, indicate that both the influence of the terms as well as the PDF are largest below  $\eta \approx 0.3$ . Term 1 and Term 4 provide the largest influence on the model predictions, while Term 2 and Term 3 remain relatively small by comparison. As Term 1 is temporal, its large negative magnitude indicates that the flowfield is still evolving at this location relatively quickly. The magnitude of Term 4 also indicates that the total derivative of  $\tilde{\xi}$  is large and plays a significant influence. The convective and diffusive influence, given by Term 2 and Term 3, respectively, are minor as this location is along the centreline and only axial scalar and vector gradients are significant. The conditions at this location and this timestep support ignition of the mixture, as evidenced by an increase in Favre-averaged



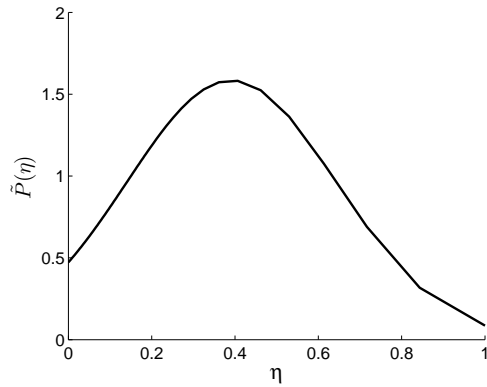
(a) Inhomogeneous model terms at  $r/d = 0$



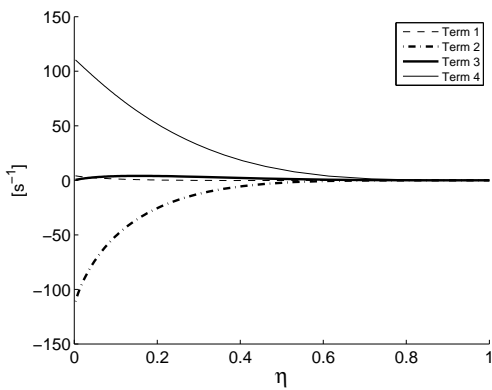
(b)  $\tilde{P}(\eta)$  at  $r/d = 0$ ,  $\tilde{\xi} = 0.6783$ ,  $\tilde{\xi}''^2 = 0.0460$



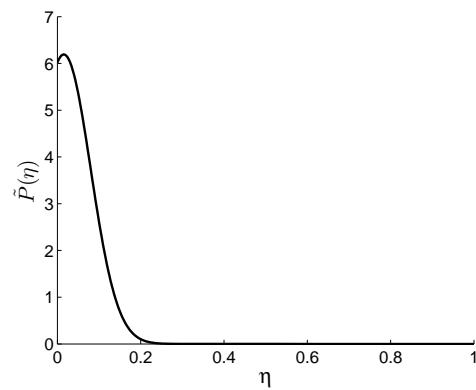
(c) Inhomogeneous model terms at  $r/d = 0.5$



(d)  $\tilde{P}(\eta)$  at  $r/d = 0.5$ ,  $\tilde{\xi} = 0.3917$ ,  $\tilde{\xi}''^2 = 0.0634$



(e) Inhomogeneous model terms at  $r/d = 1.0$



(f)  $\tilde{P}(\eta)$  at  $r/d = 1.0$ ,  $\tilde{\xi} = 0.0154$ ,  $\tilde{\xi}''^2 = 0.0041$

Figure 7.26: Inhomogeneous model terms and  $\tilde{P}(\eta)$  at  $x = 0.5L_{ign}$

temperature. Moving outward to the  $r/d = 0.5$  location, shown in Fig. 7.28 c) and d), the influence of Term 2 and Term 4 have changed. Instead of being dominated by Term 4, as seen at the centreline, Term 2 increases in importance, indicating that the convective term increases off centre. The PDF remains similar to that seen at the centreline, so there are no significant radial gradients of  $\tilde{\xi}$  or  $\tilde{I}_{1,2}$ . At the  $r/d = 1.0$  location, Fig. 7.28 e) and f) , the influence of the inhomogeneous terms remains largely unchanged from the  $r/d = 0.5$  location; however, the magnitudes of the respective terms have decreased.

When examining the results at the  $x = 1.25L_{ign}$  location, shown in Fig. 7.29,

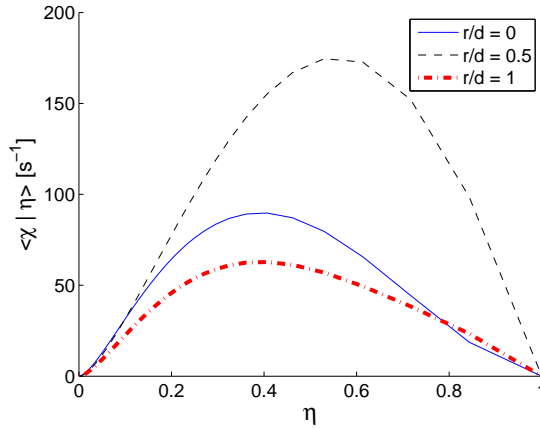
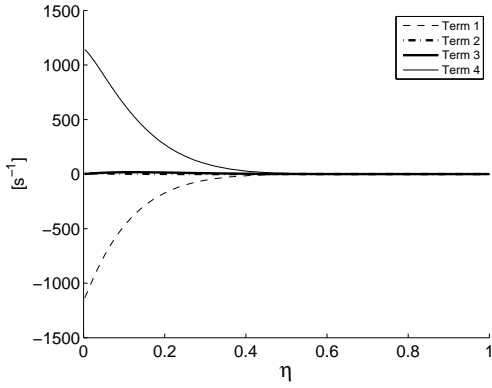
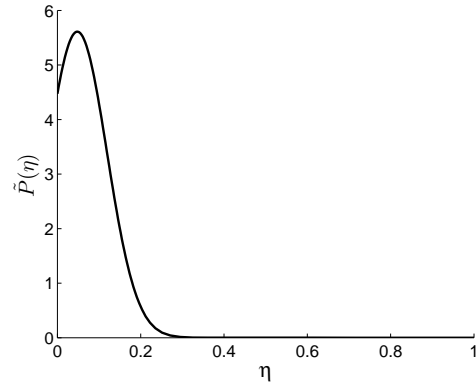


Figure 7.27:  $\langle \chi | \eta \rangle$  at  $r/d = 0, 0.5$  and  $1.0$ ,  $x = 1.0L_{ign}$

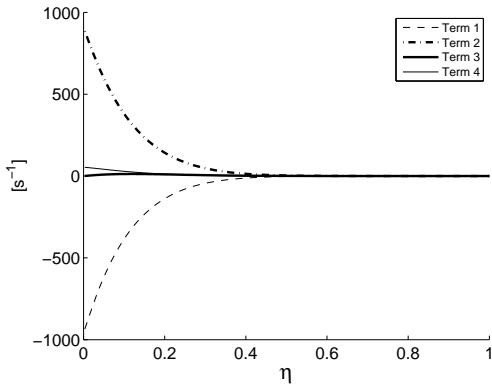
the trends seen in Fig. 7.27 are reproduced, albeit at a smaller magnitude. The respective  $\langle \chi | \eta \rangle$  curves at the centreline and  $r/d = 0.5$  locations, shown in Fig. 7.29, predict nearly identical values below  $\eta \approx 0.1$ , which is within the area of strongest influence from the PDF due to the local  $\tilde{\xi}$  values being on the order of  $1 \times 10^{-3}$ . Once again, moving outward, the  $\langle \chi | \eta \rangle$  curve decreases for all  $\eta$ . At large  $\eta$  values, it is seen that the curve appears to be discontinuous for all locations shown; however, this is largely due to a lack of resolution in this area due to the spacing of the  $\eta$  grid. This is not expected to influence the results in any way, as the  $\tilde{\xi}$  yield extremely low probabilities for large  $\eta$  at this axial location. Looking at the term-by-term contributions and PDF for the centreline, Fig. 7.30 a) and b), respectively, the most important terms are Term 1 in the negative direction and Term 4 in the positive direction. As  $\tilde{\xi}$  is on the order of  $10^{-3}$ , the PDF is highly concentrated near the pure air boundary. The strong and narrow peak of the PDF indicates that there is little variation in fuel content at this location and mixing is almost complete. At the



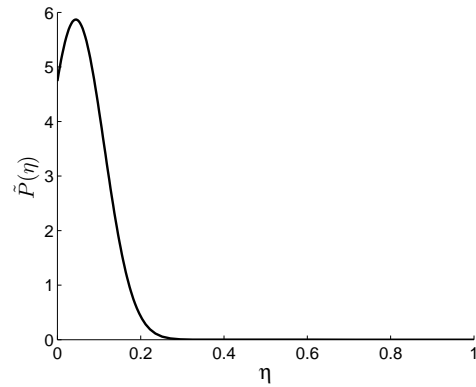
(a) Inhomogeneous model terms at  $r/d = 0$



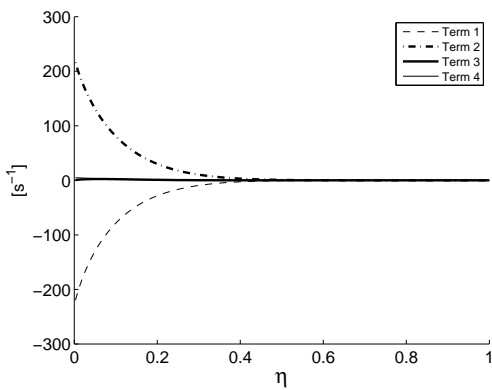
(b)  $\tilde{P}(\eta)$  at  $r/d = 0$ ,  $\tilde{\xi} = 0.0479$ ,  $\tilde{\xi}''^2 = 0.0051$



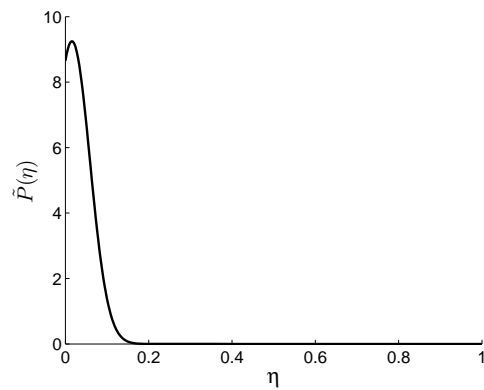
(c) Inhomogeneous model terms at  $r/d = 0.5$



(d)  $\tilde{P}(\eta)$  at  $r/d = 0.5$ ,  $\tilde{\xi} = 0.0444$ ,  $\tilde{\xi}''^2 = 0.0046$



(e) Inhomogeneous model terms at  $r/d = 1.0$



(f)  $\tilde{P}(\eta)$  at  $r/d = 1.0$ ,  $\tilde{\xi} = 0.0159$ ,  $\tilde{\xi}''^2 = 0.0019$

Figure 7.28: Inhomogeneous model terms and  $\tilde{P}(\eta)$  at  $x = 1.0L_{ign}$

$r/d = 0.5$  radial location, Fig. 7.30 c) and d), the inhomogeneous model terms once again follow the trend seen further upstream at the  $x = L_{ign}$  location, with Term 2 and Term 4 essentially swapping magnitudes. The PDF remains similar to the centreline position, as there is very little cross stream variation in  $\tilde{\xi}$  and  $\tilde{\xi}''^2$ . At the furthest radial location, Fig. 7.30 e) and f), the inhomogeneous terms remain similar in relative contribution to the model, with a slight reduction in magnitude. The PDF again remains similar to the other radial locations seen at  $x = 1.25L_{ign}$ .

Overall, for the current flow, the inhomogeneous model provides a  $\langle \chi | \eta \rangle$  curve some-

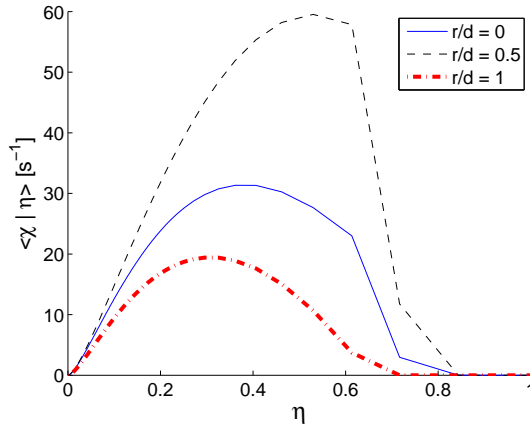
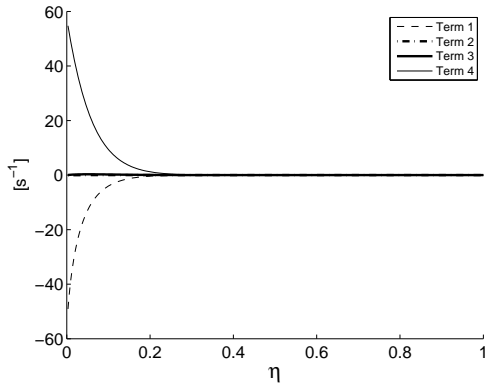


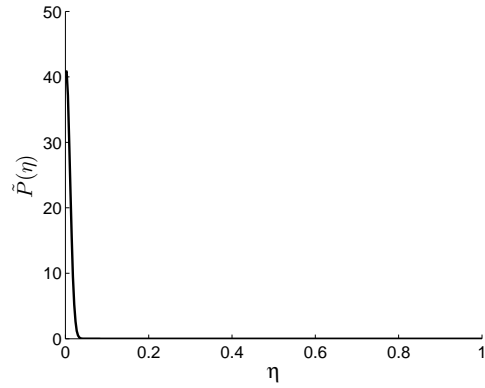
Figure 7.29:  $\langle \chi | \eta \rangle$  at  $r/d = 0, 0.5$  and  $1.0$ ,  $x = 1.25L_{ign}$

what similar in shape to the AMC model. The magnitude of the curve is largest off the centreline, and appears to peak within the mixing layer between the fuel and oxidiser. The magnitudes of the curves remain similar at small  $\eta$ , typically below  $\eta \approx 0.1$ . As the PDF is concentrated in this area for most locations, except very near the inlet, this area provides the largest impact on the overall performance of the model.

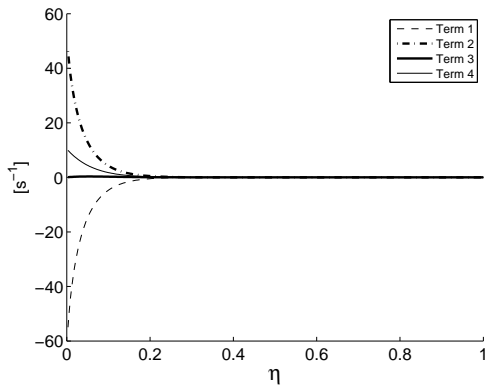
Following examination of the inhomogeneous model term budgets, several trends emerge. The first trend seen is that the magnitude of all terms within Eq. 3.55 have the largest relative contribution in areas within  $\eta$ -space where the PDF is also large. Term 1 remains negative in all instances seen within the current flow. Unsteady flows with large oscillations or fluctuations, such as vortex shedding, would result in positive and negative oscillations of Term 1 due to the alternating directions in the  $\tilde{\xi}$  gradients; however, for the current flow this is not seen. Term 1 is strongest along the centreline and decreases quickly with increasing radial distance. Term 2 has minimal influence at locations close to the inlet, but



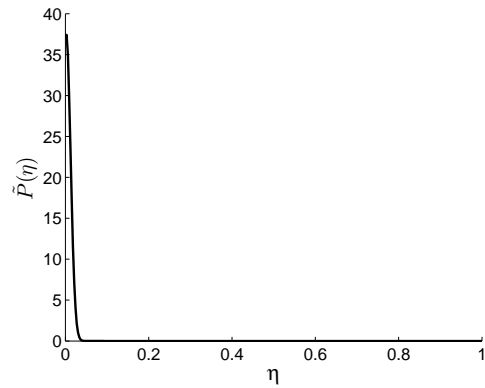
(a) Inhomogeneous model terms at  $r/d = 0$



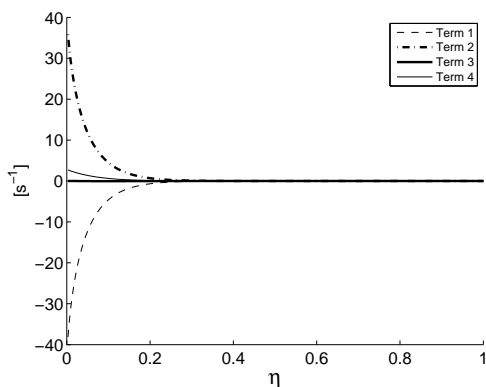
(b)  $\tilde{P}(\eta)$  at  $r/d = 0$ ,  $\tilde{\xi} = 0.0016$ ,  $\tilde{\xi}''^2 = 9.4 \times 10^{-5}$



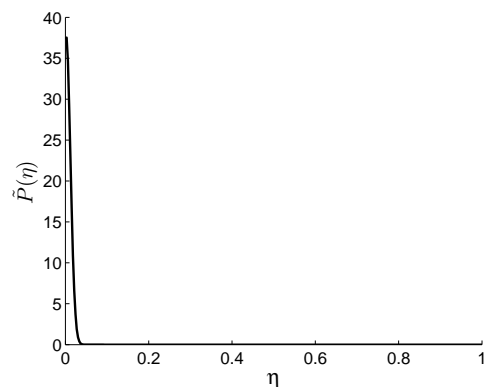
(c) Inhomogeneous model terms at  $r/d = 0.5$



(d)  $\tilde{P}(\eta)$  at  $r/d = 0.5$ ,  $\tilde{\xi} = 0.002$ ,  $\tilde{\xi}''^2 = 1.1 \times 10^{-4}$



(e) Inhomogeneous model terms at  $r/d = 1.0$



(f)  $\tilde{P}(\eta)$  at  $r/d = 1.0$ ,  $\tilde{\xi} = 0.0016$ ,  $\tilde{\xi}''^2 = 1.0 \times 10^{-4}$

Figure 7.30: Inhomogeneous model terms and  $\tilde{P}(\eta)$  at  $x = 1.25L_{ign}$

increases in importance with increasing axial distance. It is observed to remain close to zero along the centreline, but the importance increases with radial distance. Term 3 is seen to be the largest close to the inlet, with the relative contribution decreasing with increased axial distance. At locations close to the inlet, Term 3 appears to approximately follow the shape of the PDF, while providing the largest contribution at the interface between fuel and oxidiser, where flowfield gradients are largest. Term 4 is largest at areas close to the inlet along the centreline. At increasing axial distance, the contribution of Term 4 while off the centreline is seen to be small, decreasing in importance with increased radial distance. In general, at large distances from the fuel inlet, the model predicts very consistent results and contributions for the various terms, indicating that mixing remains fairly consistent through this portion of the domain, while for areas near the inlet, the mixing shows a strong spatial dependence.

The implementation of the inhomogeneous model in the present work, which follows the method of Devaud et al. [3] and Milford [11], is shown to provide qualitatively similar results in comparison to these previous numerical simulations. In both studies, the magnitude of the individual terms are seen to be large where the PDF is also large, a result mirrored in the present work. The autoignition simulations performed by Milford [11] demonstrated different trends for  $L_{ign}$  predictions; the inhomogeneous model is seen to predict increased ignition lengths compared to the AMC model when applied to a high pressure methane jet, a trend opposite to the present predictions. The difference is attributed to application of the model in a significantly different flow.

## 7.9 Summary

This chapter describes the numerical simulation of an autoigniting flame using multiple sets of turbulence constants and two different mixing models. The ignition length results indicate that all models show an underprediction in ignition length compared to experimental results; however, when results are shifted by 10K in the negative direction, equating to the stated 1% experimental error [42], a much closer fit to the experimental data is seen, with only slight underpredictions of ignition length observed. In the current study, both the lifted flame and flashback regimes are attained, while it is believed that the coflow temperatures tested are on the edge of the no ignition boundary.

Modification of the mixing model constants resulted in large changes to the flowfield. Reduction of  $C_{\epsilon_1}$  resulted in a decrease of centreline  $\tilde{\xi}$ , but an increase in the magnitude of centreline  $\tilde{\xi}''^2$  in comparison to the standard constants. The ignition length predictions also increased compared to the standard constants. Reduction of  $S_{c_t}$  decreased centreline  $\tilde{\xi}$ . Near the inlet, centreline  $\tilde{\xi}''^2$  increased relative to the standard constants, however the peak was reached early and  $\tilde{\xi}''^2$  began to decline in relation to the standard constants and the modified  $C_{\epsilon_1}$  case. The peak  $\tilde{\xi}''^2$  is the lowest of the 3 cases tested. Predicted ignition lengths for reduced  $S_{c_t}$  are shorter than those predicted by the standard model constants.

Comparison of the AMC and inhomogeneous models yielded slight differences in  $L_{ign}$ , with AMC providing the larger predictions. This is attributed to the temporal behaviour of the  $\langle \chi | \eta \rangle$  distribution. The scaling undertaken with the AMC model in order to match  $\tilde{\chi}$  causes the magnitude of the scalar dissipation rate to peak at early times, then subsequently decrease, while the inhomogeneous model is seen to produce a gradual ramp up of  $\langle \chi | \eta \rangle$ , therefore promoting earlier ignition.

Examination of the conditional values leading up to the point of ignition provide further evidence of the differences in performance. The lower mixing values throughout  $\eta$ -space promote earlier reaction, leading to a quicker buildup of  $OH$  radicals prior to ignition. This increase in chemical activity is followed by a corresponding increase in the conditional temperatures and therefore the Favre-averaged temperature.

Steady state predictions of the flame differ between the AMC and inhomogeneous models, with the inhomogeneous model predicting an earlier location of reaction and an overall higher peak centreline temperature. This is believed to be caused by the distribution of the  $\langle \chi | \eta \rangle$  curve near the fuel inlet for the inhomogeneous model, which provides lower conditional scalar dissipation rate values than the AMC model at low  $\eta$ , i.e. in the vicinity of the peak chemical reactions. Within the flame, the  $\langle \chi | \eta \rangle$  distributions of both models become similar, indicating that any differences are due to the diffusive and convective terms of the CMC equation. Finally, the flame structures of each  $T_{coflow}$  are shown, indicating that both the lifted flame and flashback regimes are realised.

While examining the equation budgets for the inhomogeneous model, it is seen that the strongest spatial dependence is near the fuel inlet, where gradients are largest. Moving further downstream, the influence of the terms stabilise, showing very little spatial dependence far from the inlet. The peak mixing values are seen off the centreline of the domain, within the mixing layer between the fuel and oxidiser.

# Chapter 8

## Conclusions

The focus of the present study is investigation of the performance of a finite volume based CMC code, fully coupled with CFD calculations in conjunction with two different mixing models, the AMC model and the inhomogeneous model. The performance of this code is evaluated with respect to a well documented, steady jet flame, as well as with an autoigniting flow upon which previous numerical work is based.

The numerical implementation of the various models are described, including the discretisation of the CMC equation and the AMC and inhomogeneous mixing models. The method of implementing the solver used for the CMC equation and chemistry interactions is also provided. Several strategies used to reduce computational cost of the CMC calculations are also investigated.

Simulation of a steady flame is presented following the experimental measurements of Barlow and Carter [40]. This work provides a well documented flame from which to base a steady simulation for code validation. Once preliminary results are obtained, the study is further extended to include simulation of autoignition processes, based on the experimental work by Markides and Mastorakos [42]. The effect of mixing model and turbulence constants are explored in relation to the autoignition predictions.

For both the steady flame and autoignition case, the calculation is allowed to proceed until a steady flame is obtained. The results were then compared with experimental data, if available, or analysed accordingly.

## 8.1 Numerical Techniques

The present study included a finite volume discretisation of the CMC calculation fully coupled with flowfield calculations. It is seen that the feedback provided in this formulation has the ability to predict combustion and autoignition in the flames studied, yielding accurate conditional species predictions while providing a flowfield characteristic of typical  $k - \epsilon$  model performance, with jet penetration underpredicted and jet spreading overpredicted.

As a means of improving the computational efficiency of the CMC calculations, several methods are investigated to improve the ability of CMC to adapt to various flows. This includes the use of a CMC grid scaling factor, overlaying it with the CFD grid at multiples of the base grid spacing, as well as providing a dynamic CMC grid, which adapts to regions where ignition and combustion are likely to occur, thereby avoiding calculations for locations that will not support combustion. The scaling factor is seen to provide a proportional reduction in computational cost, however, a strong dependence on axial grid spacing is observed. When the CMC mesh becomes too coarse, fluctuations in the conditional values yield unphysical oscillations in the flowfield, and is not used in the bulk of the study. The dynamic CMC grid proves to be extremely efficient, allowing the CMC calculations to proceed at a fast rate, only slowing when fuel penetrates the domain to a large extent.

The chemical mechanism used in the current study [53] is seen to provide accurate conditional values when compared to experimental measurements. Temperature predictions are slightly higher than experimentally observed values; however, this may be in part due to the flowfield predictions which are not tuned for the steady flame calculations via adjustment of turbulence model parameters. The VODE solver used for solution of the CMC equation is seen to capture the stiff chemical kinetics such that the autoignition events and trends are well represented.

## 8.2 Steady State Results

Through steady state simulation, it is seen that the computational code exhibits typical traits of the  $k - \epsilon$  model, with an underprediction of the centreline penetration, and an overprediction of spreading within the domain. The centreline values are underpredicted

by approximately 35% compared to the experimental results, indicating that correction of the turbulence constants is required if more accurate results are required. The general trends for  $\tilde{\xi}$ ,  $\tilde{\xi}''^2$ ,  $\tilde{U}$  and  $\tilde{T}$  predictions are in good agreement with experimental data.

The CMC portion of the calculations appears to function well in relation to the experimentally measured values. The predictions of  $\langle Y_{OH} | \eta \rangle$  are in good agreement with experimental measurements. A close link is seen between the  $\langle T | \eta \rangle$  and  $\langle \chi | \eta \rangle$  fields. Some discrepancies can be seen due to the turbulent flow and mixing field simulations using the standard  $k - \epsilon$  model.

### 8.3 Autoignition Results

Simulation of the autoignition experiments performed by Markides and Mastorakos [42] yield encouraging results. The agreement between experimental data and numerical simulations is not as strong as some previous LES simulations, which use both CMC methods [46] and PDF methods [45]; however predictions of ignition location and ignition conditions follow experimental and previous numerical trends closely. An overall qualitative improvement in comparison to previous RANS results is seen in relation to predictions of flame structure [43]. A general underprediction of ignition length is seen in all cases.

The impact of the selection of turbulence constants is evaluated. The impact of turbulence constants has a large effect on the formation of the steady flowfield for the autoignition flow: reducing  $C_{\epsilon_1}$  to 0.40 from 1.40 yields an increase in centreline  $\tilde{\xi}''^2$  and therefore  $\tilde{\chi}$ . Reducing  $Sc_t$  to 0.5 from 0.7 yields a reduction in centreline  $\tilde{\xi}''^2$  and  $\tilde{\chi}$ . However, the choice of turbulence constants has a small impact on ignition length predictions, by changing  $L_{ign}$  by 5% at most. The predictions of  $L_{ign}$  are proportional to centreline  $\tilde{\xi}''^2$ , with  $L_{ign}$  increased by  $C_{\epsilon_1} = 0.40$  in comparison to the standard constants, and  $L_{ign}$  reduced by  $Sc_t = 0.5$  in comparison to the standard constants.

## 8.4 Impact of Mixing Models

The selection of mixing model is seen to play a role in the predictions of  $L_{ign}$ . Predictions of  $L_{ign}$  performed by the inhomogeneous model are lower than that of the AMC model by up to 15%. The difference in predictions between the models decreases as the temperature increases and dependence on mixing predictions decreases. The inhomogeneous model results indicate that the effect is largely due to the magnitude of the  $\langle \chi | \eta \rangle$  curve predicted. The AMC model predicts an early peak in the magnitude of the  $\langle \chi | \eta \rangle$  curve, but the magnitude decreases with increasing  $\tilde{\xi}$ . The inhomogeneous model predicts a slow ramp up of  $\langle \chi | \eta \rangle$ , increasing with  $\tilde{\chi}$  as time progresses. The slow ramp up of  $\langle \chi | \eta \rangle$  with the inhomogeneous model provides conditions more suitable for autoignition, while the AMC model  $\langle \chi | \eta \rangle$  progression leads to a delay in ignition.

The effects of using the inhomogeneous mixing model on a steady flame are also examined. It is seen that the inhomogeneous model predicts an earlier temperature peak and overall higher temperatures throughout the domain. This is largely a result of the distribution of  $\langle \chi | \eta \rangle$  predicted by the inhomogeneous model, favouring lower  $\langle \chi | \eta \rangle$  at small  $\eta$  near the inlet. This leads to a faster rate of species evolution and earlier ignition by the inhomogeneous model. Near the centre of the flame, the AMC and inhomogeneous model yield very similar  $\langle \chi | \eta \rangle$  predictions; however, the effects of the convective and diffusive terms in the CMC equation yield differences in the conditional values predicted. The effects of the inhomogeneous model are seen to have the largest impact near the fuel inlet and in areas with large gradients.

## 8.5 Recommendations and Future Work

Throughout the course of this study, several numerical problems were documented. This included numerical errors in the form of discontinuities in the mixing model formulation, typically appearing when  $\tilde{\xi}''^2$  exceeds approximately  $0.1\tilde{\xi}$ . Although it was attempted to revise the calculations such that the discontinuity was avoided, this produced unsatisfactory results with large portions of the  $\langle \chi | \eta \rangle$  curve becoming negative, and subsequently forced to zero. The effect on the calculations was to yield unrealistically early autoignition predictions due to the conditional scalar dissipation rate being locally equal to zero.

Further investigation into why this happens and how to provide a correction that yields accurate results is recommended so that the simulations may be run under the exact experimentally documented conditions, i.e. increase the turbulence intensity to the value of 13% seen experimentally [42].

The steady simulation provided in this study was undertaken with only the standard  $k - \epsilon$  model coefficients. Although it was beyond the scope of the current study, further testing and analysis of the steady flame used for comparison is recommended in an attempt to provide better jet flame predictions with the current fully coupled CMC calculations.

To provide further characterisation of the chemistry, it is recommended that further study be undertaken with the autoignition simulations at lower coflow temperatures, documenting the "no ignition" and "random spots" regimes seen experimentally. As the lower temperature limit used,  $T_{coflow} = 940K$ , still resulted in ignition, albeit at very low  $\langle \chi \mid \eta = \xi_{mr} \rangle$  values. It is currently unknown how RANS simulations will behave at the lower temperature limit of autoignition with the current  $H_2 - N_2$  fuel mixture.

A further area of improvement in model formulation is to include the effects of differential diffusion in the CMC equation and study the effects that this has on autoignition and steady flame processes. As hydrogen is a highly diffusive fuel, the effects that this has on the current numerical predictions may be large. Inclusion of the  $\beta$ -PDF for CMC calculations is also an area of improvement for the current model, as many chemical interactions are seen to occur near the  $\eta = 0$  boundary, where the clipped Gaussian PDF performs somewhat poorly.

# Bibliography

- [1] N. Peters. *Turbulent Combustion*. Cambridge University Press, 2000.
- [2] E. O'Brien and T.L. Jiang. The conditional dissipation rate of an initially binary scalar in homogeneous turbulence. *Phys. Fluids A*, 3(12):3121–3123, 1991.
- [3] C.B. Devaud, R.W. Bilger, and T. Liu. A new method of modeling the conditional scalar dissipation rate. *Phys. Fluids*, 16(6):2004–2011, 2004.
- [4] S. B. Pope. *Turbulent Flows*. Cambridge University Press, 2000.
- [5] Richard W. Johnson. *The Handbook of Fluid Dynamics*. CRC Press LLC, 1998.
- [6] W. Malalasekera H.K. Versteeg. *An Introduction to Computational Fluid Dynamics, The Finite Volume Method*. Pearson Education Limited, 2007.
- [7] B.E. Launder W.P. Jones. The prediction of laminarisation with a two equation turbulence model. *Int. J. Heat and Mass Transfer*, 15(2):301–314, 1972.
- [8] D.C. Wilcox. Reassessment of the scale-determining equation for advanced turbulence models. *AIAA Journal*, 26(11):1299–1310, 1988.
- [9] B.E. Launder and B.I. Sharma. Application of the energy-dissipation model of turbulence to the calculation of flow near a spinning disc. *Lett. Heat Mass Transf.*, 1:131–138, 1974.
- [10] Ahmad El Sayed. Ignition delay of non-premixed methane-air mixtures using conditional moment closure (CMC). Master's thesis, University of Waterloo, Waterloo, Ontario, Canada, September 2007.

- [11] Adrian Milford. Investigation of an inhomogeneous mixing model for conditional moment closure applied to autoignition. Master's thesis, University of Waterloo, Waterloo, Ontario, Canada, May 2010.
- [12] N. Peters. Laminar diffusion flamelet models in non-premixed turbulent combustion. *Prog. Energy Combust. Sci.*, 10(3):319–339, 1984.
- [13] A.Yu. Klimenko and R.W. Bilger. Conditional moment closure for turbulent combustion. *Prog. Energy Combust. Sci.*, 25(6):595–687, 1999.
- [14] A. Papoulis. *Probability, random variables and stochastic processes*. McGraw-Hill, 1984.
- [15] P.A. Libby and F.A. Williams. *Turbulent Reacting Flows*. Springer-Verlag, Berlin, 1980.
- [16] D. Veynante and L. Vervisch. Turbulent combustion modelling. *Prog. Energy Combust. Sci.*, 28(3):193–266, 2002.
- [17] J. Janicka and N. Peters. Prediction of turbulent jet diffusion flame lift-off using a PDF transport equation. *Proc. Combust. Inst.*, 19:367–374, 1982.
- [18] D.B. Spalding. Mixing and chemical reaction in steady confined turbulent flames. *Symposium (International) on Combustion*, 13(1):649 – 657, 1971.
- [19] S.B. Pope. Lagrangian PDF methods for turbulent flows. *Annual Rev. Fluid Mech.*, 26:23–63, 1994.
- [20] A.Yu. Klimenko. Multicomponent diffusion of various admixtures in turbulent flow. *Fluid Dyn.*, 25(3):327–334, 1990.
- [21] R.W. Bilger. Conditional moment closure for turbulent reacting flow. *Phys. Fluids A*, 5(2):436–444, 1993.
- [22] V. R. Kuznetsov and V. A. Sabel'Nikov. *Turbulence and Combustion*. Hemisphere, New York, 1990.
- [23] N. Swaminathan and R.W. Bilger. Analyses of conditional moment closure for turbulent premixed flames. *Combust. Theory Model.*, 5(2):241–260, 2001.

- [24] J.D. Li and R.W. Bilger. A simple theory of conditional mean velocity in turbulent scalar-mixing layer. *Phys. Fluids*, 6(2):605–610, 1994.
- [25] J.H. Kent and R.W. Bilger. The prediction of turbulent diffusion flame fields and nitric oxide formation. *16th Symposium (Int.) on Combust.*, pages 1643–1655, 1976.
- [26] S.S. Girimaji. Assumed beta-PDF model for turbulent mixing : validation and extension to multiple scalar mixing. *Combust. Sci. Tech.*, 78(4-6):177–196, 1991.
- [27] P. Givi, C.K. Madnia, C.J. Steinberger, and S.H. Frankel. Large eddy simulations and direct numerical simulations of high speed turbulent reacting flows. Technical report, NASA Langley Research Centre, 1991.
- [28] V. Eswaran and S.B. Pope. Direct numerical simulation of the turbulent mixing of a passive scalar. *Phys. Fluids*, 31(3):506–520, 1988.
- [29] N. Swaminathan and S. Mahalingam. Assessment of conditional moment closure for single and multistep chemistry. *Combust. Sci. Technol.*, 112(1):301–326, 1996.
- [30] A. El Sayed and C.B. Devaud. Conditional moment closure (CMC) applied to autoignition of high pressure methane jets in a shock tube. *Combust. Theory Model.*, 12(5):943–972, 2008.
- [31] S.H. Kim, K.Y. Huh, and R.A. Fraser. Modeling autoignition of a turbulent methane jet by the conditional moment closure model. *Proc. Combust. Inst.*, 28:185–191, 2000.
- [32] M.J. Cleary and J.H. Kent. Multiple mapping conditioning for flames with partial premixing. *Combust. Theory Model.*, 12(5):943–972, 2008.
- [33] W.T. Kim and K.Y. Huh. Second-order conditional moment closure modeling of local extinction and reignition in turbulent non-premixed hydrocarbon flames. *Proc. Combust. Inst.*, 29:569–576, 2002.
- [34] Y.M. Wright, G. De Paola, K. Boulouchos, and E. Mastorakos. Simulations of spray autoignition and flame establishment with two-dimensional cmc. *Combust. Flame*, 143(4):402–419, 2005.

- [35] C.N. Markides, G. De Paola, and E. Mastorakos. Measurements and simulations of mixing and autoignition of an n-heptane plume in a turbulent flow of heated air. *Exp. Therm. Fluid Sci.*, 31(5):393–401, 2007.
- [36] G. De Paola, I.S. Kim, and E. Mastorakos. Second-order conditional moment closure simulations of autoignition of an n-heptane plume in a turbulent coflow of heated air. *Flow Turb. Combust.*, 82:455–475, 2009.
- [37] S.S. Girimaji. On the modeling of scalar diffusion in isotropic turbulence. *Phys. Fluids A*, 4(11):2529–2537, 1992.
- [38] G. Brethouwer and F.T.M. Nieuwstadt. DNS of mixing and reaction of two species in a turbulent channel flow: A validation of the conditional moment closure. *Flow, Turb. Combust.*, 66(209), 2001.
- [39] A. Milford and C.B. Devaud. Investigation of an inhomogeneous turbulent mixing model for conditional moment closure applied to autoignition. *Combust. Flame*, 157:1467–1483, 2010.
- [40] R.S. Barlow and C.D. Carter. Raman/Rayleigh/LIF measurements of nitric oxide formation in turbulent hydrogen jet flames. *Combust. Flame*, 97:261–280, 1994.
- [41] R.S. Barlow, N.S.A. Smith, J.-Y. Chen, and R.W. Bilger. Nitric oxide formation in dilute hydrogen jet flames: Isolation of the effects of radiation and turbulence-chemistry submodels. *Combust. Flame*, 117:4–31, 1999.
- [42] C.N. Markides and E. Mastorakos. An experimental study of hydrogen in a turbulent coflow of heated air. *Proc. Combust. Inst.*, 30:883–891, 2005.
- [43] S.S. Patwardhan and K.N. Lakshmisha. Autoignition of turbulent hydrogen jet in a coflow of heated air. *Int. J. of Hydrogen Energy*, 33:7265–7263, 2008.
- [44] W.P. Jones and S. Navarro-Martinez. Study of hydrogen auto-ignition in a turbulent air co-flow using a large eddy simulation approach. *Computers and Fluids*, 37:802–808, 2008.
- [45] W.P. Jones, S. Navarro-Martinez, and O. Rohl. Large eddy simulation of hydrogen auto-ignition with a probability density function method. *Proc. Combust. Inst.*, 31:1765–1771, 2007.

- [46] I. Stanković. *Numerical Simulations of Hydrogen Auto-Ignition in Turbulent Flows*. PhD thesis, University of Ghent, Ghent, Flanders, Belgium, 2011.
- [47] I. Stanković, A. Triantafyllidis, E. Mastorakos, C. Lacor, and B. Merci. Simulation of hydrogen auto-ignition in a turbulent co-flow of heated air with LES and CMC approach. *Proc. European Combust. Meeting*, 2009.
- [48] Stefan Georg Kerkemeier. *Direct numerical simulation of combustion on petascale platforms: Application to Turbulent Non-Premixed Hydrogen Autoignition*. PhD thesis, ETH Zurich, Zurich, Switzerland, 2010.
- [49] R.R. Cao, S.B. Pope, and A.R. Masri. Turbulent lifted flames in a vitiated coflow investigated using joint PDF calculations. *Combust. Flame*, 142:438–453, 2005.
- [50] J. Li, Z. Zhau, A. Kazakov, and F.L. Dryer. An updated comprehensive kinetic model of hydrogen combustion. *Inter. J. Chem. Kinet.*, 36:566–575, 2004.
- [51] M. O’Conaire, H.J. Curran, J.M. Simmie, W.J. Pitz, and C.K. Westbrook. A comprehensive modelling study of hydrogen oxidation. *Inter. J. Chem. Kinet.*, 36:603–622, 2004.
- [52] M.A. Mueller, T.J. Kim, R.A. Yetter, and F.L. Dryer. Flow reactor studies and kinetic modeling of the  $H_2 - O_2$  reaction. *Inter. J. Chem. Kinet.*, 31:113–125, 1999.
- [53] R.A. Yetter, F.L. Dryer, and H. Rabitz. A comprehensive reaction-mechanism for carbon-monoxide hydrogen oxygen kinetics. *Combust. Sci. and Tech.*, 79:97–128, 1991.
- [54] A.A. Konnov. Remaining uncertainties in the kinetic mechanism of hydrogen combustion. *Combust. Flame*, 152:507–528, 2008.
- [55] S.V. Patankar. *Numerical Heat Transfer and Fluid Flow*. Taylor & Francis Group, New York, 1980.
- [56] D.B. Spalding. A novel finite-difference formulation for differential expressions involving both first and second order derivatives. *Int. Journal Num. Meth.*, 4:551, 1972.
- [57] P.N. Brown, G.D. Byrne, and A.C. Hindmarsh. VODE: A variable-coefficient ode solver. Technical report, Lawrence Livermore National Laboratory, 1988.

- [58] A. El Sayed, A. Milford, and C.B. Devaud. Modelling of autoignition for methane-based fuel blends using conditional moment closure. *Proc. Combust. Inst.*, 32(1):1621–1628, 2009.
- [59] M. Cleary. *CMC Modelling of Enclosure Fires*. PhD thesis, University of Sydney, Sydney, Australia, 2004.
- [60] A.C. Hindmarsh. Gear: Ordinary differential equation system solver. Technical report, Lawrence Livermore National Laboratory, 1974.
- [61] J. Warnatz, U. Maas, and R.W. Dibble. *Combustion, Physical and Chemical Fundamentals, Modeling and Simulation, Experiments, Pollutant Formation, 4th Ed.* Springer, 2006.
- [62] Reaction Design. CHEMKIN A Software Package for the Analysis of Gas-Phase Chemical and Plasma Kinetics, <http://www.dipic.unipd.it/faculty/canu/files/Comb/Docs/chemkinCK.pdf>, 2000.
- [63] F.M. White. *Fluid Mechanics, 7th Ed.* McGraw-Hill, 2011.
- [64] W.P. Jones and B.E. Launder. The prediction of laminarisation with a two equation turbulence model. *Int. J. Heat and Mass Transfer*, 15(2):301–314, 1972.
- [65] S.B. Pope. An explanation of the turbulent round-jet/plane-jet anomaly. *AIAA*, 16(3):279–281, 1978.
- [66] P. Ouellette and P.G. Hill. Turbulent transient gas injections. *J. Fluids Eng.*, 122(4):743–752, 2000.
- [67] P. Gaillard. Multidimensional numerical study of the mixing of an unsteady gaseous fuel jet with air in free and confined situations. Technical report, SAE, 1984.
- [68] C.N. Markides, G. De Paola, and E. Mastorakos. Measurements and simulations of mixing and autoignition of an n-heptane plume in a turbulent flow of heated air. *Exp. Therm. Fluid Sci.*, 31:393–401, 2007.